Thesis for the degree of Doctor of Philosophy
in the Natural Sciences

Implementation and development of serial synchrotron crystallography at MAX IV

Monika Bjelčić

UNIVERSITY OF GOTHENBURG

Department of Chemistry and Molecular Biology
Gothenburg, 2023

Thesis for the degree of Doctor of Philosophy
in the Natural Sciences

Implementation and development of serial synchrotron crystallography at MAX IV

Monika Bjelčić

Cover: Deconstructed AI version of a synchrotron

ISBN: 978-91-8069-459-9 (PRINT)
ISBN: 978-91-8069-460-5 (PDF)
Available online at http://hdl.handle.net/2077/78516

Department of Chemistry and Molecular Biology
Division of Biochemistry and Structural Biology
University of Gothenburg
SE-405 30, Göteborg, Sweden
Printed by Stema Specialtryck AB
Borås, Sweden, 2023

SVANENMÄRKET
Trycksak
3041 0234

Abstract

Over the past decade, remarkable advancements in femtosecond X-ray free-electron lasers (XFELs) have brought about a profound transformation in structural biology. These XFELs have opened up exciting opportunities for conducting high-time resolution, room-temperature studies on protein structures and dynamics. This cutting-edge methodology involves exposing thousands of crystals to X-ray beams in random orientations at room temperature. These innovations have spurred the emergence of serial crystallography techniques, which have gained traction on more adaptable and readily accessible microfocus beamlines in synchrotron facilities. The primary focus of this thesis revolves around the development and implementation of serial synchrotron crystallography for proteins at the macromolecular beamlines BioMAX and MicroMAX, located at MAX IV Laboratory in Sweden.

This dissertation encompasses the development of two innovative sample delivery devices (Serial-X and AdaptoCell), incorporation of various fixed-target methods and preparation for TR-SSX. In Paper I, we introduced a novel approach for collecting data from oxygen-sensitive samples using fixed-target, complemented by the introduction of 3-D printed accessories. Paper III demonstrates the successful application of the methodology outlined in Paper I to determine the structure of CYP3A4. Paper II delves into the creation of the Serial-X flow cell, designed for efficient delivery of viscous samples, a tool that has now found utility on numerous beamlines worldwide. Lastly, in Paper IV, we present the first room-temperature serial synchrotron crystallography structure of spinach RuBisCo, along with the prepatory steps for a time-resolved SSX study of RuBisCO at BioMAX.

Acknowledgements

Thomas, thank you for seeing potential in me and giving me a chance when most wouldn't. You are the best mentor I could have wished for, giving me enough space but also knowing when to push me. I knew the working day would start good whenever we carpooled to work and talked about sports.

Richard, thank you for all your help with my manuscript and that you guided me toward the end. We had a bit distant beginning of our relationship and Covid didn't help with that. But in the end, the Queen Taylor bonded us.

Gisela, thank you for being a voice of reason and help in Gothenburg, and not more than an email away.

Gergely, thank you for all the bureaucracy guidelines and help with ISP. It was a pleasure to have you as my examiner.

Doris, a cruel world separated us knowing we would be an unstoppable force otherwise. Thank you for being an amazing host every time I was in Gothenburg. The fun we had every time you visited Malmö made me sad whenever you left. **Jonatan** and **Emil**, thank you for hosting me in your lab and helping with a big part of one of my projects. Time together on long hour beamtimes wouldn't be the same without you, especially after 2 a.m. **Owens** and **Andreas**, you guys were the best gossip and company whenever you came down for beamtime. **Analia**, we wouldn't have any work done if we were in the same city. Talking to you always felt like only minutes passed.

Mirko, you were my rock and guide when I first started. The day would be boring if we didn't have a small chitchat session. Our shared love for Star Wars made so many interesting lunch discussions, even when others would be confused about what are we talking about. Having you as a group member and a friend made my PhD journey so much more enjoyable. **Oskar**, my Oskar, there are not enough pages to thank for all your help and guidance. You were my unofficial mentor, and I am eternally grateful. On top of that, your unique humor makes you such an amazing person to call a friend. **Jie**, without you most of my ideas on the

beamline would not be possible. Your help, even during your free time, made it possible to have successful beamtimes. You are and forever will be a BioMAX magician. **Ana**, thank you for having your doors always open and patience with all my questions. **Aaron**, since you joined the group there hasn't been a dull day, not to mention that the amount of *slaying* has increased. **Yang**, thank you for all the time spent with me in the lab, some of my projects would have taken much longer without your help. **Kajsa**, without you my first project and paper would not be possible, thank you for seeing my vision and taking the time to do it with me.

To the whole **MX group**, it was such a pleasure to work alongside you for the last four years. To each and every one of you thank you for all the help during this time, and thank you for having patience to listen about Formula 1.

To all my friends back in Croatia and around the world, you made the world feel smaller and closer when times were difficult. All the messages, pictures, funny videos, zoom calls and beers made my days. **Sanja**, **Natali** and **Darko**, we stuck together during college and didn't allow different countries, and at some point other parts of the world, to break us apart. **Vedrana**, you are the best lesbian friend someone can ask for and days without your messages on Instagram wouldn't feel the same. **Emma**, our love for Swan Lake and Taylor Swift connected us, but we put in the work to stay connected even when we wouldn't physically see each other for over a year. Morning Skype coffees with you that always lasted at least 3 hours never felt like enough time. **Iva**, you are my emotional intelligence friend and without you I would have struggled in life, thank you for all the hours spent at coffee together. **Natalija** and **Ivana**, our friendship has been lasting since high school and has endured ups and downs but we always stayed together and babinjak with wine is always special and amazing with you too. **Maja**, you were the friend who literally went with me to the other side of the world, unfortunately bad luck separated us but without you that first big step would be so much harder to make (hope you will soon come back to Europe).

To my **Queen DNF's** girls, thank you for making every race weekend more fun. Meeting all of you last year made my love for F1 even bigger. **Lavanya**, meeting you as a similar soul in the most unexpected way, and I can't wait that we go together to a race and have the time of our life.

Viktor, you are the best brother a sister could ask let alone dream off. We have been a support for each other for more than 20 years now. Without you in my life, I wouldn't have the courage to go out and seek my dreams. Also, we share the same mental illnesses with our love and hope for Ferrari and talking about Formula 1 with you for hours were some of the most fun talks. My biggest regret is we don't live in the same place.

To my **muma** and **tuta**, thank you for giving me the tools to progress in life.

Pasha, even though you will not understand a word I wrote I am grateful to have you as my cat, and a tiny co-author of my thesis with the amount of letters you pressed.

Cassandra, I want to express my profound gratitude to you for your unwavering support throughout my PhD journey. Your love, patience, and belief in me were the pillars that sustained me through the academic challenges. Your sacrifices and unwavering faith have been a constant source of motivation. You will always be my Princess.

Publications

This thesis consists of the following research papers:

PAPER I: **Monika Bjelčić**, Kajsa Sigfridsson Clauss, Oskar Aurelius, Mirko Milas, Jie Nan, Thomas Ursby; "**Anaerobic fixed-target serial crystallography using sandwiched SiN membranes.**" Accepted (Acta Cryst. 79, https://doi.org/10.1107/S205979832300880X)

PAPER II: Swagatha Ghosh, Doris Zorić, Peter Dahl, **Monika Bjelčić**, Jonatan Johannesson, Emil Sandelin, Per Borjesson, Alexander Björling, Analia Banacore, Petra Edlund, Oskar Aurelius, Mirko Milas, Jie Nan, Anastasya Shilova, Ana Gonzalez, Uwe Mueller, Gisela Brändén, Richard Neutze; "**A simple goniometer compatible flow-cell for serial synchrotron X-ray crystallography**." J. Appl. Cryst. 56, 449–460. https://doi.org/10.1107/S1600576723001036

PAPER III: Owens Uwangue, Andreas Dunge, Johan Glerup, **Monika Bjelčić**, Gabrielle Wehlander, Gisela Brändén; "**Room temperature serial crystallography structure of human cytochrome P450 3A4.**" Manuscript (2023)

PAPER IV: **Monika Bjelčić**, Jonatan Johannesson, Emil Sandelin, Oskar Aurelius, Jie Nan, Thomas Ursby, Richard Neutze; "**Room-temperature Serial Synchrotron Crystallography structure of Spinacia oleracea RuBisCO: Towards Time-Resolved Structures.**" Submitted

Related papers that I have co-authored but that are not included in this thesis:

PAPER V: Doris Zorić, Jonatan Johannesson, Adams Vallejos, Emil Sandelin, Arpitha Kabbinale, Swagatha Ghosh, Annika Flink, **Monika Bjelčić**, John Rönnholm, Peter Dahl, E.V. Beale, C. Bostedt, C. Cirelli, C. Bacellar Cases da Silveira, P. Johnson, D. Ozerov, A. Batyuk, S. Boutet, C. Kupitz, A. Peck, F. Poitevin, R. Sierra, S. Lisova, C.J. Wallentin, Gisela Brändén, Richard Neutze. "**Structural changes in cytochrome c oxidase following the reduction of dioxygen to water.**" Manuscript (2023)

PAPER VI: Doris Zorić, Swagatha Ghosh, **Monika Bjelčić**, Jonatan Johannesson, Arpitha Kabbinale, Emil Sandelin, Yang Chen, Susan Nehzati, Richard Neutze, Kajsa Sigfridsson Clauss, Gisela Brändén. "**X-ray absorption spectroscopy as a tool to investigate details of the cytochrome c oxidase metal co-factors.**" Manuscript (2023)

PAPER VII: Andreas Dunge, Owens Uwangue, Cindy Phan, **Monika Bjelčić**, Jenny Gunnarsson, Gabrielle Wehlander, Helena Käck, Gisela Brändén; "**Exploring serial crystallography for drug discovery.**" Manuscript (2023)

PAPER VIII: Thomas Ursby, Karl Åhnberg, Roberto Appio, Oskar Aurelius, Artur Barczyk, Antonio Bartalesi, **Monika Bjelčić**, Fredrik Bolmsten, Yngve Cerenius, Bruce R. Doak, Miker Eguiraun, Thomas Eriksson, Ross J. Friel, Ishkhan Gorgisyan, Andrea Gross, Vahid Haghighat, Franz Hennies, Elmir Jagudin, Brian N. Jensen, Tobias Jeppsson, Marco Kloss, Julio Lidon-Simon, Gustavo M.A. De Lima, Roberto Lizatovic, Magnus Lundin, Antonio Milan-Otero, Mirko Milas, Jie Nan, Alberto Nardella, Anders Rosborg, Anastasya Shilova, Robert L. Shoeman, Frank Siewert, Peter Sondhauss, Vladimir O. Talibov, Hamed Tarawneh, Johan Thånell, Marjolein Thunnissen, Johan Unge, Christopher

Ward, Ana Gonzalez, Uwe Mueller; "**BioMAX – the first macromolecular crystallography beamline at MAX IV Laboratory.**" J. Synchrotron Rad. 27, 1415–1429. https://doi.org/10.1107/S1600577520008723

PAPER IX: Filip Leonarski, Jie Nan, Zdenek Matej, Quentin Bertrand, Antonia Furrer, Ishkhan Gorgisyan, **Monika Bjelčić**, Michal Kepa, Hannah Glover, Viktoria Hinger, Thomas Eriksson, Aleksander Cehovin, Mikel Eguiraun, Piero Gasparotto, Aldo Mozzanica, Tobias Weinert, Ana Gonzalez, Jörg Standfuss, Meitian Wang, Thomas Ursby, Florian Dworkowski; "**Kilohertz Serial Crystallography with the JUNGFRAU Detector at a 4th Generation Synchrotron Source.**" Accepted (IUCrJ https://doi.org/10.1107/S2052252523008618)

Contribution report

PAPER I: I designed the research, developed the method and co-developed the tools for anaerobic serial crystallography, crystallized the protein, collected and processed the crystallographic data, refined and analyzed the structures. I collected the XANES with Kajsa (Balder) and UV/Vis data. I wrote the manuscript and created figures.

PAPER II: I collected part of the data and contributed with testing and feedback to the design of the method and device. I processed all data and refined the structures. I commented on the manuscript.

PAPER III: I collected and processed part of the data.

PAPER IV: I refined the crystallization conditions and found conditions for obtaining microcrystals. I collected and processed all data. I planned and organized data collections based on results and refined the structures. I co-wrote the manuscript and created some figures.

Abbreviations

Here follows a list and short explanation of the different abbreviations used in this thesis.

2-PGA	2-**P**hospho**G**lycer**A**te
2,3diPGA	2,3-bis**P**hospho**G**lycer**A**te
3-PGA	3-**P**hospho**G**lycer**A**te
ADE	**A**coustic **D**roplet **E**jection
ADP	**A**denosine **D**i**P**hosphate
ATP	**A**denosine **T**ri**P**hosphate
BCU	**B**eam **C**onditioning **U**nit
C*c*O	**C**ytochrome *c* **O**xidase
dPGM	**P**hospho**G**lycerate **M**utase
DeoxyHb	**Deoxy**H**emoglob**in
DTT	**D**i**T**hio**T**hreitol
EDTA	**E**thylene**D**iamine**T**etraacetic **A**cid
LINAC	**LIN**ear particle **AC**celerator
Lyz	**L**ysozyme
LCP	**L**ipidic **C**ubic **P**hase
LDH	**L**actate **D**e**H**ydrogenase
GDVN	**G**as-**D**ynamic **V**irtual **N**ozzle
Hb	**H**emoglo**b**in
HCO	**H**eme **C**opper **O**xidase
HVE	**H**igh **V**iscosity **E**xtruder
ISPyB	**I**nformation **S**ystem for **P**rotein **C**rystallography **B**eamlines
MAD	**M**ulti-wavelength **a**nomalous **D**ispersion
MAG	**M**ono**A**cyl**G**lycerol
MetHb	**Met**H**emoglob**in
MR	**M**olecular **R**eplacement
MXCuBE	**M**acromolecular **X**tallography **Cu**stomized **B**eamline **E**nvironment
NAD	**N**icotinamide **A**denine **D**inucleotide

NADH	**N**icotinamide **A**denine **D**inucleotide **H**ydrogen
NanoBPM	**Nano** **B**eam **P**osition **M**onitor
NMR	**N**uclear **M**agnetic **R**esonance
OxyHb	**OxyH**emoglo**b**in
PDB	**P**rotein **D**ata **B**ank (online databank for protein structure)
PEG	**P**oly**e**thylene **g**lycol
PEP	**P**hospho**E**nol**P**yruvate
PK	**P**yruvate **K**inase
RMSD	**R**oot **m**ean **s**quare **d**eviation
RuBP	**R**ib**u**lose 1,5-**B**is**P**hosphate
SAD	**S**ingle-wavelength **a**nomalous **D**ispersion
SAXS	**S**mall **A**ngle **X**-ray **S**cattering
sHE	**S**oluble **E**poxide **H**ydrolase
SpRub	**Sp**inach **Rub**isco
SSF	**S**tiftelsen för **S**trategisk **F**orskning
SSX	**S**erial **S**ynchrotron **c**rystallography
SFX	**S**erial **F**emtosecond **c**rystallography
TR-SSX	**T**ime **R**esolved **S**erial **S**ynchrotron **c**rystallography
XANES	**X**-ray **A**bsorption **N**ear **E**dge **S**tructure
X-FEL	**X**-ray **F**ree-**E**lectron **L**aser
Å	**Å**ngström

Contents

Chapter 1

Introduction

1.1 Protein structure and function

Proteins are complex macromolecules responsible for most biochemical processes occurring within cells. They play crucial roles in for example DNA replication, nutrient metabolism, molecule synthesis, molecular transport, and signaling. The function of a protein is intimately linked to its structure, which is determined by its primary amino acid sequence. In proteins, there are 20 different amino acids with distinct chemical and structural properties, and the composition of amino acids in a protein determines its unique characteristics. Proteins exhibit hierarchical structures, including primary, secondary, tertiary, and quaternary structures. The primary structure refers to the linear sequence of amino acids, while the secondary structure involves local folding patterns stabilized by hydrogen bonds. The tertiary structure arises from the overall folding of secondary structure elements, and the quaternary structure consists of the association of multiple protein subunits. In many cases, the protein spontaneously folds into its native conformation, guided by the information encoded in its amino acid sequence. The hydrophobic and hydrophilic properties of the amino acids determine the protein's folding pattern, with hydrophobic regions buried in the core and hydrophilic regions exposed to the surrounding solvent [1]. It is essential to achieve the correct protein fold to function correctly, as the protein strives to reach the lowest energy conformation [2]. Some proteins act as catalysts for biochemical reactions, taking the reaction along a different energy pathway [3] and significantly accelerating reaction rates compared to non-catalyzed conditions. The structure

and dynamics of proteins are closely linked to their function. Structural changes in proteins can range from small-scale movements of individual amino acid side chains to large-scale rearrangements of secondary structure elements. These changes can occur on timescales ranging from femtoseconds to seconds. While mutational studies can identify amino acids critical for protein function, three-dimensional structural information is paramount for understanding the functional mechanisms of proteins. Scientists can uncover the intricate relationship between protein structure and function by examining protein homologs and structurally similar proteins with varying functions. Advances in structural biology techniques, such as nuclear magnetic resonance, electron microscopy, and crystallography, allow researchers to visualize proteins in their inactive and dynamic states [1].

1.2 Hemoglobin

Hemoglobin (Hb) is an iron-containing heme protein essential for oxygen transport. The protein is an assembly of four globular subunits, each containing a heme B (protoporphyrin IX group) [4]. Equine hemoglobin was among the first protein structures to be solved at high resolution [5]. It is a valuable model system for oxygen-sensitive metalloproteins due to its ubiquity and high but reversible affinity to oxygen. Deoxyhemoglobin (DeoxyHb) is missing a 6th ligand in the ferrous heme iron's coordination sphere (composed of the four heme nitrogens and histidine) and thus is very sensitive to the presence of oxygen; oxyhemoglobin (OxyHb) has one O_2 molecule bound to a ferrous heme iron; and methemoglobin (MetHb), the oxidized form of Hb, has a heme iron that is in the +3 oxidation state (ferric) with water bound in the 6th ligand position [6].

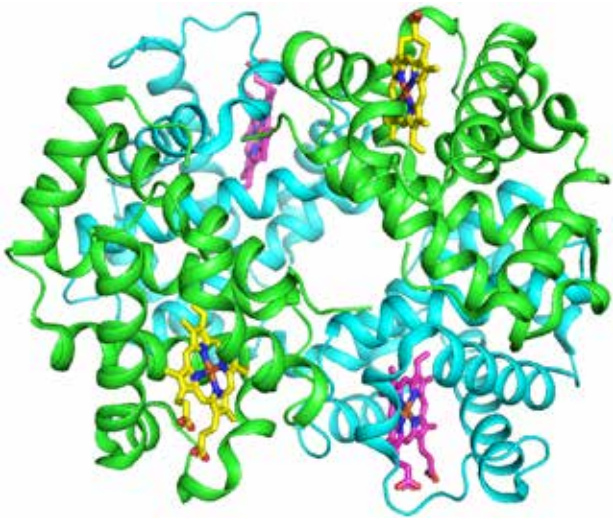

Figure 1.1: Structure of horse Hemoglobin. PDB ID: 1NS9. α-subunits in cyan, β-subunits in green

1.3 Lysozyme

Lysozyme, an antimicrobial enzyme produced by animals, is a vital component of the innate immune system, playing a critical role in defending against bacteria, viruses, and fungi. Its enzymatic activity involves catalyzing the hydrolysis of β-1,4-glycosidic bonds between N-acetylmuramic acid (NAM) and N-acetylglucosamine (NAG) in the polysaccharide backbone of peptidoglycans, which are significant components of Gram-positive bacterial cell walls. Lysozyme is abundant in various secretions, including tears, saliva, human milk, mucus, and egg white [7]. It exists in three main types: c-type (chicken or conventional type), g-type (goose type), and i-type (invertebrate type). Notably, hen egg white lysozyme exhibits remarkable thermal stability, with a melting point of up to 72 °C at pH 5.0. It retains activity within a broad pH range of 6 to 9, and its isoelectric point is measured at 11.35 [8]. In accordance with the Phillips mechanism, two crucial amino acid residues, specifically Glu35 (glutamic acid) and Asp52 (aspartic acid), play a pivotal role. The Glu35 residue's

terminal proton is translocated to the oxygen atom within the glycosidic bond connecting adjacent sugar residues, resulting in the cleavage of the glycosidic bond and the generation of a carbenium ion. This carbenium ion's positive charge finds stability through interaction with the negative charge of Asp52 until a hydroxyl ion attaches to the positively charged carbon atom, subsequently facilitating the reprotonation of Glu35 [9]. Due to its accessibility, stability, and ease of crystallization, lysozyme has become a staple protein in crystallography validation experiments.

Figure 1.2: Structure of hem-egg Lysozyme. PDB ID: 5NJM (different colors represent different secondary structures)

1.4 RuBisCO

Ribulose-1,5-bisphosphate carboxylase/oxygenase (RuBisCo) is a vital component of the light-independent phase of photosynthesis, specifically in the carbon fixation process. Its primary function involves converting atmospheric carbon dioxide into energy-rich molecules like glucose. RuBisCo is one of the most abundant enzymes on Earth and has existed for approximately four billion years, preceding the presence of oxygen. In leaves, it is the most abundant protein and consists of two protein subunits: a large chain (L) weighing approximately 55,000 Da and a small chain (S) weighing approximately 13,000 Da. The active substrate-binding sites are located within the large chains, forming dimers where amino acids from

each large chain contribute to the binding sites. Eight large chains (forming four dimers) and eight small chains assemble into a larger complex weighing approximately 540,000 Da. Magnesium ions (Mg^{2+}) are essential for the enzymatic activity of RuBisCO (yellow spheres in Figure 1.4), and they are held tightly by three amino acids: asparagine, glutamic acid, and a modified form of lysine. The initial step in activating RuBisCo is accomplished by carbon dioxide in a process involving the carbamylation of a lysine residue (Lys201 in the spinach enzyme). This process generates a binding site for a magnesium ion that stabilizes the carbamate and completes the enzyme's active site. [10]

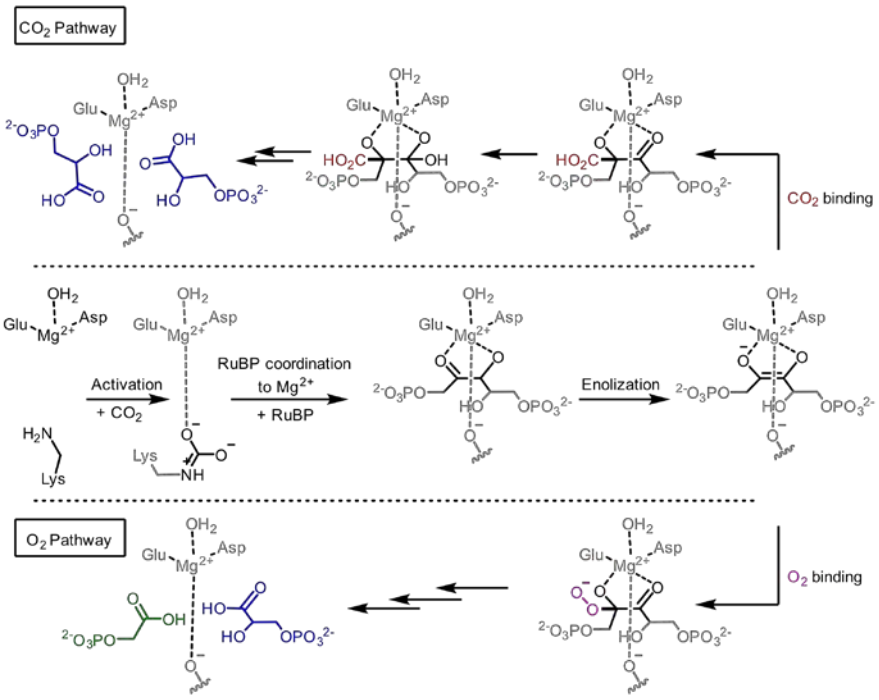

Figure 1.3: Schematic illustrating the enzyme-catalyzed reaction of RuBisCO with CO_2 or O_2 with RuBP to form 3-PGA.

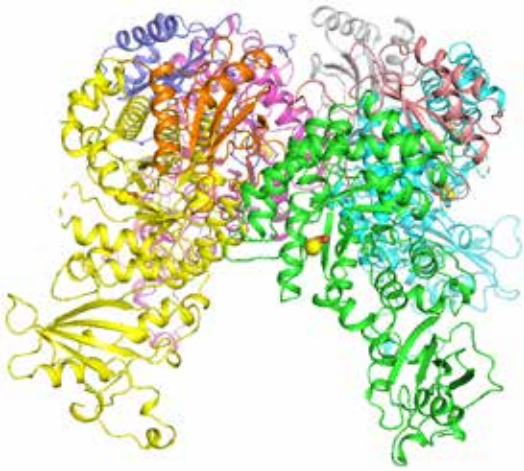

Figure 1.4: Structure of spinach RuBisCO. PDB ID: 1AUS (colors represent different subunits)

1.5 Cytochrome *c* oxidase

Cytochrome *c* oxidase (C*c*O) is an enzymatic complex involved in the process of respiration, specifically the reduction of molecular oxygen to water. It serves as the terminal enzyme in the respiratory chains of mitochondria and many bacteria. C*c*Os are integral membrane-bound complexes that facilitate the reduction of oxygen molecules to water, harnessing the released energy to translocate protons across the cell membrane. This electrochemical proton gradient stores free energy, which the cell utilizes for ATP synthesis and transmembrane transport. The study of C*c*Os has been the subject of extensive research over the past sixty years. Cytochrome *c* acts as an electron donor from the positive side of the membrane. At the same time, protons are simultaneously taken up from the negative side and transported to the heme a_3 - Cu_B active site, where the oxygen reduction reaction occurs. This process creates a charge separation across the membrane, which is further augmented by the active pumping of protons from the positive to the negative side of the membrane. Overall, the investigation of C*c*Os has provided valuable insights into the mechanisms

underlying respiratory processes and cellular energy generation. The intricate interplay between electron transfer, proton translocation, and oxygen reduction within these complexes contributes to our understanding of fundamental biological processes [11]. The thermophilic bacterium *Thermus thermophilus* (*T. thermophilus*) strain HB8 possesses two distinct terminal oxidases, ba_3 and caa_3, which are responsible for the reduction of oxygen to water. The crystal structure of the ba_3-type C*c*O, belonging to the B-type heme-copper oxidase (HCO) family, was the first B-type to be determined at a high resolution of 2.4 Å [12]. The ba_3-type C*c*O exhibits a unique electron acceptor role, receiving electrons from the thermostable cytochrome c_{552}. Notably, it demonstrates exceptional reactivity towards various ligands, including CN^-, CO, NO, O_2 and H_2O_2. These ligands bind to the heme a_3 site of the ba_3-type C*c*O [13].

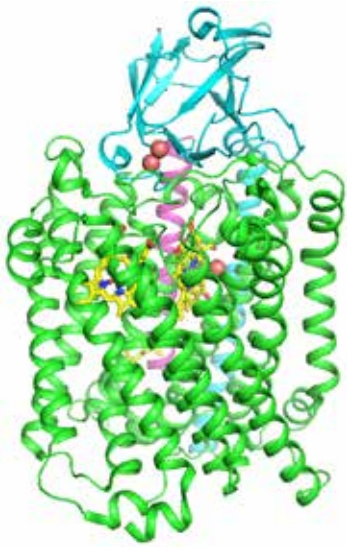

Figure 1.5: Structure of ba_3-type C*c*O. PDB ID: 3S8F, (colors present different subunits)

1.6 Cytochrome P450

Cytochromes P450 (commonly referred to as P450s or CYPs) are a diverse group of enzymes that utilize heme as a cofactor, primarily serving as monooxygenases. They play essential roles in various biological processes, including the oxidation of steroids, fatty acids, and xenobiotics in mammals. These enzymes are crucial for clearing various compounds from the body and for the synthesis and degradation of hormones. The groundbreaking work of Estabrook, Cooper, and Rosenthal in 1963 shed light on the role of CYP enzymes in steroid hormone synthesis and drug metabolism in mammals. The P450 enzymes have been identified across all domains of life, spanning animals, plants, fungi, protists, bacteria, archaea, and even viruses. P450s typically serve as the terminal oxidase enzymes in electron transfer chains, falling under the broad category of P450-containing systems. The name "P450" originates from the spectrophotometric peak observed at a wavelength of 450 nm when the enzyme is in its reduced state and bound to carbon monoxide. Most P450s require a partner protein to deliver one or more electrons, ultimately reducing the iron at the enzyme's active site and facilitating molecular oxygen reactions. The active site of cytochrome P450 contains a heme-iron center, with the iron linked to the protein through a cysteine thiolate ligand. This cysteine, along with several adjacent residues, exhibits high conservation among known P450s and conforms to the formal PROSITE signature consensus pattern [FW] - [SGNH] - x - [GD] - F - [RKHPT] - P - C - [LIVMFAP] - [GAD]. Due to the wide range of reactions catalyzed by P450s, the properties and activities of these enzymes can vary significantly. Some individual P450s, such as the main human isoform CYP3A4, can act on a diverse set of substrates. [14, 15]

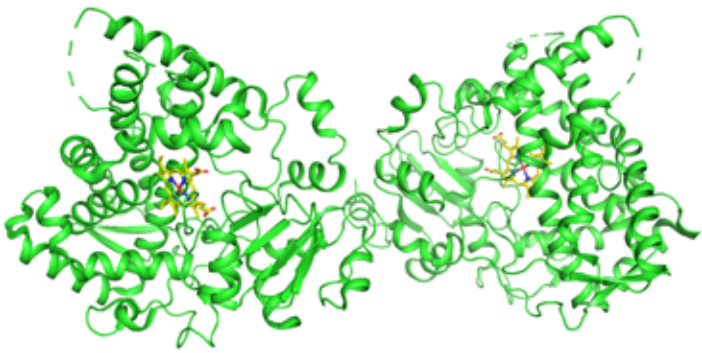

Figure 1.6: Structure of human CYP3A4. PDB ID: 5VCC

1.7 Structural determination of proteins

Despite their significant complexity and multitude of atoms, proteins cannot be directly observed under a microscope due to their small size. As a result, X-ray radiation has emerged as the primary method for protein structure determination. While Nuclear Magnetic Resonance Spectroscopy (NMR) can also be employed, its application is limited to smaller proteins due to the intricacies involved in the analysis. Cryo-electron microscopy, a rapidly advancing field, is yet to achieve consistently the same level of resolution and repetition as X-ray crystallography [16]. The breakthrough in protein structure determination using X-ray crystallography came in 1958 with the successful solution of myoglobin's structure [17]. Since then, the Protein Data Bank (PDB) has amassed over 200,000 protein structures solved through various techniques. X-ray crystallography stands as the predominant approach for investigating protein structures. This method involves the production of protein crystals, which are then illuminated with X-rays to generate diffraction patterns, serving as unique fingerprints of the protein's structure. Crystals are essential as the diffraction pattern arises from the constructive interference of orderly arranged molecules within the crystal lattice [1]. Synchrotron radiation, produced by particle accelerators called synchrotrons, is commonly employed as the X-ray source for structure determination [18–21]. The utilization of synchrotron

radiation has proven highly successful, facilitating the collection of diffraction data from diverse macromolecules. Advances such as employing cryogenic temperatures to mitigate radiation damage [22] and the ability to focus the X-ray beam to capture data from small crystals (10-15 µm) have further enhanced the technique. However, X-ray crystallography has its limitations. Firstly, it necessitates the generation of large (50 to 200 µm in size), well-diffracting crystals, which can present challenges. Specific proteins face difficulties in forming sizable crystals, while membrane proteins, with their hydrophobic nature, pose particular challenges for crystallization. Secondly, completely avoiding radiation damage is not feasible, which can impede the determination of the protein's native structure.

1.8 BioMAX

BioMAX is a beamline specialized in macromolecular crystallography at the MAX IV Laboratory 3 GeV storage ring. This storage ring is recognized as the pioneering operational multi-bend achromat storage ring, the first 4^{th} generation synchrotron. BioMAX uses the storage ring's low-emittance property to generate a parallel and high-intensity X-ray beam, which remains powerful even when focused to a minute size of 20 x 5 μm^2 using flexible focusing mirrors. The beam's energy can be adjusted within the 5–25 keV range using the in-vacuum undulator and the horizontally deflecting double-crystal monochromator. Essential equipment at BioMAX includes the MD3 diffractometer, the ISARA high-capacity sample changer, and the EIGER 16M hybrid pixel detector (Figure 1.8). The user-friendly MXCuBE3 graphical user interface facilitates data collection, while sample tracking is managed by ISPyB (EXI). MAX IV and the Lund University supercomputing center (LUNARC) support data storage and processing. BioMAX, equipped with cutting-edge instrumentation, extensive automation, intuitive interface, and remote operation capabilities, offers an exceptional facility for diverse macromolecular crystallography experiments, including the implementation of serial crystallography techniques. The various components of the system, ranging from the undulator to the detector, are illustrated in Figure 1.7. [21]

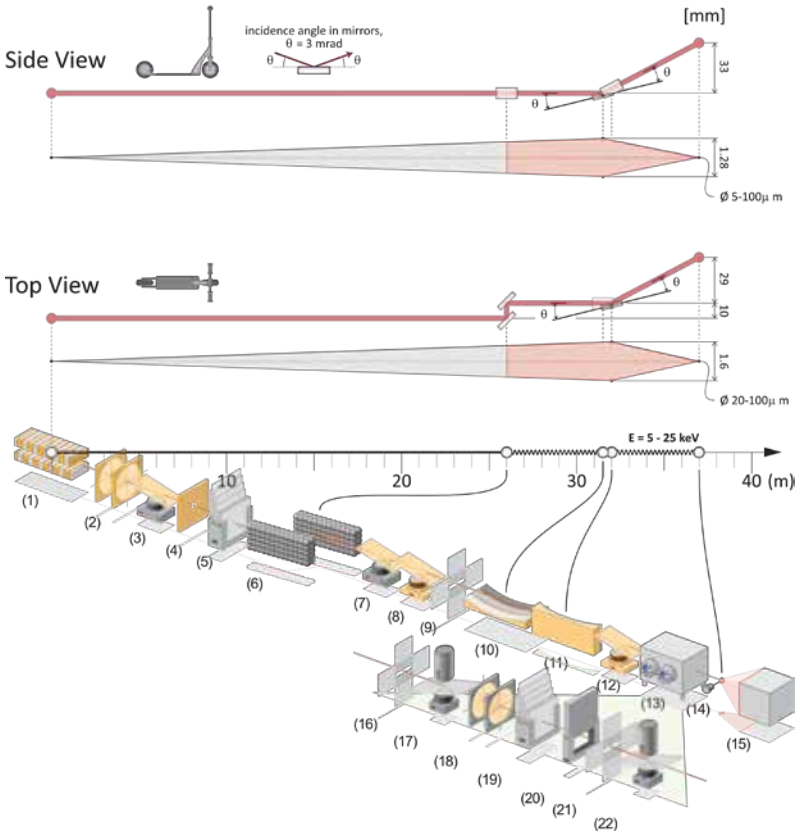

Figure 1.7: Beamline components from undulator to the detector: (1) undulator, (2) two front-end beam position monitors, (3) front-end fluorescent screen, (4) optics hutch fixed mask, (5) diamond filters, (6) double-crystal monochromator, (7) fluorescent screen, (8) NanoBPM, (9) slits, (10) vertical focusing mirror, (11) horizontal focusing mirror, (12) NanoBPM, (13) BCU, (14) sample and (15) detector. The components in the BCU chamber are shown in the enlargement and include (16) slits, (17) beamviewer/intensity monitor, (18) two diamond beam position monitors, (19) attenuators, (20) shutter, (21) slits and (22) beamviewer/intensity monitor.

Figure 1.8: BioMAX experimental hutch: a) EIGER 16M detector, b) REX with HClab and cryo-jet, c) Arinax MD3 microdiffractometer, d) BCU, e) ISARA sample changer.

1.9 MicroMAX

The MicroMAX beamline is an impressive piece of engineering, explicitly designed for microfocus macromolecular crystallography. It offers unparalleled capabilities that set it apart from other systems. With a focal spot beam diameter of 1 μm^2 and an X-ray flux of over 10^{13} photons/sec in monochromatic mode and approaching an impressive 10^{15} photons/sec in polychromatic mode, MicroMAX is a versatile tool for a wide range of scientific investigations. It can collect oscillation data from 10 µm crystals, comparable to BioMAX capabilities, and conduct cutting-edge time-resolved, serial crystallography experiments employing micrometer-sized crystals. The modular setup of MicroMAX ensures seamless adaptability to different sample environments, enabling researchers to use the most suitable sample delivery system and data collection methodology tailored to each specific case. Additionally, the high-performance goniometer and the high-capacity sample changer in EH1 enable data collection that will rival the performance of standard MX beamlines.

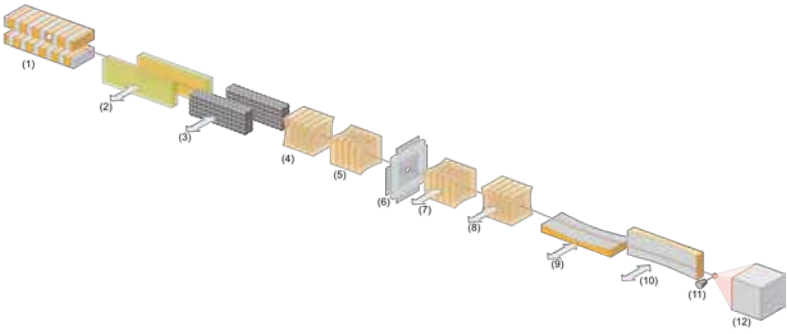

Figure 1.9: MicroMAX optics layout. (1) in-vacuum undulator (IVU), (2) multilayer monochromator (MLM), (3) horizontal double crystal monochromator (HDCM), (4) compound refractive lenses (CRL1 2D), (5) compound refractive lenses (CRL2 1D), (6) secondary source horizontal (SSh), (7) compound refractive lenses (CRL3 1D), (8) compound refractive lenses (CRL4 2D), (9) vertically focusing mirror (VFM), (10) horizontally focusing mirror (HFM), (11) Sample, (12) Detector

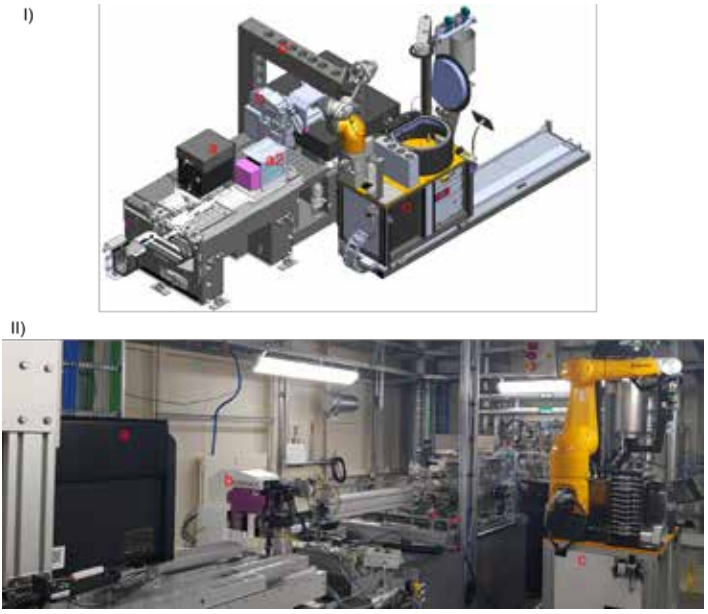

Figure 1.10: MicroMAX experimental hutch 1: I) CAD drawing of final hutch version, II) current hutch; a) DECTRIS EIGER2 X CdTe 9M detector, a2)PSI JUNGFRAU 4M (Si) detector, b) Arinax MD3-UP microdiffractometer, c)IRELEC ISARA sample changer, d) Gantry for auxiliary equipment.

1.10 Aim of work

Serial crystallography is a growing developing field with different methods of collecting data. The aim of this thesis was to implement and develop serial synchrotron crystallography methods (SSX) at BioMAX and prepare the ground for the newly built beamline, MicroMAX, that will be dedicated to SSX.
Chapter IV focuses on fixed-target SSX development, which Papers I and III also support.
Chapter V is focused on flow-cell SSX development, which Paper II supports.
Chapter VI explains the development and preparation for TR-SSX at BioMAX, whereas Paper IV supports the beginning of that.

Chapter 2

Sample preparation for X-ray crystallography

2.1 Protein expression

The isolation of a target protein is commonly accomplished using two main strategies: extraction from its natural source or utilizing recombinant DNA techniques [23]. It is important to acknowledge that many targets in structural biology exhibit limited expression levels within their native host cells. Fortunately, the development of recombinant protein expression has provided an effective solution to this challenge. In this approach, the gene encoding the protein of interest is cloned and strategically inserted into a tailored DNA vector optimized for efficient expression [24]. Subsequently, the modified vector is introduced into a suitable host system, such as an *E. coli* strain [25], enabling protein production at significant quantities.

The initial phase of protein purification involves cell lysis, which encompasses the cell wall disruption through various means, such as using lysozyme or conventional mechanical forces like high-pressure or high-frequency sound waves. Mechanical methods, like the French press or Emulsiflex, employ considerable pressure to force the cells through narrow passages, ultimately leading to cell rupture and release of intracellular contents. These high-pressure methods increase temperature, so cells are cooled to approximately 4 °C before pressing. Following the cell lysis step, centrifugation is employed to effectively separate and eliminate unbroken cells and cellular debris from the protein solution.

The subsequent stage involves utilizing various chromatography techniques, which exploit the distinct physical properties of proteins, such as size, charge, or binding affinity, to effectuate their separation. While specific chromatographic methods may differ, they all adhere to a fundamental principle: the presence of two phases, a stationary phase and a mobile phase. In the context of protein purification, column chromatography is commonly used. This technique involves a column packed with a resin serving as the stationary phase, while the mobile phase consists of a buffer solution that travels through the column. During column chromatography, proteins in the mobile phase interact with the stationary phase in distinct ways dictated by their unique properties. Consequently, these interactions lead to differential retention of proteins within the column. Using the mobile phase, the separated proteins are subsequently eluted from the column in fractions. The final purification step often involves using size exclusion chromatography (SEC), which effectively separates proteins based on size. Smaller proteins enter the minuscule pores within the column material and thus exhibit longer retention times than larger molecules [1].

In this project, we used Lysozyme, Hemoglobin, RuBisCO, CYP3A4, sHE and CcO. Lysozyme and Hemoglobin were purchased from Sigma-Aldrich, while RuBisCO was purified from spinach leaves. CcO, sHE and CYP3A4 were purified and crystallized at the University of Gothenburg.

2.1.1 RuBisCO purification

Purification of RuBisCO was made from homogenized fresh spinach leaves. After preparation of soluble extract using filtration followed by centrifugation, ammonium sulfate precipitation was performed. The 30-50 % fraction was dissolved in 5 mM KH_2PO_4, 0.1 mM EDTA, 1 mM DTT, pH 7.6 (=IEX start buffer) and then dialyzed to the same buffer before loading it to a HiLoad 26/10 HP Q column (GE healthcare) for purification by anion exchange chromatography. Elution was done using a gradient from 5-250 mM KH_2PO_4 with 0.1 mM EDTA, 1 mM DTT at pH 7.6 with a step at 145 mM KH_2PO_4, before the RuBisCO peak. After analysis by SDS-PAGE, the RuBisCO containing fractions were pooled, concentrated and then further purified by gel filtration using a HiPrep 26/60 Sephacryl S-300 HR column (GE Healthcare) in 20 mM HEPES, 5 mM $MgCl_2$, pH 8.

Finally the protein was concentrated, aliquoted and snap-frozen in liquid nitrogen. The final protein is described in Table 2.1 and Figure 2.1.

Table 2.1: Summary of purified spinach RuBisCO batch. *The purity of proteins was estimated using SDS-PAGE analysis. ** Calculated using 0.61 x Abs280 [26]

Protein	Spinach RuBisCO
Purity*	> 95 %
Concentration**	65.6 mg/mL
Buffer	20 mM HEPES, 5 mM $MgCl_2$, pH 8.0
Volume	6.9 mL
Mass	452 mg

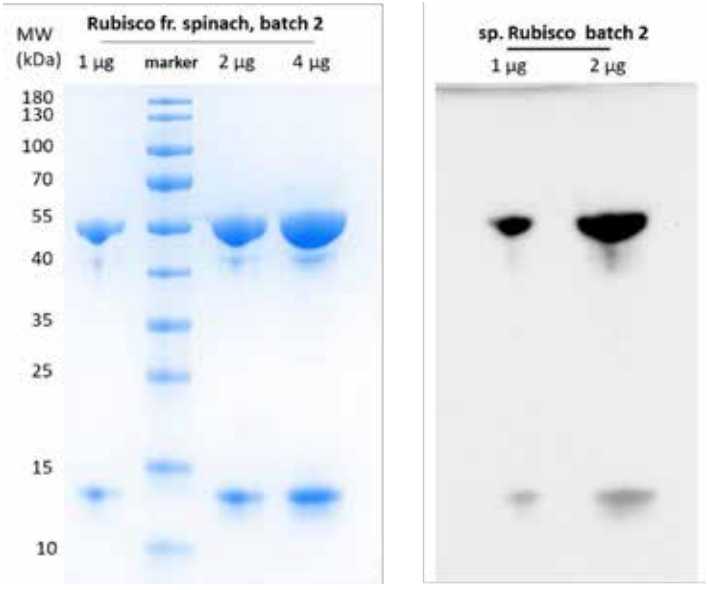

Figure 2.1: 1, 2 and 4 µg of RuBisCO from spinach batch 2 was analyzed on an SDS-PAGE gel (left) and 1 and 2 µg was also analyzed by Western blot using an anti-RuBisCO antibody. The purity is estimated to >95 %.

2.2 Crystallization

Crystallization is a well-ordered phase transition involving the transformation of a substance from a liquid to a solid state. As a result of this orderly arrangement, crystals form as solid structures comprising atoms, molecules, or ions, exhibiting a repetitive and well-defined pattern extending in three dimensions. Their regularity grants them inherent symmetry and allows diverse crystal systems and lattices to be adopted. The fundamental building blocks of crystals are unit cells, representing the smallest entities from which the entire crystal lattice can be constructed through translation operations. The unit cells can be further subdivided into what is known as the asymmetric unit - a minute portion of the crystal that can be translated or rotated via symmetry operations, ultimately forming the complete unit cell. The determination of optimal crystallization conditions for individual proteins is a particular process, as various conditions (pH, buffer, salt, temperature etc.) can yield crystals with varying qualities and different types of crystal contacts. The screening and optimization of crystal conditions often involve iterative steps, demanding both time and a substantial amount of sample, where the successful crystallization of a protein is never guaranteed. Factors such as high conformational flexibility or insufficient crystallization contacts of the protein can hinder finding suitable crystallization conditions altogether. Even when crystals are obtained, they may require numerous rounds of optimization, wherein conditions are subtly modified, results are evaluated, and further optimizations are performed. Crystallization trials typically involve setting up small microliter (µL) droplets. These droplets consist of a mixture of the protein of interest and a precipitant solution containing a precipitating agent. The four main methods for crystalization are: dialysis, microbatch, vapor diffusion and free interface diffusion [1].

2.2.1 Vapor diffusion crystallization

This method encloses the droplet within a sealed environment alongside excess reservoir solution. The droplet can be placed either in a hanging or sitting position (Figure 2.2). Using a sitting drop allows for larger droplets, whereas hanging drops offer benefits such as conservation of the sample

and ease of crystal harvesting. The reservoir solution contains the same precipitant as the droplet but at a higher concentration. This establishes a vapor diffusion mechanism, whereby water migrates, from the droplet to the reservoir until an equilibrium is achieved within the sealed system. Since the crystallization process relies on achieving supersaturation of the molecules in the solution, the solubility diagram of the droplet conditions plays a crucial role in governing the crystallization process (Figure 2.3) [27].

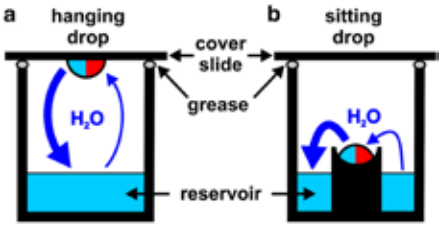

Figure 2.2: Vapor diffusion crystallization techniques. a) Hanging drop, b) sitting drop setup. (Reproduced with permission from reference [28], https://creativecommons.org/licenses/by/4.0/)

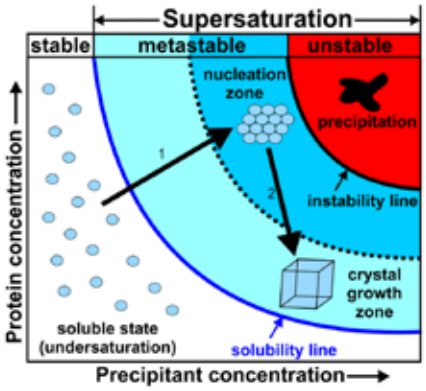

Figure 2.3: Phase diagram of protein crystallization. (Reproduced with permission from reference [28], https://creativecommons.org/licenses/by/4.0/)

The gradual evaporation of water from the droplet reduces available water molecules for protein hydration, leading to a decrease in protein solubility. If the protein and precipitant concentrations become excessively high, they will enter the precipitant zone. Under such conditions, the protein tends to form amorphous precipitates rather than well-ordered crystals. On the other hand, if the concentrations are too low, the droplet will reside in the undersaturation zone, and the protein will remain in the solution without crystal formation. Ideally, the initial conditions of the droplet should lie within the metastable zone. As the water content decreases, the droplet's protein and precipitant concentrations increase, as shown by arrow 1 in Figure 2.3. Upon entering the nucleation zone, small nuclei start forming, initiating protein crystal growth. During crystal growth, the protein concentration gradually decreases, following arrow 2 in Figure 2.3, until it reaches the solubility curve, at which point crystal growth stops [29].

2.2.2 Micro-crystallization

Traditional single X-ray crystallography typically relies on data acquisition from large single crystals. However, microcrystals may be the only ones available in certain cases, or specific methods like SSX and SFX necessitate smaller sample sizes [30]. Furthermore, working with microcrystals offers inherent advantages, including reduced mosaicity and enhanced robustness. The latter characteristic renders microcrystals less susceptible to detrimental effects resulting from cryocooling, ligand soaking, or light exposure in pump-probe studies [31]. There are various approaches to obtaining micro-crystals, with batch and vapor diffusion methods being the most commonly used. In the batch method, protein and precipitating agents are mixed to reach the nucleation zone promptly [32]. Alternatively, micro-crystals can be derived from macro-crystals by crushing them using techniques like vortexing or a glass crusher. However, this approach may introduce heterogeneity into the sample. To address this, the crystals can be filtered, although this may lead to sample loss and potentially impact the experiment's success. Physical crushing of the crystals may also result in increased mosaicity and broadening of Bragg peaks. As an alternative, crushed macro-crystals can be used for seeding, where small fragments

of existing crystals (seeds) are introduced. This seeding process enhances the nucleation rate and the yield of micro-crystals, mitigating some of the challenges associated with their preparation [33].

2.2.3 LCP crystallization

The Lipid Cubic Phase (LCP), also known as the in-meso approach, is a well-established method for crystallizing membrane proteins. During the solubilization process and the use of detergents in protein purification, the native conformation of the protein can be disrupted, sometimes resulting in loss of protein function. The LCP method addresses this issue. This technique involves the addition of lipids to the purified integral membrane protein solution, aiming to mimic the protein's native environment. The most commonly employed lipid is monoacylglycerol monoolein (MAG), which forms a mesophase in the presence of water [34]. In practice, the pure concentrated protein and monoolein are mixed in an approximately 40:60 lipid ratio. Initially, the protein and monoolein are separately loaded into two glass Hamilton syringes connected by a coupler, and they are then mixed by applying alternating pressure to the plungers of the syringes. Once the cubic phase is formed, a batch crystallization approach can be initiated. The LCP-protein mixture is extruded from the syringe and brought into contact with crystallization buffers in a crystallization plate. The transformation from a cubic phase to a lamellar phase brings proteins in a position to form contacts between bilayers through their soluble domains. This process aims to initiate the nucleation phase and promote crystal formation by utilizing specifically selected crystallization buffers [35].

2.3 RuBisCO microcrystals

Due to the absence of reported structures of spinach RuBisCO (SpRub) microcrystals and incompatibilities with older protocols for obtaining large single crystals [36], our approach involved initial screening experiments. Two screens, namely MD JCSG+ and MD PACT premier (Molecular Dimensions, UK), were used in 96-well plates, with each well containing

three drops at different protein-to-buffer ratios (1:1, 2:1, 1:2). Promising conditions identified during the screening phase were reproduced and further optimized in 48-well plates for optimization and crystal harvesting. Through multiple iterations of crystallization and data collection, we successfully obtained four conditions that produced large, well-diffracting single crystals. These conditions were selected for further optimization in order to obtain microcrystals. Ultimately, microcrystals of SpRub were successfully obtained using the sitting drop method, utilizing an HR1-002 plate (Hampton Research), at a temperature of 20 °C. The crystallization process involved the activation of SpRub prior to setup [37]. The specific conditions used were as follows: 5 µL of SpRub solution at a concentration of 15 mg/mL (in a buffer of 20 mM HEPES, 5 mM $MgCl_2$, pH 8.0), combined with 5 µL of reservoir solution (0.2 M $MgCl_2$x6H_2O, 0.1 M Tris pH 7.0, 12% w/v PEG 8000). The total well volume was 500 µL.

2.4 Lysozyme microcrystals

Chicken egg white Lysozyme (Sigma, CAS-12650-88-3) was dissolved at a concentration of 50 mg/mL in 100 mM Na Acetate pH 3.0. Of this lysozyme solution, 500 µL were mixed with 500 µL of precipitant, 19.04 % NaCl, 5.44 % PEG 8,000, 68 mM Na Acetate pH 3.0 in an Eppendorf tube and incubated overnight at 20 °C. Crystals grown in batch were spun down at room-temperature with 2,000 g for 1 min. Almost all supernatant was removed and crystals were re-suspended using a 200 µL pipette [32].

2.5 Hemoglobin microcrystals

Equine hemoglobin (Sigma, CAS-9047090) stock solution of 20-25 mg/mL was prepared in 10 mM HEPES, pH 7.5 and crystalized using the stirred batch method [38] by mixing into precipitant solution (26 %v PEG3350, 10 mM HEPES pH 7.5). At 20 °C 500 µL of precipitant was added to 250 µL protein solution. The mixture was stirred in small HPLC vials with rice corn-sized stir bars on a magnetic stirrer for about 20h, after which crystals of 5x5x5 μm^3 size were obtained.

Chapter 3

Methods

3.1 Theory of light scattering and X-ray diffraction

3.1.1 What X-rays are, and how they are generated at Synchrotrons

X-rays are electromagnetic waves characterized by wavelengths ranging from 10^{-12} meters to 10^{-9} meters, as represented in Figure 3.1. They are classified into soft and hard X-rays based on their energy levels. Hard X-rays, in particular, find extensive utilization in medical applications and are prominently employed in X-ray crystallography due to their exceptional penetrating ability. X-ray crystallography is a formidable scientific methodology for determining the structural characteristics of molecules or complexes arranged in a crystalline lattice, achieving atomic-level resolution. This technique relies on the unique suitability of X-rays for this purpose, primarily attributed to their wavelengths falling within the range of 0.1 to 1 Å. This particular range aligns well with the interatomic spacing within the molecule of interest, facilitating an optimal exploration and detailed examination of the molecular architecture [39].

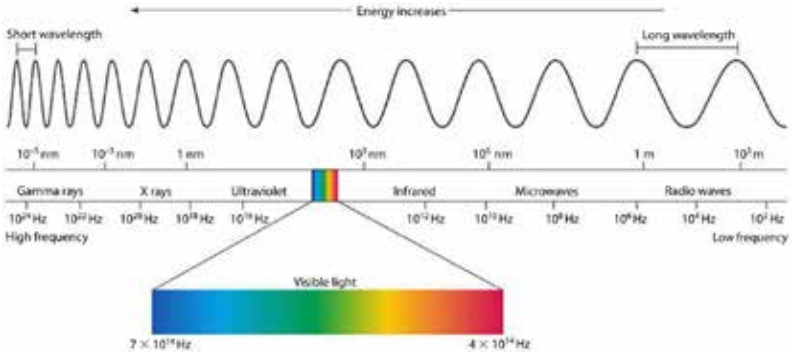

Figure 3.1: Electromagentic spectrum (Reproduced with permission from [40]).

A synchrotron, a circular-shaped particle accelerator, uses electromagnetic fields to accelerate electrons to relativistic energies, generating electromagnetic radiation. Its structure comprises several essential components: a LINAC (linear particle accelerator), a storage ring, and beamlines, also some have a booster synchrotron. The process begins with the LINAC, where electrons receive their initial acceleration before being injected into the ring or booster. Within the storage ring, electrons travel at velocities near the speed of light, and the machine maintains their energy at a constant value. The storage ring contains both straight and curved sections. The straight segments feature undulators, up to 5 meters in length, where electrons are guided through an array of magnets along a sinusoidal path, producing X-rays as a result. The curved sections of the storage ring are equipped with bending magnets, which compel electrons into a circular orbit. As the electrons change direction in these magnets, they emit synchrotron radiation and lose energy. Finally, the synchrotron facility encompasses beamlines extending from the storage ring. Each beamline is tailored to specific research purposes, equipped with setups optimized for distinct scientific investigations [41].

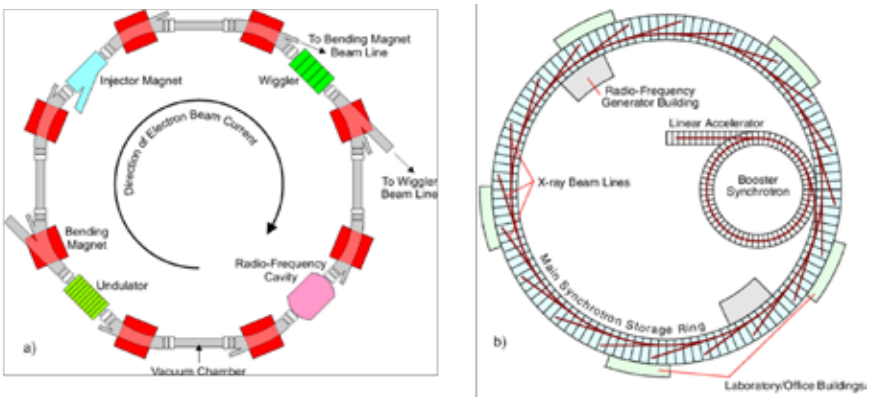

Figure 3.2: Example of synchrotron layout (Reproduced with permission from [42]).

3.1.2 X-ray diffraction

During the early 20th century, Lawrence Bragg and his father, William Bragg, made a significant discovery by observing that when X-rays interacted with a crystal, they scattered at specific angles. This discovery led to the formulation of Bragg's law and marked the beginning of crystallography as a field of study [43]. The following equation represents Bragg's law: $n\lambda = 2d\sin\theta$, where n is a positive integer, λ denotes the wavelength of the X-rays, d represents the spacing between two lattice planes in the crystal, and θ is the scattering angle (Figure 3.3b). This law signifies that when X-rays interact with the crystal, the electrons within its structure scatter the waves, leading to constructive interference and resulting in Bragg reflections. Each set of lattice planes is considered an independent diffractor, generating reflections with varying intensities based on the electron density distribution within the unit cell. Higher electron density allows for more X-ray scattering, increasing the scattered beam's intensity. The relationship between the diffraction angle θ and the distance between lattice planes, d, is inverse. Larger unit cells with greater spacing result in smaller θ, leading to an increased number of reflections within a specific angle from the incoming X-ray beam. This relationship is visually depicted by the distance OP (Figure 3.3a), equivalent to d^{-1}. A mathematical construction called the reciprocal space is used to analyse

Bragg reflections. The planes within the crystal and their corresponding directions can be illustrated using Miller indices, denoted as h, k, and l. To generate a reflection, reciprocal lattice points must be arranged in a specific manner to satisfy Bragg's law. In order to satisfy Bragg's law and produce reflections, reciprocal lattice points must intersect with the Ewald's sphere [44]. To effectively sample all of the reciprocal space, all reciprocal lattice points must be brought into diffracting conditions. This can be achieved by rotating the crystal around one axis, causing more reciprocal lattice points to meet Bragg's law by crossing Ewald's sphere. The minimum degree of rotation required depends on the symmetry of the unit cell, with higher symmetry requiring less rotation in order to record complete diffraction data, where completeness represents that fraction of possible symmetry-related diffraction spots that are sampled in a given experiment [45].

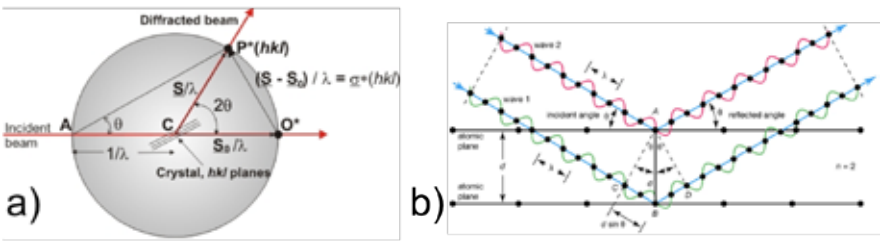

Figure 3.3: a) Ewald's sphere (Reproduced with permission from [46]); b) Bragg's law (Reproduced with permission from [47]).

3.2 XANES

X-ray Absorption Near Edge Structure (XANES) is the spectral part of X-ray Absorption Spectroscopy (XAS) that focuses on the absorption fine structures in proximity to an absorption edge (a sharp discontinuity in the absorption spectrum of a substance). This region spans approximately 10 eV below and 20 eV above the absorption edge. It is characterized by notable fluctuations in the X-ray absorption coefficient and is often dominated by intense, narrow resonances. With this technique you are probing

the molecular orbitals depending on the ligands coordinating the absorbing atom. The edge position depends on the oxidation state and ligand coordination. It's an element-specific bulk technique, meaning seeing all the excited atoms in the sample at the same time. Because of that, it is a valuable technique for obtaining insights into the electronic structure of unoccupied energy levels, and only a limited number of methods can achieve this level of detail. XANES is employed for hard X-ray spectra, particularly in coordination chemistry and metal atom studies [48, 49].

3.3 Vanilla crystallography

In vanilla or standard macromolecular crystallography experiments, a crystal is mounted on a support (goniometer) and rotated around the ω axis, perpendicular to the X-ray beam. Before data collection, various parameters can be adjusted, such as the detector distance, total number of images collected, oscillation range, exposure time, X-ray transmission, and X-ray wavelength [50]. Data collection can be performed at room temperature or under cryogenic conditions, each with its own advantages and drawbacks. At room temperature, we can observe a protein structure closer to its native state and conduct time-resolved experiments, but there is a higher risk of radiation damage. On the other hand, cryo-temperatures significantly reduce the issue of radiation damage, but real-time experiments become less feasible [1]. It is also good to mention that there is a form of time-resolved experiment under cryo-temperatures called cryo-trapping. With this method we have lower radiation damage compared to room temperature but we are limited with what speed of reactions we can follow [51]. Radiation damage can occur in general or specific ways. General damage is evident during data collection through reduced reflection intensity and increased mosaicity. Specific damage can be observed by analyzing electron density maps using software like COOT [52], which highlights changes in aspartates, glutamates, tyrosines, and methionines. Additionally, X-ray exposure may affect proteins with cofactors/prosthetic groups through water radiolysis [53, 54]. To preserve the lattice structure, which the presence of ice may disrupt, and to avoid ice rings in the diffraction pattern, cryoprotectants are used in cryo-crystallography.

A typical cryo-crystallography setup involves a stream of cold nitrogen gas directed toward the sample to maintain a constant temperature, preventing radiation damage and ice formation [55]. Modern cryo-crystallography experiments are often automated (from sample changer, data collection to data processing), enabling remote data collection, making it a convenient and efficient method in current crystallographic studies [21, 56–58].

3.4 Serial Synchrotron Crystallography

Obtaining large crystals for X-ray crystallography can be challenging in certain cases. Furthermore, smaller crystals allow shorter mixing times for mixing experiments, so microcrystals are better suited for those. Also, radiation dose plays a role, where if we have a smaller crystal that is replenished after X-ray exposure [59] we can go with a higher intensity beam compared to a single crystal experiment. This is where an alternative approach known as serial crystallography comes into play. Serial crystallography entails passing many crystals through the X-ray beam to obtain thousands of partial diffraction patterns. The orientation of each crystal is considered random, and multiple measurements are made for each Bragg peak to improve data quality. This approach is commonly employed at room temperature and uses crystals typically ranging from several microns to 50 µm in size. Before starting a serial crystallography experiment, several prerequisites must be met. Firstly, the beam size should be smaller or equal to that of the microcrystals to optimize the signal-to-noise ratio. Secondly, an appropriate sample delivery system needs to be chosen. Thirdly, a fast detector capable of collecting millions of frames within a limited time frame, typically one or two beamtime shifts, is essential. Lastly, a substantial quantity of high-quality crystals must be produced to ensure the success of the experiment [60]. This method originated at XFELs [61, 62] and has since been further advanced and adapted for use at synchrotrons, leading to its distinct designation as Serial Synchrotron X-Ray Crystallography, later just Serial Synchrotron Crystallography, from which the acronym SSX derives [63].

3.5 Sample delivery in SSX

For Serial Synchrotron Crystallography, the delivery of the crystals can be achieved in three ways: the sample flows from an injector (flow-based), the sample is laid on a fixed target and a hybrid of the two.

3.5.1 Flow-based

Flow-based methods developed with GDVN [64] (Gas Dynamic Virtual Nozzle) and HVE [65] (High Viscosity Extruder) at XFELs. However, using a GDVN results in significant sample consumption, ranging from 10 to 100 milligrams per data set. Additionally, the high flow rate of 10 m/s leads to a limited crystal-X-ray interaction time when translating through an X-ray beam, thereby reducing the amount of diffraction data measurable at synchrotron facilities [60]. Consequently, there has been a pressing demand for innovative approaches to minimize sample consumption and adapt methods for synchrotrons. Addressing this need, the HVE injector has emerged as a viable solution and has been adapted for use in synchrotron facilities as well [66]. As a result, two main categories of methods have been developed: LCP-based techniques and solution-based techniques.

3.5.1.1 LCP-based

When employing this type of injector, the sample is either grown in LCP media or diluted by combining it with a viscous medium. Various options for viscous media are available, including monoolein, agarose, grease, vaseline, hyaluronic acid, and hydroxyethyl cellulose (HEC) [67]. The selection of the carrier is primarily based on enhancing the survival probability of the crystals embedded within the material. In the case of the HVE method, the crystal sample embedded in a matrix is loaded into a reservoir, over which a Teflon ball is positioned (which will get distorted with pressure to ensure the system is sealed). A piston is pressed down (which is achieved by applying pressure to the piston) on the Teflon ball, effectively extruding the sample. To ensure the stream remains perpendicular to the x-ray beam (Figure 3.4), a gas stream (helium or nitrogen) is introduced coaxially to the crystals slurry [30, 66]. An additional technique, the Serial-X

flow-cell, employs Hamilton syringes driven by a CETONI Low Pressure Syringe Pump Nemesys 290 N. The sample is then directed through a glass capillary with a wall thickness of 10 µm (Figure 3.5) [68].

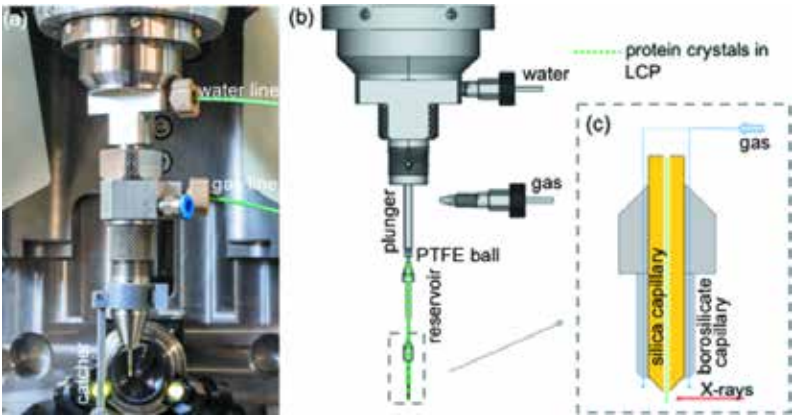

Figure 3.4: HVE setup at BioMAX [30].

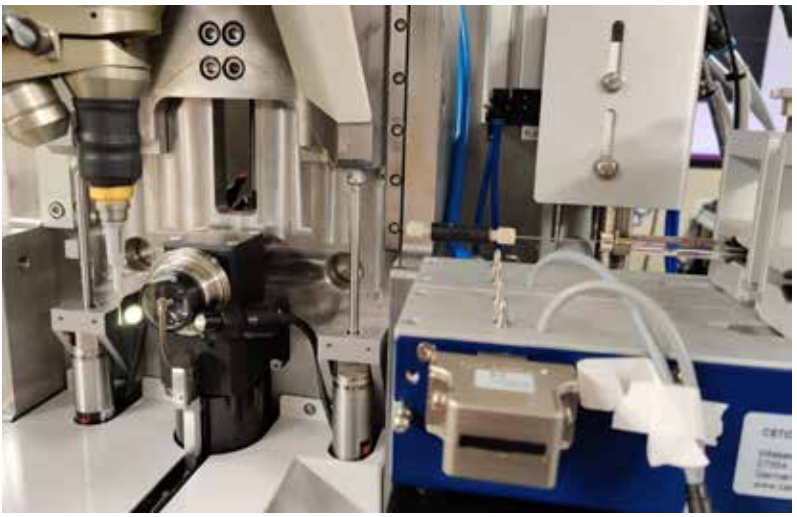

Figure 3.5: Serial-X flow-cell setup at BioMAX [68].

3.5.1.2 Solution-based

Some samples cannot be mixed with viscous media due to their inability to survive (from dissolving upon mixing with viscous matrix to poorer diffraction quality), and mixing experiments under such conditions are quite challenging. To overcome these difficulties, solution-based techniques have been developed. One such technique was pioneered at PETRA III on the P11 beamline, where thin-walled glass capillaries with 10 µm walls and 100 µm inner diameter were used to facilitate a flow of crystal suspension [63]. One drawback of the capillary method is the additional background scattering from capillary walls and crystallization solution inside the capillary. An alternative approach is using acoustic droplet ejection (ADE) [69] (Figure 3.6a), which allows for "drop-on-demand" delivery of samples, ejecting them only when necessary. This method reduces sample consumption significantly and enables data collection at both room and cryogenic temperatures. Moreover, there have been further advancements in this field, such as using microfluidic chips, including 3D-MiXD at ESRF [70] (Figure 3.6c) and AdaptoCell (Figure 3.6b) at MAX IV (which is currently in the final stages of development).

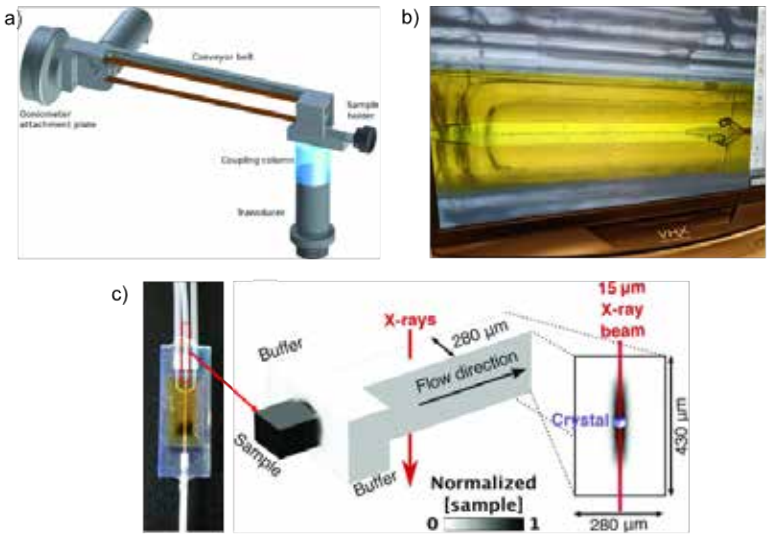

Figure 3.6: Solution-based SSX techniques. a) ADE at NSLS [69], b) AdaptoCell at BioMAX, c) 3D-MiXD at ESRF [70] (Reproduced with permission from the journals).

3.5.2 Fixed-target

Fixed-target methods emerged as a viable alternative to injector methods, aimed at enhancing the sample hit-rate and minimizing sample consumption in the experiments. In theory, fixed-target methods have the potential to achieve a hit-rate of 100% and significantly reduce sample consumption to the microgram scale. Additionally, these methods offer the flexibility of collecting data at both cryogenic and room temperatures [60]. Fixed-target methods can be divided into high-degree rotation and low-degree rotation.

3.5.2.1 High-degree rotation fixed-target

This fixed-target method employs supports that are compatible with SPINE holders, enabling their utilization on a wide range of beamline goniometers and ensuring compatibility with sample changers. Due to their specific dimensions and alignment, these supports can rotate up to 90° during the

data collection, limited by the risk of collision with beamline apertures. In Figure 3.7, we can see currently available solutions.

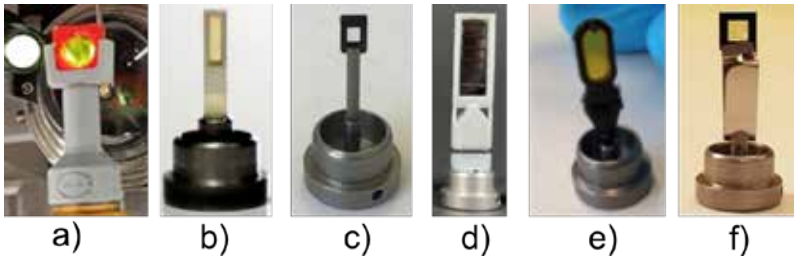

Figure 3.7: High-degree rotation fixed-targets. a) Serial-X, b) MiTeGen [71], c) SwissMX [72], d) Suna [73], e) XtalTool [74]. f) Silson [75]

3.5.2.2 Low-degree rotation fixed-target

Implementing this fixed-target method necessitates the modification of the goniometer, either by substituting its head or employing an alternative component. These supports are characterized by significantly larger dimensions and offer either restricted rotation, up to 20 degrees, or lack rotational capability altogether. Figure 3.8 showcases some presently available solutions, among which the silicon chips represented as a, b, and c hold a notable advantage. Specifically, each crystal is securely housed within its individual slot, resulting in minimized instances of multi-shot images and reduced solvent surroundings for the crystals, contributing to a lower background signal (solvent is extracted after chip loading). On the other hand, a significant benefit of in-situ data collection is the preservation of crystals within their native environment, mitigating potential disruptions caused by their removal. However, this approach exhibits a higher background signal.

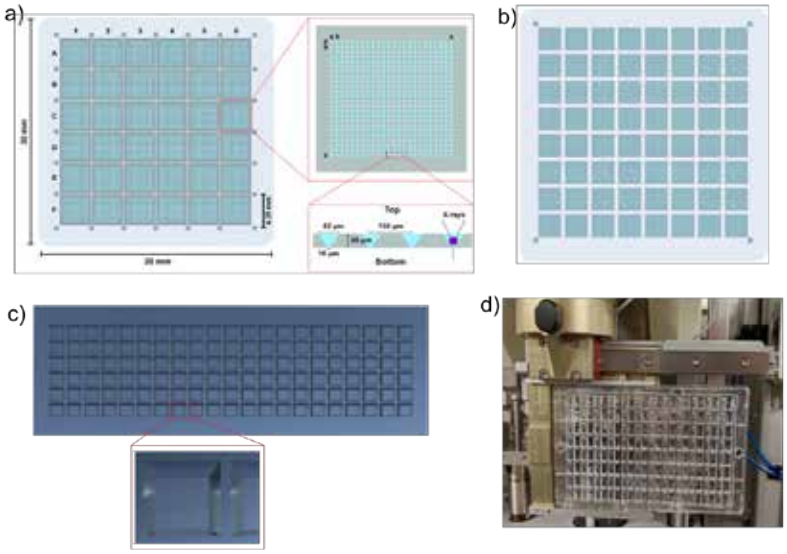

Figure 3.8: Low-degree rotation fixed-target. a) HARE chip [76], b) Oxford chip [77], c) Roadrunner II [78], d) In-situ plates [58, 79–81] (Reproduced with permission from the journals).

3.5.3 Hybrid methods

The tape drive is an innovative hybrid method that effectively combines the strengths of both fixed-target and flow-based sample delivery systems, making it a versatile and efficient solution for crystallography experiments. In this technique, crystals are suspended in a capillary, and small droplets are accurately deposited onto a moving tape. The tape then positions the crystal droplets precisely in front of an X-ray beam, creating a continuous and steady stream of crystal samples fed to the beam. One of the significant advantages of this technique is its capability to facilitate mixing experiments. Crystal solutions can be combined with other solutions just before deposition on the tape, opening up new possibilities for advanced research [82]. Currently, two types of tape drives are available to use at synchrotrons: one developed by CFEL [83] (Figure 3.9a) and the other by Suna-Precision GmbH (Figure 3.9b). There is another one under development at ESRF ID29 beamline [84].

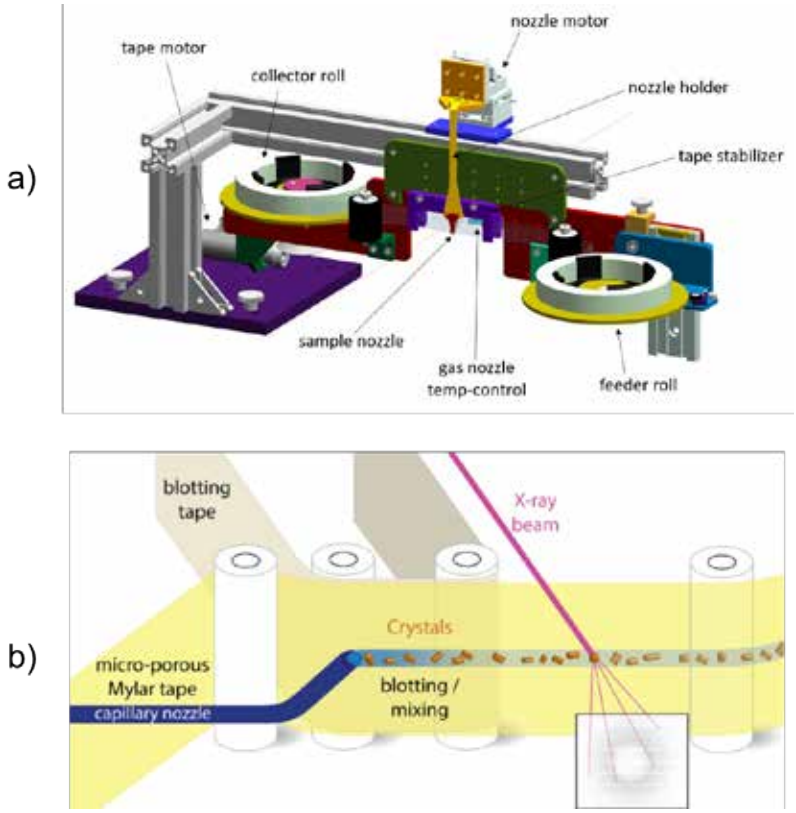

Figure 3.9: a) CFEL tape-drive [83], b) Suna-Precision tape-drive (Reproduced with permission from the journals).

3.6 Time-resolved Serial Synchrotron Crystallography (TR-SSX)

TR-SSX is an innovative technique that combines the advantages of SSX structure determination with the study of protein dynamics. This method can be efficiently conducted at either synchrotrons or XFELs, depending on the specific time frame required to observe the chemical process of interest. One of the primary applications of TR-SSX is the investigation of conformational changes in proteins, wherein the switching between two

or more energetically favorable conformations is determined. Such conformational changes can be triggered, for instance, by pH alterations or light activation. In the context of time-resolved crystallography, data collection is carried out at room temperature to maintain the physiological relevance of the protein under investigation and since conformational changes are restricted at cryo-temperatures [85]. This involves using flow-based, fixed-target, or tape-drive systems, which enable a steady supply of fresh crystals during the experiment, ensuring reliable data collection and accurate results [86, 87]. This approach holds great promise for advancing our knowledge of biological processes and aiding drug development efforts.

3.6.1 Pump-probe experiment

In this thesis time-resolved crystallography is employed with the use of a photocage CO_2, so we utilized the pump-probe approach to gather data (Figure 3.10). In this technique, a laser pump with precise wavelengths is used to induce activation of a photocage or reactions in light-sensitive proteins, activating 10-40% of these proteins. The sample is initially illuminated and the laser pump initiates the photoreaction. After a defined time interval, an incident X-ray beam is directed onto the sample, either in the injector or at a fixed target [86].

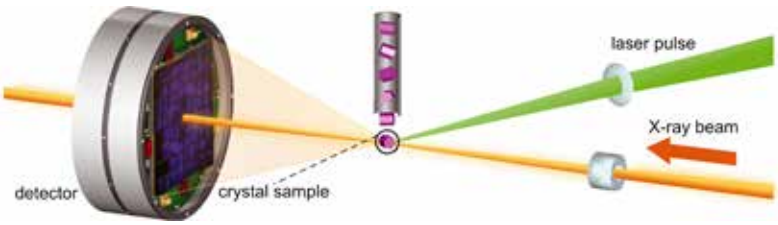

Figure 3.10: Schematic of pump-probe experiment (Reproduced with permission from reference [87]).

3.7 Data processing and refinement

Data processing and refinement of SSX data encompass a comprehensive series of steps. The first step is to find the locations of the obvious Bragg

peaks in the image. These are then used to index the pattern, which is followed by a series of refinement and result-checking steps. If the indexing solution is accepted, the unit-cell parameters and orientation, combined with the detector geometry, wavelength and other information about the X-ray beam, are used to calculate the positions of the Bragg peaks in the frame. Their intensities are then measured from the image data, employing a pixel intensity threshold to distinguish genuine diffraction from background noise [88]. Subsequently, integrated intensities undergo scaling and merging. During the scaling process, correction factors are introduced to ensure comparability among diffraction data, for example, accounting for crystal volume variations, disparities in X-ray absorption, X-ray radiation damage. As for the merging step, equivalent observations are aggregated to form a comprehensive dataset [89].

Following the scaling and merging steps, evaluating the dataset's quality involves calculating several figures of merit. These figures of merit encompass completeness, signal-to-noise ratio (I/σ), redundancy, Pearson correlation coefficient ($CC_{1/2}$), and R_{split}. Completeness represents the proportion of observed reflections within each resolution shell, ideally close to 100%, indicating a comprehensive dataset. The (I/σ) value indicates the strength of diffraction relative to the background, with a desired value of 1 for the highest-resolution shell. Redundancy quantifies the number of measured reflections, while $CC_{1/2}$ is derived from dividing the complete set of reflections randomly into two equal parts and calculating the correlation between the intensity estimates of these subsets (ranging between 0 and 1). Lastly, R_{split} evaluates the agreement between two halves of the dataset, providing valuable insights into the dataset's consistency and reliability (the ideal overall value should be below 20%). These figures of merit collectively contribute to assessing the dataset's overall quality [90].

The next step is phasing which will give us an electron density map. The basic electron-density map can be calculated numerically by a Fourier transformation of the set of observed (experimental) reflection amplitudes Fobs and their phases. However, because the phases, ρ_{calc}, cannot be measured at the same time as intensity (the phase problem [91]) we need to acquire them with a different method. Experimentally it is done with for example MAD (multi-wavelength anomalous diffraction) or SAD (single-wavelength anomalous diffraction), or mathematically using a reference

model with MR (molecular replacement) [92].

The final step involves refining the structure. This process is iterative, aiming to create an accurate electron density model by adding residues and shaping the model to fit the electron density, ultimately improving the model's phases. The model building is commonly carried out in Coot [52], followed by Refmac5 [93] cycles. Upon completion of a refinement run in Refmac5, the quality of the job is assessed using the R-factors R_{work} and R_{Free}. These factors measure the discrepancy between experimentally observed and calculated structure factor amplitudes (F_{obs} and F_{calc}). An accurate refinement results in a consistent decrease in the R-factors, indicating that the structure has been correctly built into the electron density. Conversely, the incorrect model building would lead to increased R-factors or an increased gap between R_{work} and R_{Free}.

All processing and refinement in this thesis was done using the following: Diffraction data was indexed, integrated, merged and converted to MTZ format using CrystFEL 0.10.1 [88, 94]. Peak detection was done using "peakfinder8" [95], indexing was done with indexing algorithms MOSFLM [96], XDS [97] and XGandalf [98], and finally merging was done using partialator. Data truncation, phasing (Phaser [99]) and structure refinement was performed in CCP4 Cloud [100, 101]. The structures were refined by one round of rigid body refinement using REFMAC5 [93, 102], followed by several rounds of restrained refinement. Model building was done in Coot [52, 103] and all structural representation was made in PyMOL [104].

Chapter 4

Development of fixed-target SSX

In this chapter I will present work connected to fixed-target SSX, including results from **Paper I** and **Paper III**.

4.1 Anaerobic fixed-target serial crystallography using sandwiched SiN membranes (Paper I)

In **Paper I**, we describe a method for anaerobic SSX at room temperature with silicon-nitride membranes that can easily be implemented on BioMAX and any other beamline with access to a glovebox. We have developed a fixed-target method that "sandwiches" oxygen-sensitive crystals between silicon-nitride (SiN) chips [30, 75], protecting them from ambient oxygen. Using crystals of DeoxyHb, we demonstrate the practicality of this design for anaerobic SSX and further verify by UV-Vis and X-ray spectroscopy that the hemoglobin crystals remain in the deoxy state.

4.1.1 Crystallization

Equine hemoglobin (Sigma, CAS-9047090) stock solution of 20-25 mg/ml was prepared in 10 mM HEPES, pH 7.5 and crystalized using the stirred batch method [38] by mixing into precipitant solution (26 %v PEG3350, 10 mM HEPES pH 7.5). At 20°C 500 µL of precipitant was added to 250 µL protein solution. The mixture was stirred in small HPLC vials with

rice corn-sized stir bars on a magnetic stirrer for about 20h, after which crystals of 5x5x5 μm^3 size were obtained.

4.1.2 3D printed holder and accessories

Since handling this type of chips is challenging due to being small and thin, we have designed an assembling tool, a chip tray and an MX-sample holder for easier manipulation. The MX-sample holder was printed with Tough 1500 Resin (Formlabs Inc, USA), for the rest of the 3D-printed components Tough Resin V5 (Formlabs Inc, USA) was used. The assembling tool went through a few iterations, as can be seen in Figure 4.1. The final iteration accounts for imperfections in chip size (some sides being longer, or with "horns" in the edges), avoids too high pressure with the lever that would destroy the chips and leaves one corner easily accessible for handling upon assembly (Figure 4.2a). Several chips can be prepared for quicker assembly with the chip tray (Figure 4.2b). To ease the sample mount to the goniometer head at MX beamlines, the MX-sample holder was designed to be attached to SPINE bases easily [105] (Figure 4.2c). The tightening screws allow for extra pressure to be applied on the sides of the sandwiched chips during data collection, further ensuring air-tightness.

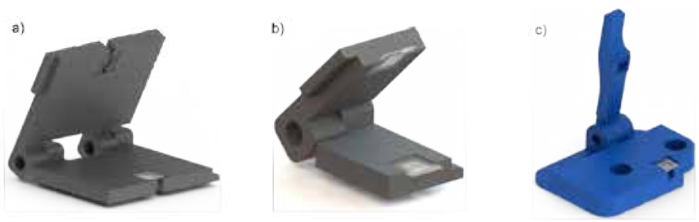

Figure 4.1: Development of assembling tool, a) first iteration, b) third iteration, c) final iteration.

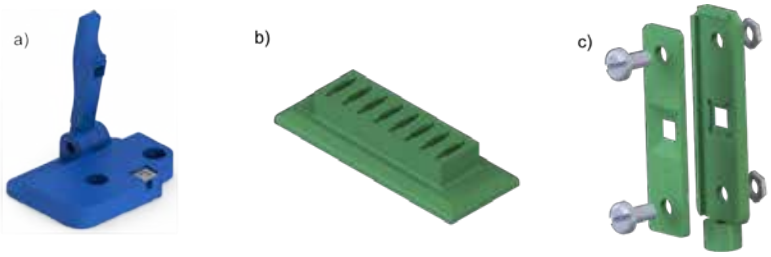

Figure 4.2: 3D-printed accessories for SiN chip handling. a) Assembling tool; b) SiN chip tray; c) MX-sample holder.

4.1.3 Anaerobic chip assembly for X-ray crystallography

Before data collection, DeoxyHb crystals were prepared fresh inside a nitrogen-filled glovebox (Coy Laboratory Products, Inc.). The average oxygen concentration in the glove box was 2 ppm during sample preparation and never exceeded 10 ppm. The aerobically grown hemoglobin microcrystals were transferred into the glovebox and chemically reduced by mixing sodium dithionite solution [106] (50 mM sodium dithionate, 26 % w/v PEG3350, 10 mM HEPES pH 7.5) with hemoglobin microcrystals (5 µL : 20 µL respectively) and incubated within the glovebox at room temperature for 2 h, during which the crystal slurry undergoes a color change from brown to pink. Inside the glovebox, SiN chips (membrane size 2.5 x 2.5 mm^2, membrane thickness 1000 nm, frame size 5.0 x 5.0 mm^2, frame thickness 200 µm, from Silson Ltd, UK) were loaded onto the assembling tool (Figure 4.3a-b), followed by the addition of 2 µL of microcrystal slurry (Figure 4.3c). To seal the chip, a small amount of superglue (Super Glue Brush On Loctite) was applied onto all four corners of the chip with a single hair from a small paintbrush (Figure 4.3d). Then a second chip was placed on the top (Figure 4.3e) and pressed gently with the lever to secure it (Figure 4.3f). The assembled chip was then put in the MX-sample holder (Figure 4.2c) for data collection.

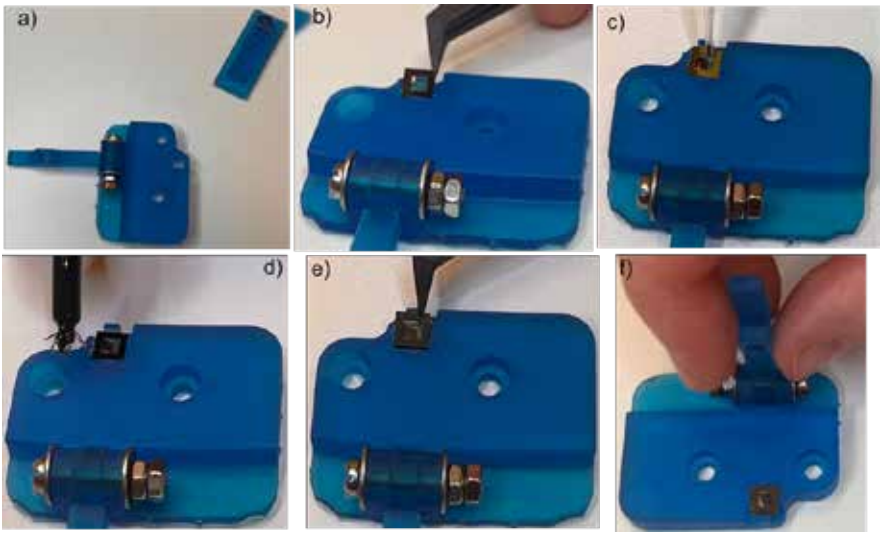

Figure 4.3: Procedure for anaerobic chip assembly.

4.1.4 Results

The first thing we needed to do was to verify that the chips assembled with this method maintained deoxy form to be viable for MX collection. To achieve this, we conducted two beamtime experiments at Balder [107]. The first experiment aimed to determine if we could detect the signal from a mere 2 µL sample, as the typical samples at Balder are usually larger and more concentrated. However, a significant issue arose: after a single data collection, the crystals on the chip got reduced or were destroyed. Additionally, we encountered problems when attempting to use the beamline's regular sample holder. Consequently, we designed a specialized holder tailored explicitly for the Balder beamline (Figure 4.4b). This innovative holder enabled us to prepare six chips simultaneously. As a result, we could execute a well-structured collection strategy, gathering data from one chip every 20 minutes. This strategic approach effectively resolved the issue of reduced or destroyed crystals encountered after the initial collection.

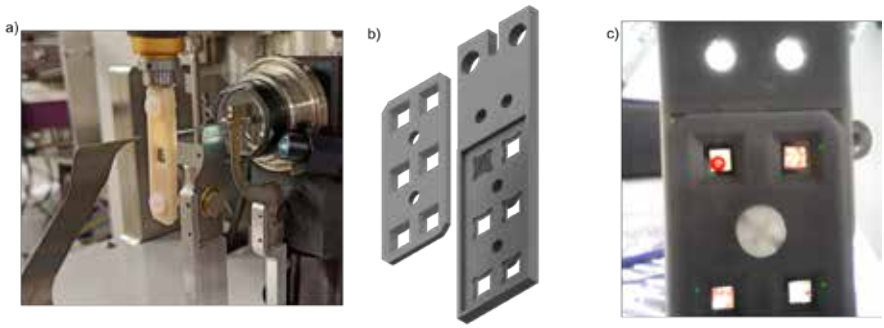

Figure 4.4: a) MX-sample holder at BioMAX beamline, b) Balder holder, c) Balder holder at the Balder beamline with the red circle marking the beam position on chip 1 seen through the sample camera and Orthoviewer software.

Results from the second beamtime revealed that the chip could hold for approximately 40 minutes, with the arrangement of the chips playing a significant role. This is evident from the observation that only chips 3 and 4 retained their deoxy state, as illustrated in Figure 4.5. This observation highlighted the importance of reinforcing the chip holder's integrity with additional pressure, such as incorporating screws. This realization subsequently influenced the design of the MX-sample holder with this consideration in mind, as depicted in Figure 4.2c. In order to validate the functionality of the newly devised holder, a supplementary assessment was conducted using an offline UV-Vis spectroscopy setup. As presented in Figure 4.6, the data confirmed the holder's capacity to maintain the desired conditions for a minimum duration of 30 minutes.

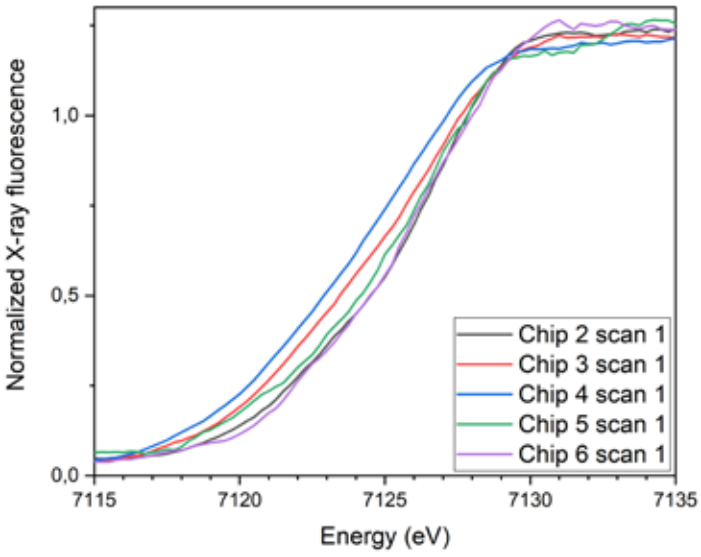

Figure 4.5: The first Fe K-edge XANES scan of the chip-sandwich in position 2-6 of the sample holder in Figure 4.4b, numbered from the top left corner. Top row chip 2 (black), middle row chip 3 (red) and 4 (blue), last row chip 5 (green) and 6 (purple).

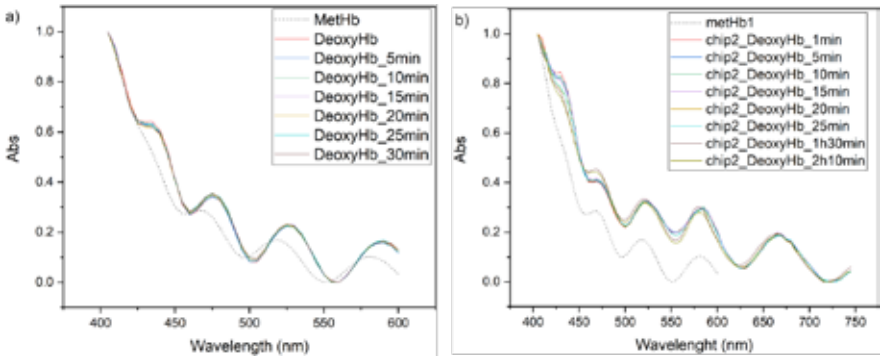

Figure 4.6: UV-Vis spectra of a chip-sandwich chip1 (a) and chip2 (b) with DeoxyHb in the MX-sample holder (the spectra have been normalized in Origin 2018b).

During MX data collection, each DeoxyHb chip was prepared fresh before collection. In total five chips were collected (Figure 4.4a) to verify the consistency of the method. The prepared chip-sandwiches were rastered through the X-ray beam in a regular snake-like pattern. Diffraction data were collected at room temperature with an X-ray beam size of 20 x 5 μm^2 (FWHM), through a 10 µm diameter aperture, at a photon energy of 12.6 keV and flux of 2 x 10^{12} photons/s. 10,000 to 20,000 images per chip were collected from five chips each for both MetHb and DeoxyHb. All five chips with DeoxyHb were also independently processed, exhibiting the presence of the deoxy state, except chip 3, which contained a bubble following the preparation resulting in too few indexed images for a separate analysis.

The α-subunits of DeoxyHb have a water molecule in the heme pocket about 3 Å (3.1 Å in this case) from the iron and hydrogen-bonded to the distal histidine (Figure 4.7). In MetHb the α- and β-heme groups have a water molecule as the 6th ligand, approximately 2 Å (2.2 Å in this case) from the iron (Figure 4.8). When hemoglobin changes from deoxy form to oxy or met form there is no significant change in the inner region of α1β1/α2β2 dimer. Visible changes are present in the outer region of the dimer and in the dimer interface area. Interaction between α1β2 and α2β1 moves towards the centre of the molecule. Residues in contact in αβinterfaces are between αB (Glu30/A – Phe36/A) and βH (Phe122/B – Lys132/B), αG (Ser102/A – Leu113/A) and βG (Gly107/B – Phe118/B), αH (Phe117/A – Lys127/A) and βB (Arg30/B – Pro36/B). The most noticeable movement is at the β-heme where a water molecule is bound in MetHb compared to the empty β-heme in DeoxyHb. The β-heme of MetHb moves downwards to the proximal side of the heme pocket (Figure 4.9). Both structures are in agreement with published structures [108–110].

The assembling tool for chip-sandwich preparation simplifies the process, facilitates visualization, and decreases the risk of crystal or chip damage. Furthermore, SiN chips do not cause strong diffraction that can damage detectors, but are single-use only. With the MX-sample holder and the protocol presented, it is feasible to collect data from oxygen-sensitive samples and the method can be implemented at many MX beamlines that have access to a glovebox and an MX-compatible goniometer.

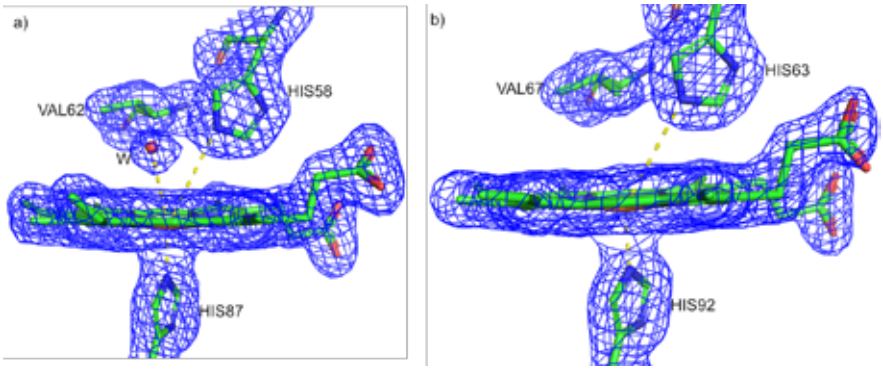

Figure 4.7: View of the final $2mF_o–DF_c$ electron density map for the heme pockets of DeoxyHb, (a) the α subunit and (b) the β subunit. Density is contoured at 1.1σ. The distance between HIS58/63 and the heme iron is 4.2 Å, while the distance between the water molecule and the heme iron is 3.1 Å

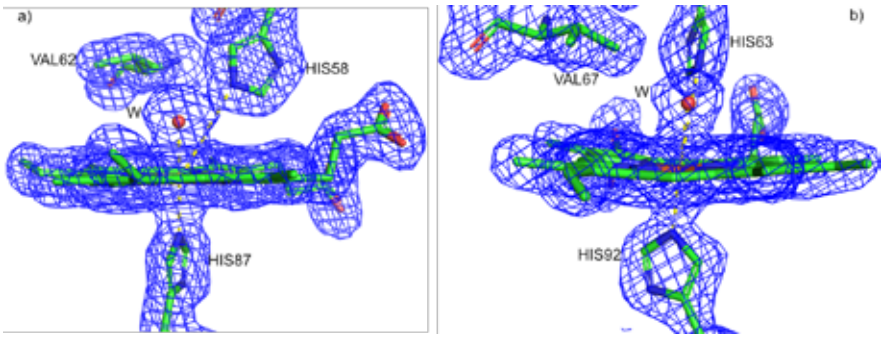

Figure 4.8: View of the final $2mF_o–DF_c$ electron density map for the heme pockets of MetHb, (a) the α subunit and (b) the β subunit. Density is contoured at 1.1σ. The distance between HIS58/63 and the heme iron is 4.1 Å, while the distance between the water molecule and the heme iron is 2.1 Å

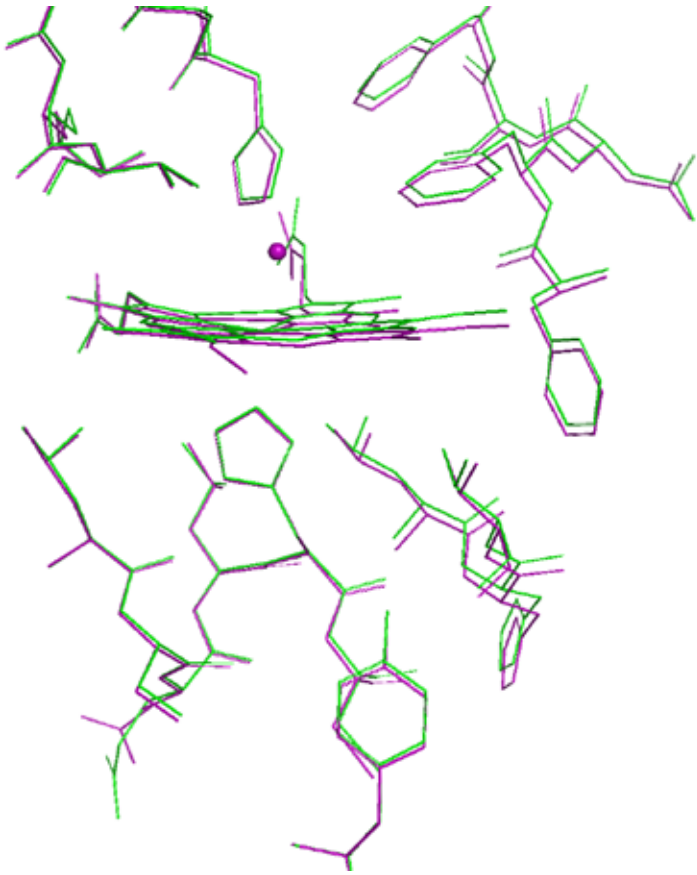

Figure 4.9: Comparison of the β-heme pocket of DeoxyHb (green) and MetHb (purple) in F-helix frame

4.2 *In-situ* data collection at BioMAX

Incorporating crystallization plates into the data collection process offers several benefits. It eliminates the need for sample manipulation, such as using cryoprotectant agents or manually retrieving crystals with a cryo-loop. Additionally, this approach is valuable for crystal screening during crystallization optimization and fragment screening. Nevertheless, certain constraints come into play, encompassing narrower oscillation angles within

the diffraction system, heightened background interference due to the presence of scatterers like crystallization plates, seals, and solvents, as well as reduced dosage thresholds at ambient temperature. Nonetheless, adopting the small-wedge or SSX technique can mitigate these challenges and facilitate the acquisition of comprehensive datasets.

4.2.1 BioMAX implementation

The first step involves replacing the MiniKappa Head with a Plate Holder Head in MD3 goniometer setup (Figure 4.10 a). Subsequently, a software modification is carried out in both MD3 and MXCuBE, enabling a dedicated plate scanning mode (developed specifically for this experiment). As part of the optimization process, the cryo-nozzle is removed from the sample position and the flow of cold nitrogen gas is reduced (to minimize the interference and reduce the use of liquid nitrogen). The standard beamline setup has a penta-aperature (Figure 4.10 red rectangle), beam capillary (Figure 4.10c blue rectangle) and beamstop (Figure 4.10 green rectangle). For plate experiments to prevent any collision during data collection (as can be seen in Figure 4.10b the plate fully rotated would come in collision with the standard beam capillary), the conventional beam capillary is substituted with a streamlined solution - a cannon aperture capillary (Figure 4.10d), effectively integrating capillary and aperture functionalities into one unit.

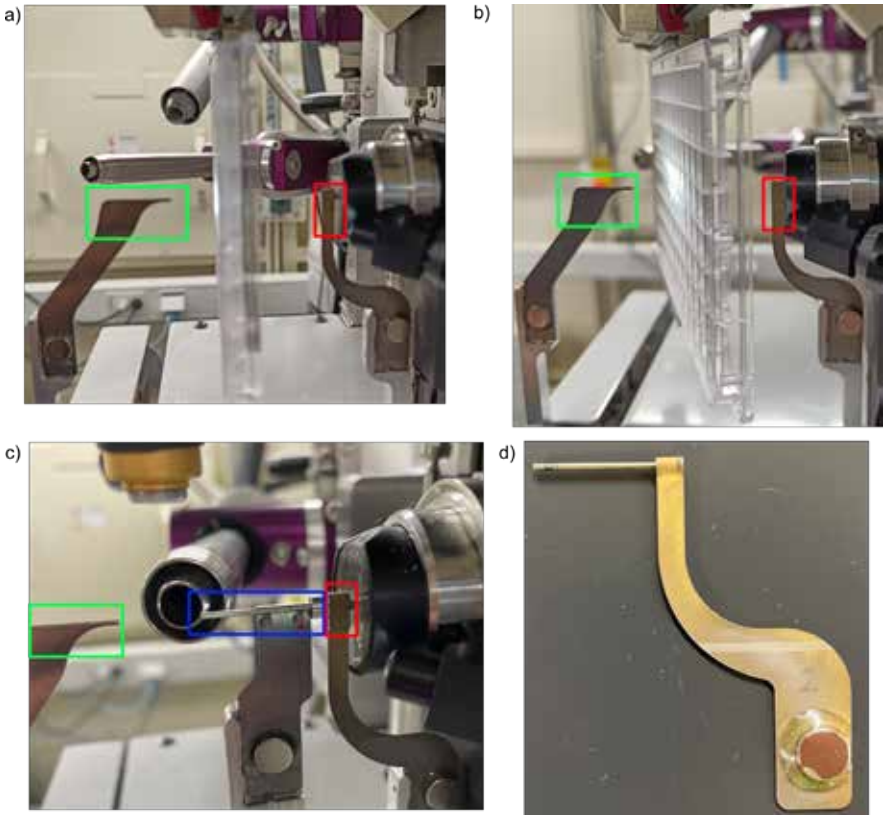

Figure 4.10: Plate setup on BioMAX. a) starting position of the plate at the goniometer, b) plate in full rotation at the goniometer, c) standard rotation setup, d) cannon aperture capillary

4.2.2 Results

Data were collected from lysozyme and hemoglobin crystals, crystalized as mentioned in 2.4 and 2.5, respectively. During the beamtime we evaluated the performance of two distinct plates: CrystalDirect and In Situ-1 (both from MiTeGen). Data were collected with a mesh grid drawn on each drop, which was then rastered through the X-ray beam in a regular snake-like pattern. Regrettably, due to a delay in the delivery of the canon aperture,

our data collection during that beamtime was constrained to employing the beamline aperture exclusively, without the capillary. Consequently, we could not benefit from a focused beam and 100 % transmission, leading to a more noticeable background signal. Despite these limitations, our efforts still yielded valuable results, although the crystals' diffraction capabilities were not fully realized. This data, however, demonstrated the viability of using this method at BioMAX. Results can be seen in Table 4.1 and Figure 4.11. Furthermore, we have done a successful first dark experiment with plates in collaboration with the Westenhoff group at Uppsala University.

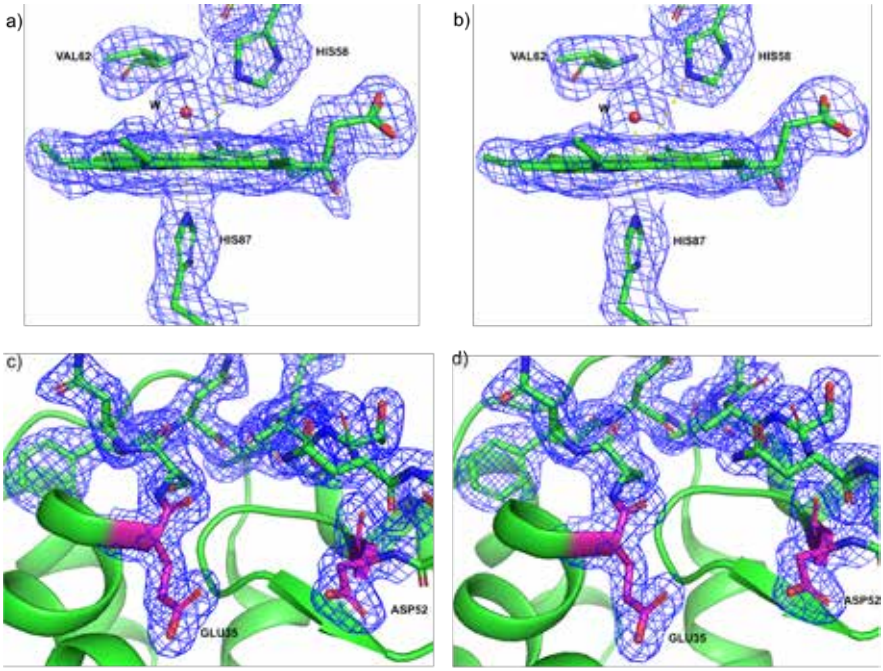

Figure 4.11: View of the final $2mF_o–DF_c$ electron density map: a) Heme pocket in α subunit from CrystalDirect, b) Heme pocket in α subunit from In-Situ1, c) Lysozyme active site from CrystalDirect, d) Lysozyme active site from In-Situ1. Density is contoured at 1.1σ.

Table 4.1: In-Situ results

	Hb_CrystalDirect	Hb_In-Situ1	Lyz_CrystalDirect	Lyz_In-situ1
Diffraction source	BioMAX, MAX IV Laboratory	BioMAX, MAX IV Laboratory	BioMAX, MAX IV Laboratory	BioMAX, MAX IV Laboratory
Wavelength (Å)	0.9763	0.9763	0.9763	0.9763
Temperature (K)	294	294	294	294
Space group	C121	C121	$P4_32_12$	$P4_32_12$
a, b, c (Å)	108.56, 62.74, 54.28	108.56, 62.74, 54.28	78.75, 78.75, 38.01	78.75, 78.75, 38.01
α, β, γ (°)	90, 111, 90	90, 111, 90	90	90
Resolution (Å)‡	53.35 – 2.3 (2.38 – 2.3)	53.35 – 2.35 (2.43 – 2.35)	55.69 – 2.1 (2.17 – 2.1)	55.66 – 2.1 (2.18 – 2.1)
R_{split} (%)†‡	12. 15 (43)	9.61 (33.24)	5.82 (12.78)	6.7 (13.66)
I/σ (I)‡	9.7 (3.64)	11.99 (3.97)	15.21 (7.32)	12.97 (6.71)
$CC_{1/2}$‡	0.9734 (0.6025)	0.9833 (0.8433)	0.9938 (0.9749)	0.9935 (0.9697)
Completeness (%)‡	100 (100)	100 (100)	100 (100)	100 (100)
Multiplicity‡	130 (83)	197 (129)	118 (80)	89 (59)
Collected images	137607	198725	74485	84607
Indexed patterns	32468	44597	11470	8440
Indexing rate (%)	23.6	22.4	15.4	10
Number of reflections	1993454	2833978	877648	660614
Number of unique reflections	15265	14332	7410	7420
Refinement				
Resolution range (Å)	53.35 – 2.3	53.35 – 2.35	55.69 – 2.1	55.66 – 2.1
R_{work}/R_{free} (%)	14.17/19.68	15.27/20.44	14.6/18.82	14.15/17.92
Number of atoms	4552	4522	2016	2017
Average B factor (Å^2)	54	64	46	46
RMSD bonds (Å)	0.017	0.014	0.015	0.014
RMSD angles (°)	2.27	2.15	2.13	2.02

†$R_{split} = \left(\frac{1}{\sqrt{2}}\right) \frac{\sum_{hkl} |I_{even} - I_{odd}|}{0.5 \sum_{hkl} (I_{even} - I_{odd})}$

‡Values in parenthesis correspond to those of the highest-resolution shell.

4.3 Roadrunner II at BioMAX

Dr. Alke Meents' research team has developed a steadfast sample holder tailored for fixed-target applications in serial crystallography. This inventive design was initially employed in experiments conducted at synchrotron sources, demonstrating its effectiveness in both cryogenic [111] temperature and room temperature [112] data acquisition settings. The group's ingenuity extended to the development of the precision-driven Roadrunner goniometer and Roadrunner chips which were introduced in chapter 3.5.2.2 and Figure 3.8c. This advanced instrument revolutionized fixed-target serial crystallography by capitalizing on the complete 120 Hz repetition rate offered by the LCLS XFEL situated at Stanford, USA [113] (Figure 4.12). Subsequently, the Roadrunner goniometer's capabilities were expanded to include time-resolved laser pump-probe experiments. Aligned with these advances, a collaborative initiative was initiated under the RÅC grant 2017-06734, with the one of the objective of establishing and integrating Roadrunner II at the MAX IV facility. The reason for bringing Roadrunner to BioMAX was to have an established

and reproducible method for fixed-target at BioMAX, and prepare the groundwork for its later implementation at MicroMAX with time-resolved experiments in mind. Although the original timeline earmarked for this undertaking was slated for commencement in 2018, the timeline was deferred to 2020. Unfortunately, the outbreak of the Covid-19 pandemic in 2020 introduced unprecedented disruptions, leading to a further postponement of the project's fruition until April 2023.

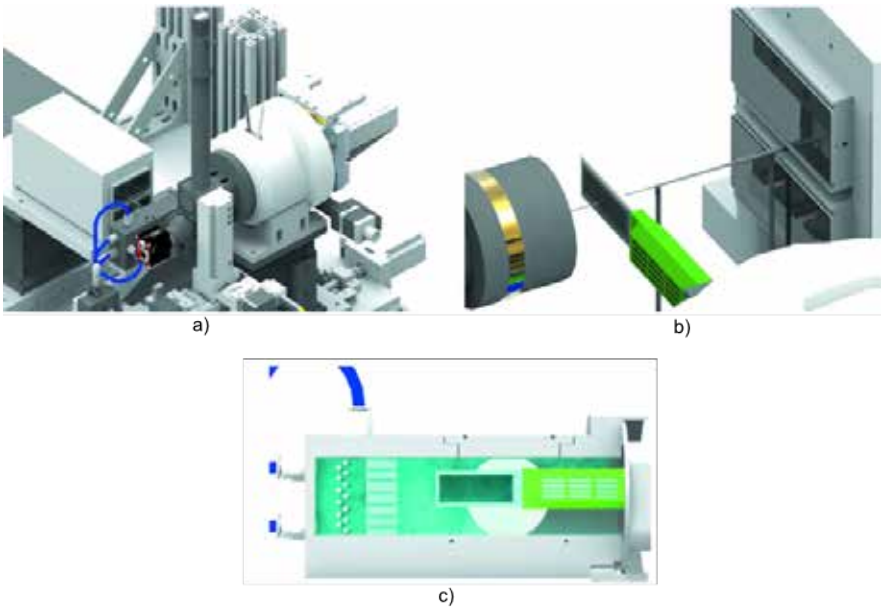

Figure 4.12: Technical drawing of the Roadrunner II goniometer. a) Roadrunner position at end-station ID09 at the ESRF; b) close up of the chip in front of the beam; c) chip inside humidity chamber (Reproduced with permission from the [78])

4.3.1 BioMAX implementation

The project involved a comprehensive implementation across both hardware and software aspects. On the hardware front, a specialized stand was designed to securely position Roadrunner on the granite surface at

BioMAX, as its size prevented it from fitting onto the Arinax stage. This adaptation process is illustrated in Figure 4.13. Conversely, the software aspect saw significant contributions from our German collaborators [114].

Figure 4.13: Roadrunner II at BioMAX; a) control computer and humidifier, b) back view after installation, c) side view, d) sample position before humidity chamber, e) sample position with humidity chamber

4.3.2 Samples

We used lysozyme crystals for proof of concept (crystalized as mentioned in 2.4). The next sample was Soluble Epoxide Hydrolase (SHE) which was previously collected at BioMAX with Silson SiN and Serial-X fixed-target chips, so we wanted to compare the results. Lastly, we tested an LCP sample using C*c*O crystals to compare it with other fixed-target chips

available at BioMAX. CcO and sHE crystals were donated by University of Gothenburg.

4.3.3 Results

During the beamtime, a series of tests were conducted, encompassing various parameters such as exposure time, rotation, and diverse collection patterns. While encountering challenges with larger-sized chips and some motor malfunctions during the process, overall, the beamtime proved successful. Notably, the diffraction outcomes from sHE crystals exhibited heightened clarity and reduced background compared to previous collections. Regrettably, a setback occurred when one of the chips dried out during motor repairs, leading to insufficient samples for higher-resolution data sets. CcO also displayed improved diffraction with less background compared to prior methods. However, due to silicon diffraction constraints, data collection required a lower transmission setting, consequently affecting the attainable highest resolution. Likewise, Lysozyme demonstrated commendable diffraction, albeit slightly below the peak achieved with these crystals at BioMAX. This outcome was again influenced by the need for lower transmission due to silicon diffraction. The summarized findings are presented in Table 4.2 and illustrated in Figure 4.14. In conclusion, these results signify a successful initial test and integration at BioMAX. While some refinements are necessary, primarily in the control components, this has also facilitated planning for the future integration at MicroMAX.

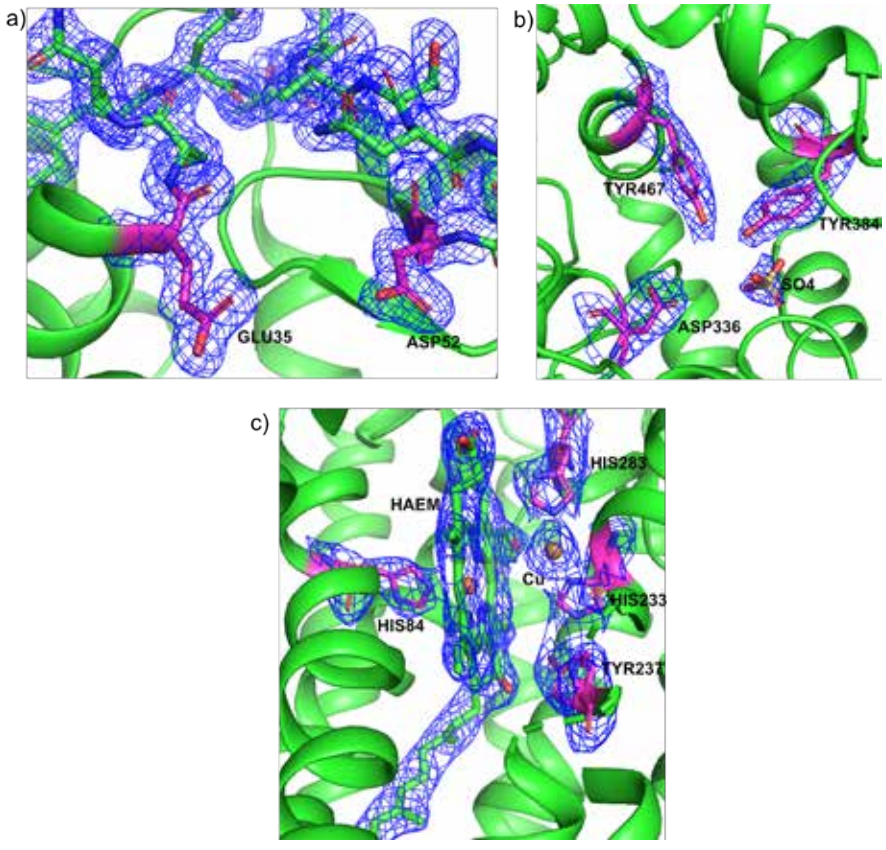

Figure 4.14: View of the final $2mF_o–DF_c$ electron density map: a) Lysozyme active site, b) sHE active site, c) CcO haem a_3 active site. Density is contoured at 1.1σ.

Table 4.2: Roadrunner results

	Cytochrome *c* oxidase	Soluble Epoxide Hydrolase	Lysozyme
Diffraction source	BioMAX, MAX IV Laboratory	BioMAX, MAX IV Laboratory	BioMAX, MAX IV Laboratory
Wavelength (Å)	0.9763	0.9763	0.9763
Temperature (K)	294	294	294
Space group	C121	$P6_522$	$P4_32_12$
a, b, c (Å)	146.06, 100.17, 96.62	94.23, 94.23, 247.06	78.72, 78.72, 38.07
α, β, γ (°)	90, 126.76, 90	90, 90, 120	90
Resolution (Å)‡	22.79 – 2.7 (2.8 – 2.7)	81.61 – 2.7 (2.8 – 2.7)	55.66 – 1.8 (1.86 – 1.8)
R_{split} (%)†‡	17.67 (41.17)	15.93 (36.97)	6.61 (17.15)
I/σ (I)‡	6.36 (2.55)	7.76 (2.94)	14.32 (5.51)
$CC_{1/2}$‡	0.9457 (0.7648)	0.9366 (0.8237)	0.9918 (0.9388)
Completeness (%)‡	100 (100)	99.8 (99.5)	100 (100)
Multiplicity‡	37 (25)	29 (20)	112 (78)
Collected images	40914	20754	29040
Indexed patterns	15961	3943	10944
Indexing rate (%)	39.01	19	37.7
Number of reflections	1128782	536696	1299361
Number of unique reflections	30700	18737	11610
Refinement			
Resolution range (Å)	22.79 – 2.7	81.61 – 2.7	55.66 – 1.8
R_{work}/R_{free} (%)	13.38/18.86	14.85/22.13	14.48/17.30
Number of atoms	12884	8746	2032
Average B factor (Å^2)	56	46	38
RMSD bonds (Å)	0.015	0.013	0.014
RMSD angles (°)	2.35	2.26	1.84

†$R_{split} = \left(\frac{1}{\sqrt{2}}\right) \frac{\sum_{hkl}|I_{even}-I_{odd}|}{0.5\sum_{hkl}(I_{even}-I_{odd})}$

‡Values in parenthesis correspond to those of the highest-resolution shell.

4.4 Room temperature serial crystallography structure of human cytochrome P450 3A4 (Paper III)

The cytochrome P450 enzyme family plays a crucial role in the body's metabolism of foreign substances, such as pharmaceutical compounds. Hence, it is imperative to consider their significance in drug development. Among these enzymes, CYP3A4 is the primary human isoform. This protein is highly adaptable, capable of interacting with a wide range of substances, and susceptible to inhibition by compounds of varying sizes. As CYP3A4 accommodates different ligands, it undergoes substantial conformational changes, transitioning the active-site binding pocket from a collapsed state to various open configurations [14, 15, 115]. Despite the wealth of structural data available, our comprehension of the dynamic characteristics of CYP3A4 remains limited. In this study, we present the

structural analysis of CYP3A4 at room temperature, employing serial crystallography as our methodology. The room-temperature structure closely resembles the cryo-structures of the unbound enzyme, including the configuration of the active-site lid. Notably, at room temperature, we observe improved definition of certain loops, even though this structure exhibits lower resolution. Samples on Silson SiN chips were prepared using 3D-printed tools presented in Chapter 4.1.

4.4.1 Data collection and processing

Microcrystals of CYP3A4 were tested for diffraction using a variety of fixed-target devices (Oxford chip [77], custom self-assembled mylar chips at the PXI – X06SA beamline, silicon-nitride (SiN) chip [30] and Serial-X chips) at four different synchrotron beamlines of Diamond Light Source, Swiss Light Source, Petra III and MAX IV Laboratory, respectively. The highest-quality SX data were collected using the Serial-X chip at the BioMAX beamline of MAX IV Laboratory. Each chip was loaded with 0.8 – 1 µL of densely concentrated crystals. Room-temperature diffraction data were recorded on an Eiger 16M hybrid-pixel detector (DECTRIS) by raster grid scanning using a beam size of 20 x 5 μm^2 (FWHM, horizontal x vertical), an X-ray energy of 12.7 keV, 2.3 x 10^{12} photons/s flux with 100 % transmission, and 11 ms exposure time. Seven chips were collected, averaging 24,163 images per chip. Data was processed as described in 3.7. Data processing and refinement statistics are presented in Table 4.3.

Table 4.3: CYP3A4 results

	CYP3A4
Diffraction source	BioMAX, MAX IV Laboratory
Wavelength (Å)	0.9763
Temperature (K)	294
Space group	I222
a, b, c (Å)	79.95, 103.74, 128.64
α, β, γ (°)	90
Resolution (Å)‡	80.75 – 2.95 (3.00 – 2.95)
R_{split} (%)†‡	5.43 (73.04)
I/σ (I)‡	14.8 (1.00)
$CC_{1/2}$‡	0.995 (0.55)
Completeness (%)‡	100 (100)
Multiplicity	423
Collected images	169142
Indexed patterns	66748
Indexing rate (%)	39.5
Number of reflections	4637438
Number of unique reflections	11603
Refinement	
Resolution range (Å)	80.75 – 2.95
R_{work}/R_{free} (%)	24.4/29.5
Number of atoms	3782
Average B factor (Å^2)	97
RMSD bonds (Å)	0.002
RMSD angles (°)	1.21

†$R_{split} = \left(\frac{1}{\sqrt{2}}\right) \frac{\sum_{hkl} |I_{even} - I_{odd}|}{0.5 \sum_{hkl} (I_{even} - I_{odd})}$

‡Values in parenthesis correspond to those of the highest-resolution shell.

Chapter 5

Development of flow-cells

In this chapter I will present work connected to flow-based SSX, including results from **Paper II**.

5.1 A simple goniometer compatible flow-cell for serial synchrotron X-ray crystallography (Paper II)

The idea was to design an LCP-based flow delivery method that is easier to use and control than HVE at BioMAX, which became even more needed when Covid-19 pandemic started and users were not allowed to come to MAX IV.

5.1.1 Design of a 3D-printed plug for flow cell assembly

We designed a lightweight base for the flow cell utilizing AutoCAD (Autodesk 2020) software to accommodate the spatial constraints of a standard goniometer sample mounting system. Our process involved printing prototypes on a 3D printer (MAX/MAX UV, Asiga technologies) using plastic resin (Asiga PlasGRAY V2). This design underwent iterative improvements. After printing, each base underwent an isopropanol wash, and internal channels were purged using isopropanol-filled syringes to eliminate any residual resin. Following this, the system was air-dried and underwent two stages of UV light hardening (2 x 2000 flashes). Each 3D-printed component featured a base capable of grasping a magnetic disc (5 x 5 mm, Supermagnet, Neodymium N45, S-05-05-N), or a similarly sized iron

disc. This innovation facilitated mounting the system onto a goniometer magnet and aligning it with the X-ray beam via beamline alignment tools. The assembly process of the flow cell device involved embedding fused silica capillary tubing (TSP250350, CM Scientific Polymicro Technologies) through a designated opening within the 3D-printed base, secured with super glue. The tubing typically possessed an outer diameter of 360 $\pm$ 10 µm and an inner diameter of 250 $\pm$ 6 µm, and it was trimmed to a length enabling it to span from the syringe pump to the magnetic mount. Finalizing the assembly entailed affixing a slender, X-ray transparent borosilicate glass capillary (Hampton Research Glass Number 50 Capillary) to the opposite end of the 3D-printed device in relation to the magnet. Within this study, we assessed glass capillaries of both 100 and 200 µm diameters; however, alternative operational diameters can be chosen based on requirements. These glass capillaries typically maintained a wall thickness of approximately 10 µm and were usually cut around 50 to 55 mm away from the magnetic cap. The fully assembled flow cell weighed less than 3 g and the convenience of preassembled flow cells, supported by 3D-printed structures, facilitated their transportation to the synchrotron radiation facility.

5.1.2 Sample preparation

Microcrystals of ba_3-type C*c*O from *T. thermophilus* was used. The protein was produced, purified and crystallized via methods described previously [116] using a well-founded technique for large-scale production of ba_3-type CcO microcrystals [35]. Purified protein was concentrated to 12 to 15 mg/mL in 20 mM Tris–HCl pH 7.6, 0.05 %(w/v) DDM, 80 mM NaCl. For the lipidic cubic phase (LCP) crystallization, concentrated protein was mixed with monoolein (Nu-Check Prep; CAS 111-03-5) at a ratio of 2:3 protein to lipid (40 µL of protein and 60 µL of monoolein) using an LCP coupler connected to two gas-tight 100 µL Hamilton syringes [117]. Strings of LCP reconstituted protein (10 to 15 µL) were then dispensed into a nine-well glass plate containing 300 µL of 1.4 M NaCl, 100 mM MES pH 5.3 with 36 to 39 %(v/v) PEG 400. The plate was covered with a transparent seal (Molecular Dimensions, ClearVue TM Sheets, MD6-O1S, Lot No: 11024) and microcrystals of around 20 µm in their longest

dimension were obtained at room temperature within 2 to 3 days of incubation in the precipitant solution. LCP crystals of ba_3-type C*c*O were transported in 500 µL Hamilton syringes to the MAX IV Laboratory for SSX data collection. The LCP phase was softened by the addition of 5 to 10 µL of PEG 400 into the syringe immediately prior to sample injection.

5.1.3 Data collection

Proof-of-principle experiments were conducted at the MAX IV Laboratory at the BioMAX beamline [21]. The preassembled flow cell was mounted on the goniometer magnet and aligned with the X-ray beam using the in-line visualization tools of the beamline (Figure 5.1a,b). Next step was loading of 100 µL Hamilton syringe with LCP crystals of ba_3-type C*c*O on a CETONI Nemesys syringe pump. Sample viewing, alignment and measurement were done using the beamline control software MXCuBE3 [118]. Data collection was triggered manually when sample was observed to flow through the glass capillary (Figure 5.1b). After exposure to the X-ray beam, samples were collected in a catcher (Figure 5.1c). X-ray diffraction data were collected at room temperature using X-ray beam size of 20 x 5 μm^2 (FWHM), a photon energy of 12.6 keV and a flux of 3.6 x 10^{12} photons/s. LCP crystals of ba_3-type C*c*O were injected vertically downwards at flow-rates of 5 nL/s for the 100 µm-diameter glass capillary and 20 nL/s for the 200 µm-diameter glass capillary. In both cases this equates to a downward velocity approximately equal to 0.64 mm/s, and it therefore took approximately 8 ms for the sample to move through the X-ray beam. X-ray diffraction data were recorded on an EIGER 16M hybrid pixel detector with an exposure time of 50 ms. However, exposure to the X-ray beam triggered gradual charring of the glass capillary over time, leading to slight protein accumulation along the capillary's inner walls. To manage this concern the capillary was shifted about 100 µm vertically as required during data collection.

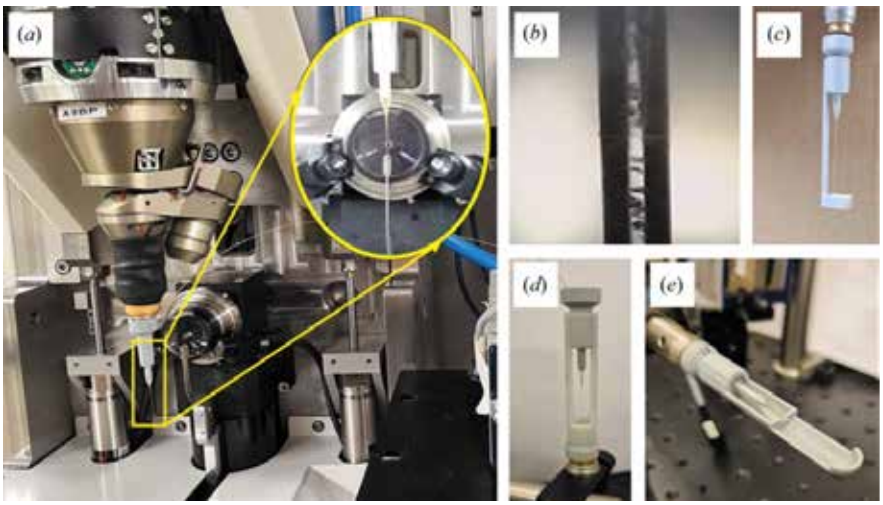

Figure 5.1: Mounting and alignment of the 3D-printed flow cell on a macromolecular crystallography beamline. (a) Flow cell mounted on the goniometer magnet and aligned with the X-ray beam at BioMAX. (b) LCP crystals of ba3-type CcO injected into the flow cell were observed through the glass capillary using the standard alignment optics of BioMAX. (c) Design of the catcher when the goniometer allows vertical mounting from above. This catcher is mounted by sliding over the flow cell and is held in place by friction. (d) Design of the catcher when the goniometer allows vertical mounting from below. In this case the sample also flows downwards. (e) Design of the catcher when the goniometer allows horizontal mounting.

5.1.4 Results

In this work we developed a practical and lightweight flow cell design that leverages the existing alignment tools present in macromolecular crystallography beamlines around the world. This design also conforms to the magnetic-mount standards commonly used in cryo-crystallography. By designing the system to fit into established standards, we ensure that the flow cell can be easily and quickly installed and aligned without causing disruptions to the typical setup of a macromolecular crystallography

beamline. Our system's flexibility allows it to be adjusted for various goniometer orientations, as shown in Figure 5.1 c,d,e. Moreover, this system offers the convenience of offline testing before using it at a synchrotron facility. Furthermore, the transparency of glass capillaries makes our flow cell suitable for studying light-sensitive proteins using time-resolved diffraction methods. By integrating multiple fused silica capillary tubing inputs and incorporating mixing channels within the 3D-printed base, we've enabled the initiation of enzymatic reactions through mixing directly within the flow cell. Our aim with these designs is to make the technology more accessible for those who may not be experts in the field and to provide a practical solution for any macromolecular crystallography beamline with a rapid-readout X-ray detector that wants to offer SSX capabilities to its users. For easy reference and further analysis, we have deposited the relevant atomic coordinates and structure factor files from data collected using a 200 mm-diameter capillary in the PDB with the entry 8hua. Additional results can be found in Table 5.1 and Figure 5.2.

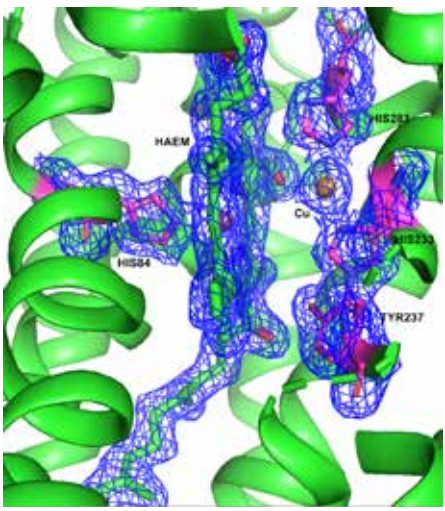

Figure 5.2: View of the final $2mF_o–DF_c$ electron density map of C*c*O haem a_3 active site. Density is contoured at 1.1σ.

Table 5.1: Serial-X flow results

	100 µm glass capillary	200 µm glass capillary	SFX structure
Diffraction source	BioMAX, MAX IV Laboratory	BioMAX, MAX IV Laboratory	SACLA BEAMLINE BL3
Temperature (K)	294	294	294
Space group	C121	C121	C121
a, b, c (Å)	145.4, 100.2, 96.6	146.1, 100.2, 96.6	145.9, 100.3, 96.6
α, β, γ (°)	90, 126.8, 90	90, 126.8, 90	90, 126.8, 90
Resolution (Å)‡	25.2–3.05 (3.16–3.05)	25.4–2.12 (2.20–2.12)	36.4–2.30 (2.34–2.30)
R_{split} (%)†‡	9.1 (65.9)	10.4 (78.1)	19.4 (120)
I/σ (I)‡	8.2 (1.5)	7.0 (1.2)	3.7 (1.02)
$CC_{1/2}$‡	99.1 (69.2)	99.1 (55.9)	95.6 (36.6)
Completeness (%)‡	100 (100)	100 (100)	100 (100)
Multiplicity‡	115.8 (76.8)	124.8 (82.7)	36.8 (14.7)
Collected images	263118	135000	87057
Indexed patterns	36702	65638	8211
Indexing rate (%)	13.9	48.6	9.4
Number of reflections	3539032	7887328	1864107
Number of unique reflections	30553	63185	50602
Refinement			
Resolution range (Å)		25.8–2.12	36.4–2.3
R_{work}/R_{free} (%)		15.1/18.8	16.2/19.8
Number of atoms		12953	6386
Average B factor (Å^2)		52	43.9
RMSD bonds (Å)		0.013	0.012
RMSD angles (°)		1.84	1.61

†$R_{split} = \left(\frac{1}{\sqrt{2}}\right) \frac{\sum_{hkl} |I_{even} - I_{odd}|}{0.5 \sum_{hkl} (I_{even} - I_{odd})}$

‡Values in parenthesis correspond to those of the highest-resolution shell.

5.2 Optimization of capillary-based SSX sample delivery for soluble proteins

As presented in chapter 5.1 we have developed a new method to deliver LCP crystals to the beam. The next step was to see if it could be used with other viscous matrices and for non-LCP samples since a significant percentage of crystal samples are not grown in LCP conditions. The idea was to test whether non-LCP crystals can be modified to mock-up LCP samples and to test all samples with different viscous matrices to show the flexibility of the set-up. Hemoglobin and lysozyme crystals were used for the study. Based on the literature search, monoolein, vacuum grease, HEC and Vaseline® have been chosen as viscous matrices for the study since those are the most common carrier media [67].

5.2.1 Results

Lysozyme and Hemoglobin crystals were used, they were crystalized as mentioned in 2.4 and 2.5, respectively. The first step was to test how crystals mix with the matrices, what the consistency of the LCP samples are (since for the set-up it needs to be a certain density to flow and not clog the system) and how long the crystals can survive in the mixture. A standardized protocol was devised to assess the resilience of crystals across various matrices. Once crystals are mixed with a viscous matrix (Figure 5.3a), the mixture is allowed to settle for an hour. Subsequently, a small sample is extracted (Figure 5.3b) and subjected to microscopic analysis (Figure 5.3c). Should the presence of crystals be evident, the process involves returning to the mixing phase, applying a few additional strokes, and then permitting a day for further incubation. After this day-long incubation, another minor sample is retrieved and examined under the microscope. If the crystals persist at this stage, the subsequent step involves the preparation of a fixed-target chip (Figure 5.3d), onto which a sample is placed for diffraction inspection. Positive outcomes at this juncture pave the way for advancement to the Serial-X beamtime stage (Figure 5.3e). In instances where the crystals endure the initial one-hour incubation but falter by the end of the day, a revised approach comes into play. These crystals undergo evaluation through shorter time fragments (every 2h), allowing for a more targeted assessment of their survival capacity. This protocol minimizes sample consumption before beamtime because a good condition can be found with only few microliters of crystal slurry and allows for offline testing before beamtime.

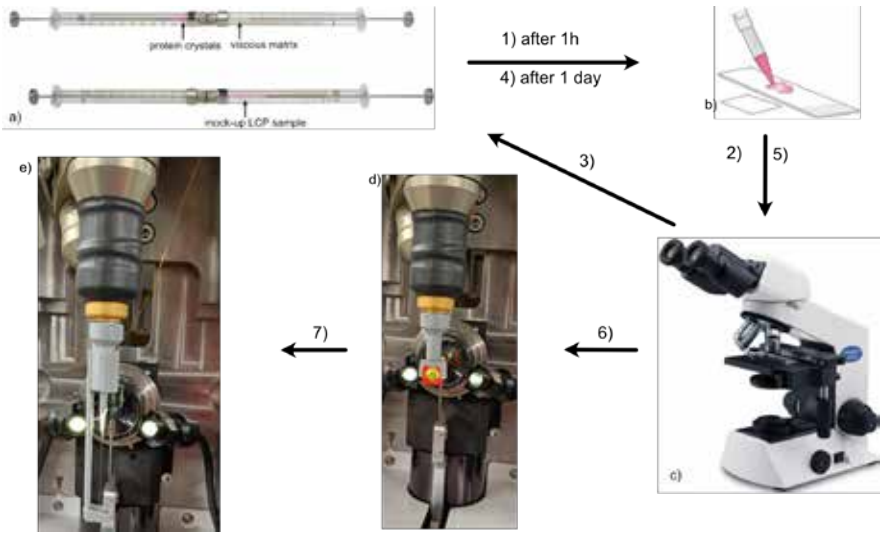

Figure 5.3: Protocol for mock-up LCP samples

The subsequent phase involved data collection, during which the following was collected: lysozyme in monoolein, vacuum grease, Vaseline® and HEC; hemoglobin in monoolein, vacuum grease and HEC. Various parameters were tested, including different exposure times, transmission settings, and the number of images captured per sample spot. From the collected data, it is evident that the samples exhibited diverse responses when mixed with the matrices. Notably, hemoglobin crystals displayed greater sensitivity to environmental changes compared to lysozyme crystals. Additionally, when hemoglobin was mixed with monoolein and left overnight, it induced changes in the space group of the crystals, as indicated in Table 5.2. Moreover, the influence of transmission and exposure time varied depending on the sample; it had a minimal impact on the results for lysozyme but significantly affected data quality for hemoglobin. In terms of the number of images per spot on the capillary, it was influenced by the viscosity of the matrix. The maximum number of images per spot (10,000) was achieved with HEC, followed by monoolein (8,000), vacuum grease (5,000), and lastly Vaseline® (3,000). These figures were determined by the appearance of visible black marks on the capillary and

the absence of crystal-diffracting images during data collection. Conducting a preliminary examination of a small sample before data collection proved invaluable in experiment planning. It not only conserved valuable samples but also underscored the significant impact of matrix choice on crystal survival rates. Therefore, it is imperative to assess the suitability of a viscous matrix for a specific protein crystal prior to beamtime, taking into account both sample survival and flow characteristics. To facilitate this, an offline station has been established at MicroMAX (Figure 5.4). In summary, this study demonstrates that the Serial-X flow cell can be effectively utilized for mock-up LCP samples. All the results are presented in Table 5.2,5.3,5.4 and Figures 5.5,5.6,5.7 for reference.

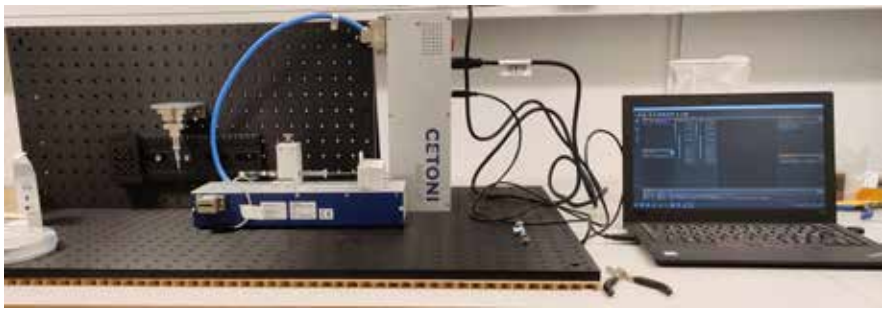

Figure 5.4: Offline testing setup for flow-cell at MicroMAX.

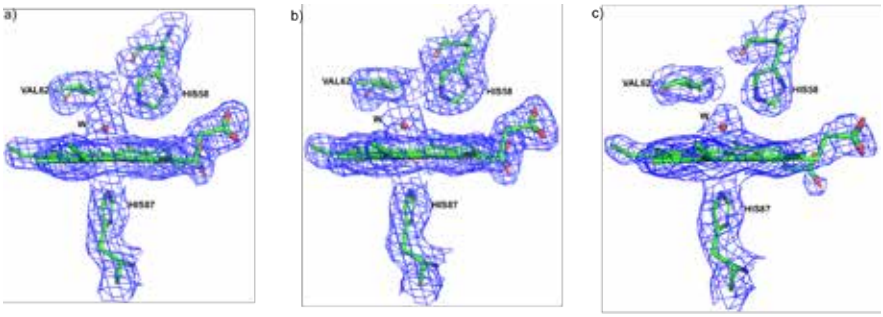

Figure 5.5: View of the final $2mF_o–DF_c$ electron density map. a) Heme pocket in α subunit from Hb in HEC, 80T, b) Heme pocket in α subunit from Hb in HEC, 100T, c) Heme pocket in α subunit from Hb in monoolein, 80T. Density is contoured at 1.1σ.

Table 5.2: Hemoglobin in different matrices results (T= % beam transmission)

	HEC, 80T, 20ms	HEC, 100T	Monoolein, 80T
Diffraction source	BioMAX, MAX IV Laboratory	BioMAX, MAX IV Laboratory	BioMAX, MAX IV Laboratory
Temperature (K)	294	294	294
Space group	C121	C121	$P2_12_12_1$
a, b, c (Å)	108.81, 63.04, 54.76	108.9, 63.01, 54.74	62.63, 80.91, 110.47
α, β, γ (°)	90, 111, 90	90, 111, 90	90
Resolution (Å)‡	53.56 – 2.5 (2.59 – 2.5)	53.56 – 2.35 (2.43 – 2.35)	30.13 – 2.8 (2.9 – 2.8)
R_{split} (%)†‡	18.36 (48.7)	11.36 (74.94)	17. 08 (54.16)
I/σ (I)‡	7.32 (2.11)	7.74 (1.32)	5.28 (2.03)
$CC_{1/2}$‡	0.9954 (0.6799)	0.9747 (0.45577)	0.971 (0.5213)
Completeness (%)‡	100 (100)	100 (100)	100 (100)
Multiplicity‡	65 (44)	70 (45)	40 (27)
Collected images	125808	140000	48000
Indexed patterns	13966	19523	9894
Indexing rate (%)	11.1	13.9	20.6
Number of reflections	788751	1024344	573133
Number of unique reflections	12105	14573	14400
Refinement			
Resolution range (Å)	53.56 – 2.5	53.56 – 2.35	30.13 – 2.8
R_{work}/R_{free} (%)	13.7/19.22	14.34/20.13	16.15/22.04
Number of atoms	4512	4511	9025
Average B factor (Å^2)	65	70	51
RMSD bonds (Å)	0.014	0.014	0.014
RMSD angles (°)	2.04	2.04	2.06

†$R_{split} = \left(\frac{1}{\sqrt{2}}\right) \frac{\sum_{hkl} |I_{even} - I_{odd}|}{0.5 \sum_{hkl} (I_{even} - I_{odd})}$

‡Values in parenthesis correspond to those of the highest-resolution shell.

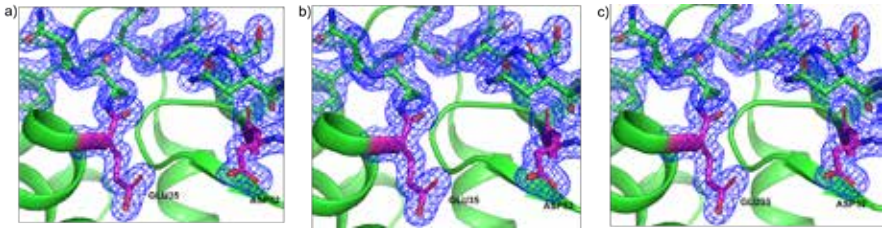

Figure 5.6: View of the final 2mF$_o$–DF$_c$ electron density map. a) Lysozyme active site in HEC 60T, b) Lysozyme active site in HEC 80T, c) Lysozyme active site in HEC 100T. Density is contoured at 1.1 σ.

Table 5.3: Lysozyme in HEC results (T= % beam transmission)

	60T	80T	100T
Diffraction source	BioMAX, MAX IV Laboratory	BioMAX, MAX IV Laboratory	BioMAX, MAX IV Laboratory
Temperature (K)	294	294	294
Space group	$P4_32_12$	$P4_32_12$	$P4_32_12$
a, b, c (Å)	79.24, 79.24, 38.15	79.25, 79.25, 38.16	79.28, 79.28, 38.19
α, β, γ (°)	90	90	90
Resolution (Å)‡	56.03 – 1.7 (1.76 – 1.7)	56.04 – 1.6 (1.66 – 1.6)	56.06 – 1.7 (1.76 – 1.7)
R_{split} (%)†‡	2.75 (23.61)	2.54 (53.61)	2.63 (35.55)
I/σ (I)‡	27.05 (1.53)	25.83 (0.51)	24.53 (1.02)
$CC_{1/2}$‡	0.9983 (0.8394)	0.9984 (0.7442)	0.9986 (0.8478)
Completeness (%)‡	100 (100)	100 (100)	100 (100)
Multiplicity‡	1673 (437)	1502 (209)	1132 (296)
Collected images	100000	100000	100000
Indexed patterns	90647	89944	70442
Indexing rate (%)	90.6	89.9	70.4
Number of reflections	23293240	24945986	15793384
Number of unique reflections	13919	16614	13955
Refinement			
Resolution range (Å)	56.03 – 1.7	56.04 – 1.65	56.06 – 1.7
R_{work}/R_{free} (%)	15.46/20.3	15.06/18.96	13.81/18.37
Number of atoms	2007	2011	2008
Average B factor (Å^2)	59	52	65
RMSD bonds (Å)	0.014	0.012	0.017
RMSD angles (°)	2.07	1.81	2.08

†$R_{split} = \left(\frac{1}{\sqrt{2}}\right) \frac{\sum_{hkl}|I_{even}-I_{odd}|}{0.5\sum_{hkl}(I_{even}-I_{odd})}$

‡Values in parenthesis correspond to those of the highest-resolution shell.

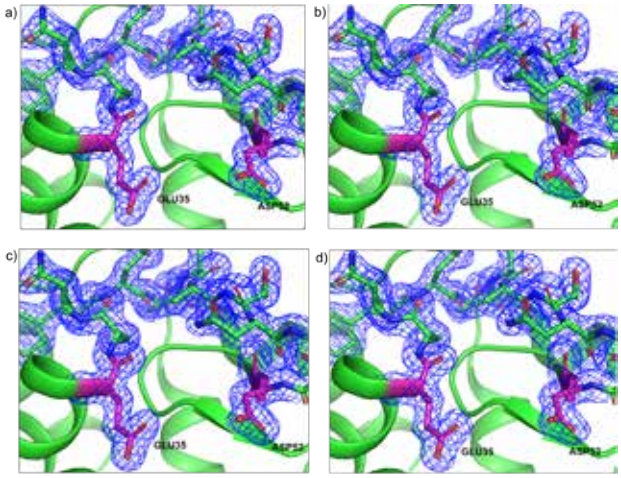

Figure 5.7: View of the final $2mF_o–DF_c$ electron density map. a) Lyz in Monoolein, 80T, b) Lyz in monoolein, 100T, c) Lyz in Vaseline®, 80T, d) Lyz in vacuum grease, 100T. Density is contoured at 1.1 σ.

Table 5.4: Lysozyme in monooleine, Vaseline® and vacuum grease results (T= % beam transmission)

Diffraction source	Monoolein 80T BioMAX, MAX IV Laboratory	Monoolein 100T BioMAX, MAX IV Laboratory	Vaseline® 80T BioMAX, MAX IV Laboratory	Vacuum grease 100T BioMAX, MAX IV Laboratory
Temperature (K)	294	294	294	294
Space group	$P4_32_12$	$P4_32_12$	$P4_32_12$	$P4_32_12$
a, b, c (Å)	79.15, 79.15, 38.08	79.20, 79.20, 38.1	79.43, 79.43, 38.03	79.25, 79.25, 38.16
α, β, γ (°)	90	90	90	90
Resolution (Å)‡	27.44 – 1.75 (1.83 – 1.75)	27.46 – 1.85 (1.92 – 1.85)	56.17 – 1.7 (1.76 – 1.7)	31.54 – 1.85 (1.92 – 1.85)
R_{split} (%)†‡	4. 66 (37.11)	7.12 (34.97)	3.06 (22.35)	4.73 (45.85)
I/σ (I)‡	19.93 (2.02)	14 (3.32)	23.64 (0.96)	12.63 (1.32)
$CC_{1/2}$‡	0.9952 (0.7282)	0.9898 (0.7242)	0.9976 (0.8897)	0.9973 (0.7355)
Completeness (%)‡	100 (100)	100 (100)	100 (100)	100 (100)
Multiplicity‡	442 (140)	147 (75)	802 (211)	363 (236)
Collected images	63000	60000	121000	224841
Indexed patterns	41855	18017	66778	39650
Indexing rate (%)	66.4	30	55.2	17.6
Number of reflections	5635365	1601052	11181042	3948367
Number of unique reflections	12743	10856	13943	10883
Refinement				
Resolution range (Å)	27.44 – 1.75	27.46 – 1.85	56.17 – 1.7	31.54 – 1.85
R_{work}/R_{free} (%)	13.93/18.22	14.13/17.17	13.77/18.32	14.27/17.36
Number of atoms	2022	2022	2022	2019
Average B factor (Å^2)	59	58	62	45
RMSD bonds (Å)	0.015	0.019	0.014	0.018
RMSD angles (°)	1.99	2.39	1.93	2.44

†$R_{split} = \left(\frac{1}{\sqrt{2}}\right) \frac{\sum_{hkl} |I_{even} - I_{odd}|}{0.5 \sum_{hkl} (I_{even} - I_{odd})}$

‡Values in parenthesis correspond to those of the highest-resolution shell.

5.3 AdaptoCell: microfluidic device for Serial Synchrotron crystallography

The AdaptoCell project [119] is funded by SSF (Stiftelsen för Strategisk Forskning) "AdaptoCell for MAX IV Laboratory users". Research in the project is made with the AdaptoCell team consisting of people from three MAX IV beamlines (Balder, CoSAXS and MicroMAX). AdaptoCell provides a microfluidic flow cell for academic and industrial users at MAX IV Laboratory. The adaptable flow cell will be integrated at three beamlines using different X-ray techniques. The available techniques are X-ray Absorption/Emission Spectroscopy (XAS/XES, Balder beamline) and Small Angle X-ray Scattering (SAXS, CoSAXS beamline), and Serial Crystallography (SSX, MicroMAX beamline). The microfluidic flow cell allows for time-resolved studies and reduces the risk of radiation damage as the sample is continuously renewed. Importantly, the device opens the venue for exploring mixing assays, with either active or passive mixing with a substrate, or change of experimental conditions, like pH or ionic strength. Available for all users are also offline flow station coupled to UV-vis spectroscopy on a microfluidic chip. For the microfluidic chips, there are different options depending on the sample and the experimental design. There are commercial polymer chips (e.g. COC (cyclo-olefin copolymer) chips from Microfluidic ChipShop and microfluidic chips in other materials such as glass-silicon-glass or polyimide (in collaboration with Customized Microfluidics, Uppsala University).

5.3.1 Chip fabrication

3D flow-focusing nozzle is printed using a 2-photon-polymerization (2PP) printer (NanoOne, UpNano, Austria). The chip is designed with Solidworks CAD software (Dassault systems, France) and the STL file is later imported into the printer software (Think3D, UpNano, Austria). The part is fabricated using UpPhoto ink (UpNano, Austria) in VAT mode with a 10x objective, using a coarse setting. Prior to printing, a quartz cube, used as a support for the printing, is silanized using the recommended protocol from UpNano. After printing, the part is carefully removed from the support and uncrosslinked ink is washed away through two 15-minute

washing steps with PEGMEA (Sigma-Aldrich, Sweden) followed by a 15-minute washing with IPA. The printed part has its main channel opened from the top and bottom (Figure 5.8a). After air drying, 8 µm thick polyimide foil (Goodfellow, UK) is applied onto 81 µm thick double-sided tape (Arcare 90445Q, Adhesive Research, Ireland) on both side of the chip. Fused silica capillaries, with an internal diameter of 100 µm and an external diameter of 170 µm (Genetec, Sweden), are glued with epoxy glue. Figure 5.8b and 5.10c shows an assembled chip.

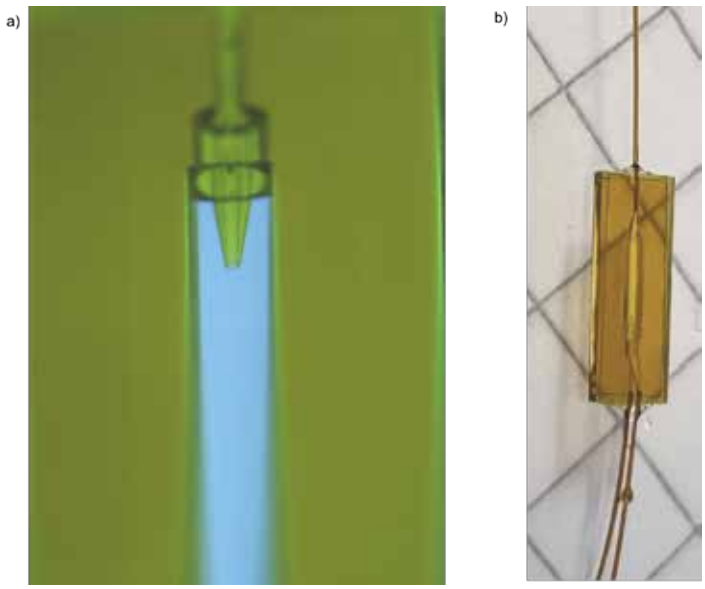

Figure 5.8: a) Chip after printing (viewing window width 500 µm and nozzle diameter 60 µm), b) fully assembled chip (total chip length 7 mm).

5.3.2 Chip characterization

The two inlet capillaries of the chip are connected to a pressure-driven pump (OB1-MK4, Elveflow, France) via high-pressure fitting (IDEX, Sweden). In order to image the flow pattern in 3D, micro-crystals are replaced by 3 µm fluorescent polystyrene microspheres (Fluorosphere, Invitrogen, Sweden) in a 10 µg/mL fluorescein salt buffer (Sigma-Aldrich, Sweden).

Sheath flow is replaced by a standard phosphate buffer (Sigma-Aldrich, Sweden). 3D imaging is performed with a Leica SP8 confocal microscope (Leica, Germany).

5.3.3 Results

3D flow focusing is imaged using fluorescent microparticles, mimicking micro-crystals, in a fluorescent buffer. By varying the respective pressures applied to the sample and the sheath buffer, hence varying flow rates, affects focusing of the sample (Figure 5.9a,b,c). Moreover, the axisymmetric design of the chip allows for a true three-dimensional focusing of the sample with a buffer sheath surrounding the middle sample stream.

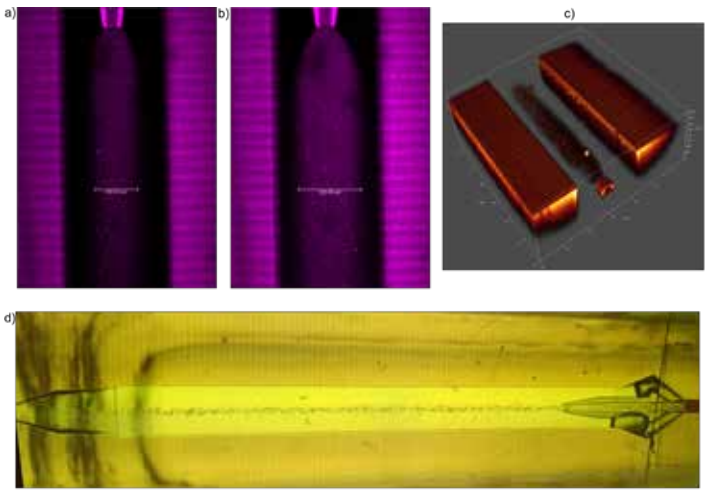

Figure 5.9: 3D flow focusing, a) sample pressure 240 mbar, buffer pressure 500 mbar (focused flow width 200 µm); b) sample pressure 400 mbar, buffer pressure 500 mbar (focused flow width 293 µm); c) Confocal image with flow seen in 3D ; d) Focused stream of lysozyme crystals

This project demanded extensive MX beamtime and rigorous testing. It involved multiple chip iterations before achieving success, as illustrated in Figure 5.10. Initially, we started with the COC chip since it had already proven effective for Balder and CoSAXS (XAS and SAXS). Regrettably,

the chip thickness of 1.3 mm COC was absorbing too much, resulting in no visible diffraction, even when shooting directly at a trapped crystal. Consequently, we pursued a 2D flow focusing thinner chip crafted from Kapton body with tape windows. However, this approach brought its own set of challenges, notably the dispersion of crystal flow after accumulation in one location due to interaction with the windows where the beam had direct contact with the sample (no sheath buffer). Subsequently, we realized the need for true 3D focusing where the sample is completely surrounded by the buffer sheath. Inspired by Hamburg-ESRF chip [70], we developed a chip design capable of 3D focused crystal flow, as depicted in Figure 5.9d. Depending on sample concentration and flow rate, this design allowed us to focus single crystals within the chip. Encouraged by this progress and the use of thin-walled Kapton tape (25 µm), we proceeded with a new beamtime. Unexpectedly, we encountered a novel issue involving the burning of the adhesive part on the Kapton tape, resulting in the formation of "sticky tentacles" that trapped crystals (Figure 5.11a,b,c), hindering further collection from the same point. We switched to Kapton foil for the subsequent beamtime, although the burning problem persisted (Figure 5.11d), albeit no longer in the form of "sticky tentacles", instead PEG in the buffer caused the burning. This prompted us to explore the possibility of reducing the PEG concentration in the buffer solution. Before implementing this change in the chip, we conducted offline experiments involving crystal mixing with lower PEG concentrations and assessed their viability through fixed-target collection. We successfully identified conditions that reduced PEG concentration by 60 %, with crystals remaining viable in the buffer for up to two days. This gave us the confidence to use this condition in the next beamtime.

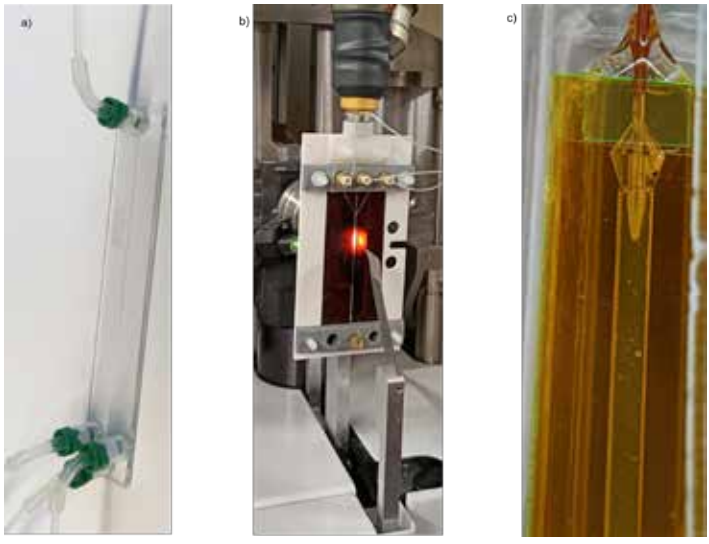

Figure 5.10: AdaptoCell chips used for SSX. a) Commercial Chip-Shop COC chip, b) 2D focusing Kapton chip, c) final chip

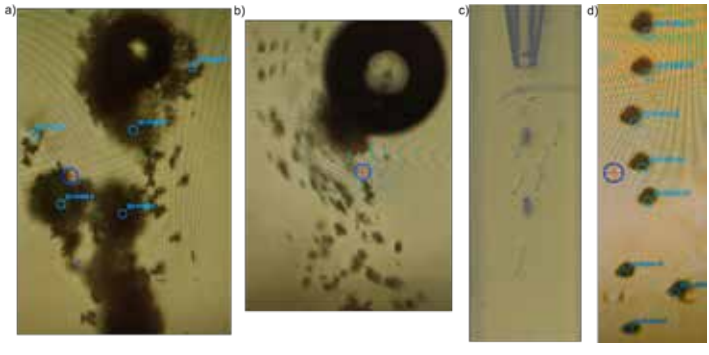

Figure 5.11: a) accumulation of crystals on the chip with Kapton tape windows, b) flow affected by burned part c) "sticky tentacles" as observed after beamtime under Keyence VHX-7000 microscope, d) burned marks from PEG (view from MXCuBE3)

For proof of concept, we employed lysozyme crystals (crystalized as

mentioned in 2.4). The results from the latest beamtime are presented in Table 5.5. While this beamtime was successful in preventing chip burning and flow disruption, an unforeseen issue arose: with the lower PEG concentration, crystals settled rapidly, causing system clogs. Consequently, our plans for the next beamtime include the incorporation of an anti-settler and further mixing experiments.

Table 5.5: Lysozyme results from AdaptoCell beamtime

	Lysozyme
Diffraction source	BioMAX, MAX IV Laboratory
Temperature (K)	294
Space group	$P4_32_12$
a, b, c (Å)	78.84, 78.84, 38.05
α, β, γ (°)	90
Resolution (Å)	35.26 – 3.5
R_{split} (%)	30.16
I/σ (I)	4.96
$CC_{1/2}$	0.8176
Completeness (%)	96.84
Multiplicity	9
Collected images	6500
Indexed patterns	467
Indexing rate (%)	7.2
Number of reflections	15224
Number of unique reflections	1678

$R_{split} = \left(\frac{1}{\sqrt{2}}\right) \frac{\sum_{hkl} |I_{even} - I_{odd}|}{0.5 \sum_{hkl} (I_{even} - I_{odd})}$

Chapter 6

RuBisCO

In this chapter I will present work connected to RuBisCO and initial TR-SSX preparation at BioMAX, including results from **Paper IV**.

6.1 Room-temperature Serial Synchrotron Crystallography structure of Spinacia oleracea RuBisCO: Towards Time-Resolved Structures (Paper IV)

The purpose of this paper was preparation for time-resolved serial synchrotron crystallography study on Spinacia oleracea RuBisCO carbon fixation at BioMAX. We present the first room-temperature SSX structure of RuBisCO. RuBisCO was purified as mentioned in 2.1.1 and crystallized as mentioned in 2.3, crystals can be seen in Figure 6.1.

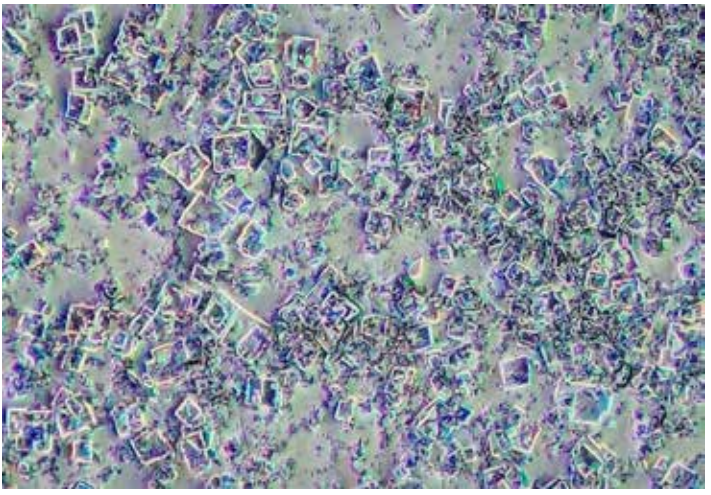

Figure 6.1: RuBisCO microcrystals.

6.1.1 SSX data collection

SpRub serial diffraction data were collected at the T-REXX endstation of the P14 beamline, operated by EMBL at PETRA-III (DESY, Hamburg). The protein crystals were loaded onto a silicon chip [76], which was then scanned at room temperature across the X-ray beam (12.7 keV, 10 µm diameter, 1.2 x 10^{12} photons/s) in a HARE pattern [120] at a rate of 30 positions per second. A pulsed ns laser (355 nm) was used for sample excitation, with 1 µJ/pulse measured at the sample position (focus diameter 30 µm FWHM). Diffraction images were recorded by an EIGER 4M (DECTRIS) detector with an exposure time of 5 ms.

A test TR-SSX structure of SpRb after mixing with the ribulose 1,5-bisphosphate (RuBP) was collected at BioMAX [21] using the 3D-printed flow cell [68]. Specifically, 16 µL 50 mM mNAAP was combined with 20 µL SpRub microcrystals slurry. To avoid data collection being compromised by microcrystal settling, we immersed these samples into monoolein at the ratio of 30:70 in favor of monoolein. Immediately prior to data collection, 10 µL 50 mM RuBP was also mixed into this slurry, which was loaded into a 100 µL Hamilton syringe and delivered using a CETONI Nemesys syringe pump. Sample viewing, alignment and measurement were carried

out using the beamline control software MXCuBE3 [118]. Diffraction data was collected at room temperature with an X-ray beam size of 20 x 5 μm^2 (FWHM), through a 20 µm diameter aperture, at a photon energy of 12.6 keV and flux of 2.7 x 10^{12} photons/s. Diffraction images were recorded by an EIGER 16M (DECTRIS) detector with an exposure time of 4 ms.

6.1.2 Data processing, model building and refinement

Diffraction data was indexed, integrated, merged and converted to MTZ format using CrystFEL 0.10.1 [88, 94]. The indexing rate was 32.1 %. Data truncation, phasing and structure refinement was performed in CCP4 Cloud [101]. High resolution structures of active SpRub (PDB ID 1AUS [121]) was used as models for molecular replacement with Phaser [99]. The structure was refined by one round of rigid body refinement using REFMAC5 [93, 102, 122], followed by several rounds of restrained refinement. Model building was done in Coot [52, 103] and all structural representation was made in PyMOL [104]. Room temperature SSX structures of active SpRub was obtained at 2.3 Å. Data collection and refinement statistics are presented in Table 6.1.

Table 6.1: Room-temperature SSX RuBisCO results

Diffraction source	PETRA III, T-REXX
Wavelength (Å)	0.976
Temperature (K)	294
PDB code	8QJ0
Space group	$C222_1$
a, b, c (Å)	158.60, 157.12, 202.74
α, β, γ (°)	90, 90, 90
Resolution (Å)‡	97.78 – 2.3 (2.382 – 2.3)
R_{split} (%)†‡	9.52 (23.88)
I/σ (I)‡	7.96 (3.66)
$CC_{1/2}$‡	0.9943 (0.9523)
Completeness (%)‡	100 (100)
Multiplicity‡	770 (528)
Collected images	334941
Indexed patterns	107372
Indexing rate (%)	32.1
Number of reflections	86314652
Number of unique reflections	112061
Refinement	
Resolution range (Å)	97.78 – 2.3
R_{work}/R_{free} (%)	18.18 – 22.81
Number of atoms	36278
Average B factor (Å^2)	25
RMSD bonds (Å)	0.015
RMSD angles (°)	2.16

†$R_{split} = \left(\frac{1}{\sqrt{2}}\right) \frac{\sum_{hkl} |I_{even} - I_{odd}|}{0.5 \sum_{hkl} (I_{even} - I_{odd})}$

‡Values in parenthesis correspond to those of the highest-resolution shell.

6.1.3 Results and discussion

Overall, the room temperature SSX structure of SpRub and that of 1AUS [121] are very similar. An internal distance matrix analysis of Cα-atom

position was used to compare structures [123,124] since this allows structures to be compared without the need to align them. This analysis showed that the internal distances between Cα atoms between pdb entry 1AUS and the refined SSX structure differ by only 0.11 Å when averaged over the four copies of RbcL, and by 0.12 Å when averaged over the four copies of RbcS (Figure 6.2a). These values are slightly higher than the corresponding average internal distance changes between the four copies of the molecule within the asymmetric unit, with the mean difference between the four protomers being 0.07 Å for RbcL and 0.06 Å for RbcS (Figure 6.2b). By mapping the average changes in internal distances on Cα atoms (Figure 6.2a) onto the protein structure (Figure 6.2c), we observe that several of the regions showing the largest structural perturbation relative to pdb entry 1AUS are located on the surface of the protein. Closer to the protein's active site, we note that Thr173 as well as three glycine residues (Gly381, Gly404, Gly405) (Figure 6.2d) show small but significant displacements relative to their positions in 1AUS. Since glycine residues introduce additional flexibility into the allowed backbone conformations, it is perhaps unsurprising that glycine-rich regions show modest disparities. From a functional perspective, it is significant that none of the residues that coordinate the active-site Mg^{+2} show significant displacements. Slightly further afield, all X-ray structures of RuBisCO to date show the disordering of residues 333 to 337 and, unsurprisingly, the boundaries to this disordered region are where the SSX deviates most from the coordinates of 1AUS.

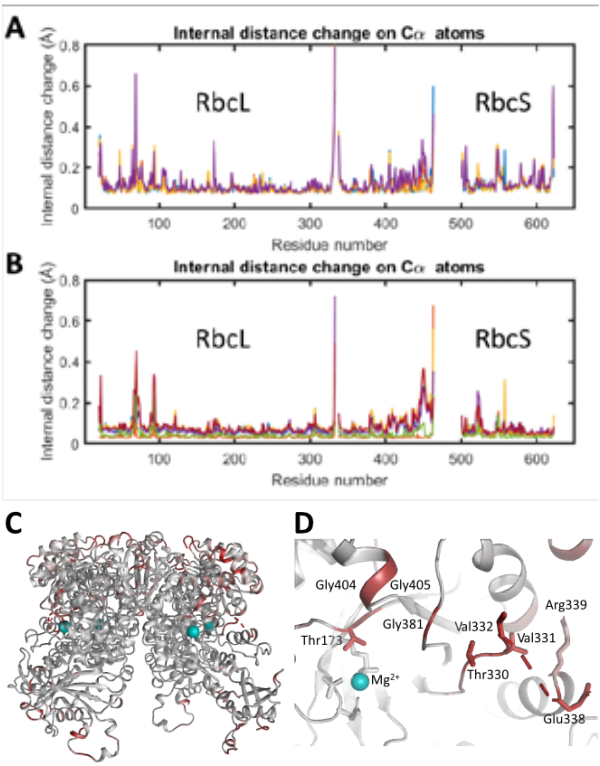

Figure 6.2: Structural comparisons of Cα-atom coordinates of the SSX structure of SpRub with an earlier single-crystal structure (1AUS) or between protomers. A) Average internal distance matrix displacements of Cα atoms when compared with the coordinates of pdb entry 1AUS. These plots are shown for all four copies of the large (RbcL) and small (RbcS) RuBisCO subunits within the asymmetric unity. B) Average internal distance matrix displacements of Cα atoms when compared with the coordinates of other copies of the large (RbcL) and small (RbcS) RuBisCO subunits within the asymmetric unity. C) Colour representation of the mean displacements of Cα-atoms relative to 1AUS, where white represents no displacement, and dark red represents the maximum displacement. Most regions where significant structural changes are observed are on the protein's surface. D) The same representation as used in C, but illustrating structural changes near the protein's active site.

At the protein's active site, all four RbcL protomers of the SSX structure show well-ordered electron density. Specifically, continuous electron density covalently connects the CO_2 molecule to Lys201, and the labile carbamate form of this residue coordinates Mg^{2+} (Figure 6.3a). Two other negatively charged residues, Asp203 and Glu204, coordinate Mg^{2+} as previously observed for the activated structure of RuBisCO without any ligand or substrate [121]. In addition, three water molecules coordinate Mg^{2+} to give the cation its characteristic six-fold coordination octahedral geometry. A fourth water molecule is well ordered in the immediate vicinity of the active site, also coordinating one water molecule that is bound to Mg^{2+}. The earlier single-crystal structure of the activated state of RuBisCO solved to 2.2 Å resolution (1AUS) shows three water molecules coordinating Mg^{2+} in one of the four RbcL protomers, but these water ligands were not built for all four protomers. Nevertheless, residual F^{obs}-F^{obs} electron density suggests that they may also have also been modeled for all protomers. A higher 1.6 Å resolution single-crystal structure but with bound inhibitor [10] reveals that the presence of a transition state analog (2-carboxyarabinitol bisphosphate) causes all three ligating water molecules to be displaced, with Mg^{2+} becoming coordinated by the C2 hydroxyl, the C3 hydroxyl and the 2'-carboxyl atoms of 2-carboxyarabinitol bisphosphate. Irrespectively, these observations suggest that the SSX active-structure arrangement is consistent with earlier work at a similar resolution.

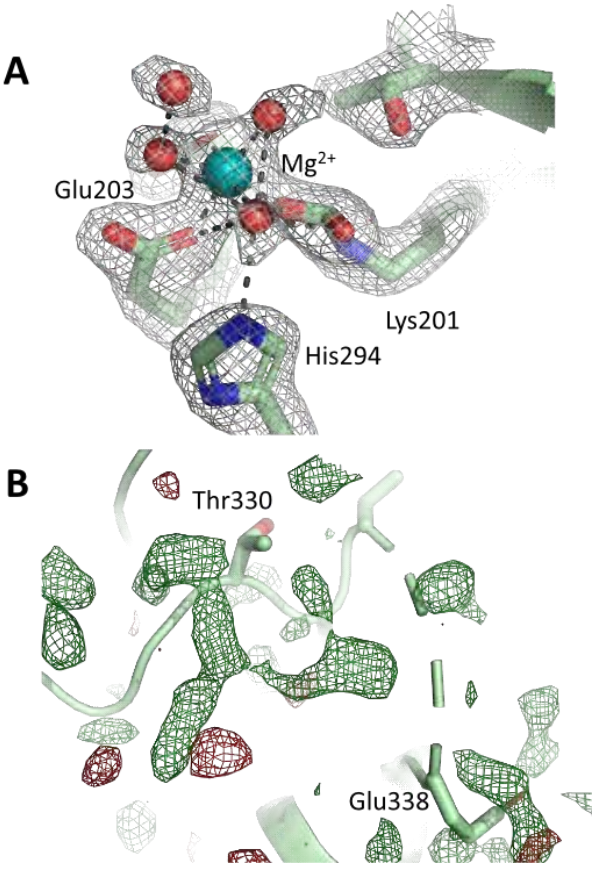

Figure 6.3: Electron density near the active site of SpRub. A) $2F^{obs}$-F^{calc} electron density map (grey) showing the quality of the map at the protein's active site. The labile carbamate form of $Lys201_L$ is clearly visible and has continuous electron density between the covalently bound CO_2 and the lysine side-chain. The active site Mg^{2+} ion shows identical ligands and water molecule coordination to earlier structures of RuBisCO, but with an additionally ordered water molecule on the outskirts of this water-cluster. B) F^{obs}-F^{calc} residual electron density map (forest green) showing residual, semi-continuous electron density near the disordered region from residues 333_L to 337_L.

6.1.4 Conclusion

Here we explored the foundations of a potential future TR-SSX study of SpRub. Most importantly, we obtained a room-temperature SSX structure of SpRub at 2.3 Å resolution, which showed high agreement with earlier single-crystal structures of this enzyme and without any obvious signs of radiation damage. As such, our data show that high-quality structures can be determined using serial crystallography protocols at synchrotron radiation sources.

6.2 Time-resolved serial synchrotron crystallography study on Spinacia oleracea RuBisCO carbon fixation

6.2.1 RuBisCO enzymatic activity

In order to enable the collection of time-resolved structural data, there needs to be a working system of reaction initiation, which should ideally be as uniform as possible. This is best achieved by a short laser pulse where there is a pump pulse initiating the reaction and a probing light at certain time delays after which would be X-rays in the case of a diffraction experiment. For substrate-dependent systems, this requires the use of substrate photo-cages. In the case of RuBisCO, carbon dioxide as well as the five-carbon sugar RuBP (Ribulose 1,5-bisphosphate) are possible options. Given the commercial availability of a carbon dioxide photo-cage, the mN-PAA [125], this is a viable option. This cage fulfills the requirements for its utilization; the time constant for the substrate formation is short (τ=200 ps) and the quantum yield is high (0.63), thus enabling a quick and uniform reaction initiation. The drawback of the cage is its relatively small extinction coefficient and the short wavelength for photoactivation (270 nm), which excludes many probe pulse light sources. Another hurdle for a successful time-resolved crystallographic experiment is the confirmation of enzymatic turnover. Given a spectroscopic signal of intermediates (and/or start- and end-state of the enzyme), this could be characterized in solution and potentially in crystal with a pump-probe set-up. For technical reasons, this is easier if the intermediate absorbs light in the UV/VIS/NIR part of

the electromagnetic spectrum, especially as relevant solvent molecules and protein residues generally do not absorb above 280 nm or below the mid-IR range. Unfortunately, the lack of such a chromophore for RuBisCO leaves IR-spectroscopy as the most appropriate option for the probe pulse. The signal-to-noise ratio in the presence of water, other solvent molecules, the photocage, and its photoproducts as well as that of the amino acids of the protein makes this a difficult option. On the other hand, the enzymatic turnover can be confirmed by coupling the enzymes' substrate consumption/or product generation to that of a chromophore readily measurable UV/VIS signal via several enzymes and substrates. This requires the bottleneck of this enzyme-coupled assay not to be limiting the detection of the product generation for the desired time scale of the probe. The product of the carbon dioxide fixation, 3-PGA (3-phosphoglycerate), can be coupled to the oxidation of NADH to NAD^+. NADH has an absorption peak at 340 nm with a molar extinction coefficient of 6220 $M^{-1}cm^{-1}$, which is completely absent for NAD^+. The scheme for this coupled enzyme assay can be described as the follows: Generation of 3-PGA from the reaction of RuBP (Ribulose 1,5-bisphosphate) and CO_2 has its phosphate group transferred to the second carbon resulting in the formation of 2-PGA (2-phosphoglycerate) by action of dPGM (phosphoglycerate mutase) via 2,3diPGA (2,3-bisphosphoglycerate). 2-PGA is further converted to PEP (phosphoenolpyruvate) catalyzed by enolase which is further catalyzed to pyruvate by PK (pyruvate kinase) in which the phosphate group is transferred to a molecule of ADP (adenosine diphosphate), thus forming ATP (adenosine triphosphate). The pyruvate is then reduced to lactate by LDH (lactate dehydrogenase) and the oxidation of NADH to NAD^+ [126]. Therefore one molecule of NADH is oxidized for each molecule of carbon dioxide fixated by the enzyme (Figure 6.4).

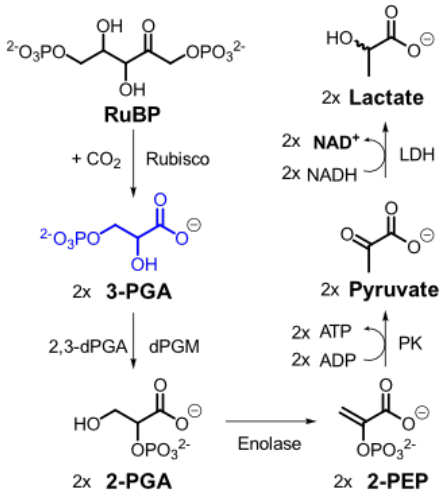

Figure 6.4: Scheme for the spectrophotometric assay method to determine RuBisCO activity in leaf extracts.

In addition to confirming enzymatic turnover, this assay can ensure that the enzyme is in its preactivated state. The activated state requires that the enzyme is in the presence of magnesium ions and carbon dioxide. This is ensured by the addition of magnesium chloride ($MgCl_2$), sodium bicarbonate ($NaHCO_3$) in addition to heating of the enzyme [127]. The rate of the enzymatic turnover can then be checked by the assay. As an initial test of the enzyme's activity, the assay was tested on the preactivated enzyme, resulting in 0.96 turnovers per enzyme per second (Figure 6.5).

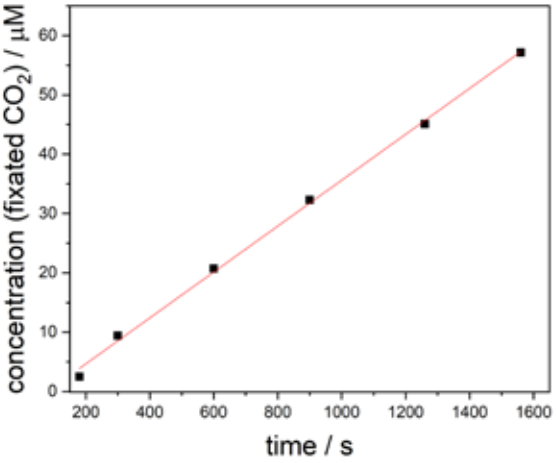

Figure 6.5: Initial test of enzyme activity in solution. Conditions: 40 nM RuBisCO, 20 mM $MgCl_2$, 20 mM $NaHCO_3$, 1 mM RuBP, 0.2 mM 2,3.diPGA, 3.75 U/mL dPGM, 12 U/mL PK, 2 mM ADP, 12 U/mL LDH, 0.2 mM NADH. The reaction was initiated by adding RuBP to the sample and was monitored in a 1 cm quartz cuvette.

In order to distinguish the activated and inactive enzyme, the assay was then performed with the inactive enzyme (no pre-heating of the sample with $MgCl_2$ and $NaHCO_3$), and following that the addition of $MgCl_2$ to the enzyme in order to see if that was sufficient for the recovery of enzymatic activity. As can be seen in Figure 6.6, the enzymatic activity is for the inactive form of the enzyme, but partially recovered by the addition of $MgCl_2$. The result of partial activation only by the addition of magnesium ions is an encouraging result as confirmation of state and the proper activation protocol could be problematic in crystals.

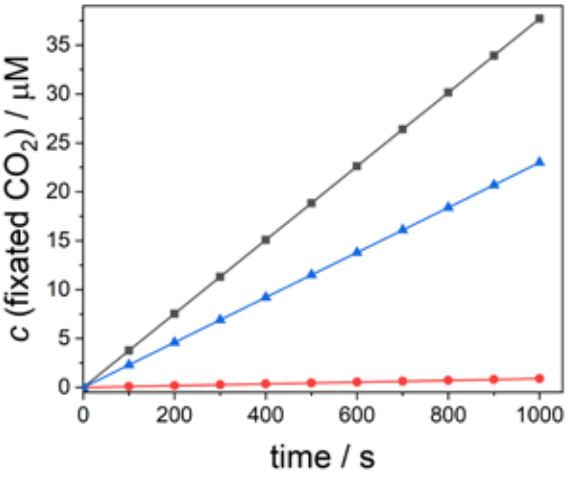

Figure 6.6: Comparison of enzyme activity in solution. Conditions: 40 nM RuBisCO, 20 mM $MgCl_2$, 20 mM $NaHCO_3$, 1 mM RuBP, 0.2 mM 2,3.diPGA, 3.75 U/mL dPGM, 12 U/mL PK, 2 mM ADP, 12 U/mL LDH, 0.2 mM NADH. The reaction was initiated by adding RuBP to the sample and was monitored in a 1 cm quartz cuvette. (gray line, addition of Mg^{2+} and then heating to 40 °C); blue line, the partially activated enzyme, addition of Mg^{2+} but not heated); red line, inactivated enzyme, no Mg^{2+} added)

In an attempt to further characterize the feasibility of a pump-probe diffraction experiment, the sample with enzyme-coupled assay components was put in a glass capillary (200 µm inner diameter) together with the carbon dioxide photo cage, mimicking the sample delivery during a time-resolved serial crystallography experiment. A probing light source was focused on the sample and the 340 nm absorption was monitored. No decay of the absorption was found, confirming the stability of the photo cage, sample compatibility and no significant thermal or other decay pathway for substrate release was seen. Furthermore, a LED (340 nm) was focused on the sample position after which spectra were collected confirmed significant NAD^+ formation and cage decomposition (Figure 6.7).

The photocage, and more significantly, the photo products of the carbon dioxide cage, has significant overlap in absorbance with NADH. After controlling for these spectral changes, the clear decrease of the NADH spectral signal could be seen (Figure 6.7).

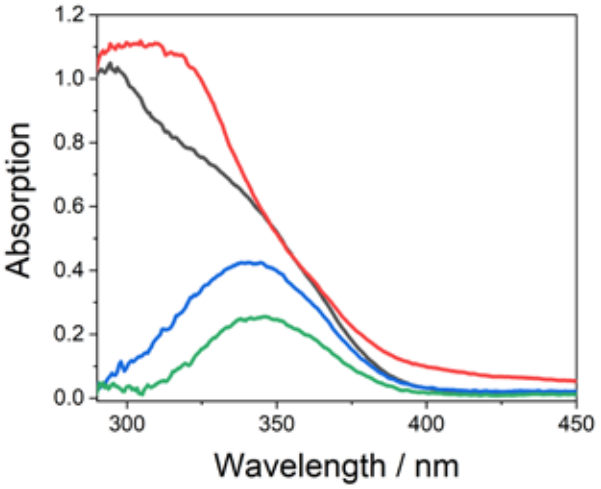

Figure 6.7: UV/VIS absorption spectrophotometry in a quartz capillary of the photo cage, the enzymatic coupling assay, RuBisCO (preactivated) and it's substrates. Conditions: 1 µM RuBisCO, 20 mM $MgCl_2$, 20 mM $NaHCO_3$, 2 mM RuBP, 0.4 mM 2,3.diPGA, 7.5 U/mL dPGM, 24 U/mL PK, 4 mM ADP, 24 U/mL LDH, 3 mM NADH, 13.5 mM mNPAA (Gray line: SpRub, enzyme assay components (including NADH), CO_2-cage as well as $MgCl_2$. Red line: SpRub, enzyme assay components (including NADH), CO_2-cage as well as $MgCl_2$ after 5s of illumination with 340nm LED. Blue line: same as the grey line, but with subtraction of the CO_2-cage spectrum. This shows the NADH spectrum. Green line: Same as the red line, but with subtraction by the 5sLED illuminated cage spectrum (this spectrum has three different cage chromophores).

The enzymatic activity came to 6.25 turnovers per enzyme per second during those five seconds of illumination, which is significantly faster than

in the static measurements. A potential reason for this could be the high concentration of carbon dioxide formed, which potentially exceeds that of the static measurements equilibrium between carbonate and dissolved carbon dioxide. This further encourages the feasibility of a pump-probe experiment. In a further step, the assay was tested with RuBisCO in crystal form. However, it was found out that the PEG8000 disturbs the assay, resulting in zero NAD^+ formation. The absence of PEG8000 turned out to dissolve the crystals, but a compromise of 1 % (v/v) PEG8000 was found not to dissolve the crystals while the assay still worked. The enzymatic activity was very slow however, and it cannot be said if the activity was slowed due to the fact that the enzyme was in the form of crystals, or if it is smaller concentrations of the dissolved enzyme that was responsible for the activity observed. In addition to this, the enzymatic concentration of the sample was not confidently determined.

6.2.2 BioMAX TR-SSX setup

To capture the different intermediate states we used a similar data collection scheme to the one in earlier study by Weinert [128] Figure 6.8.

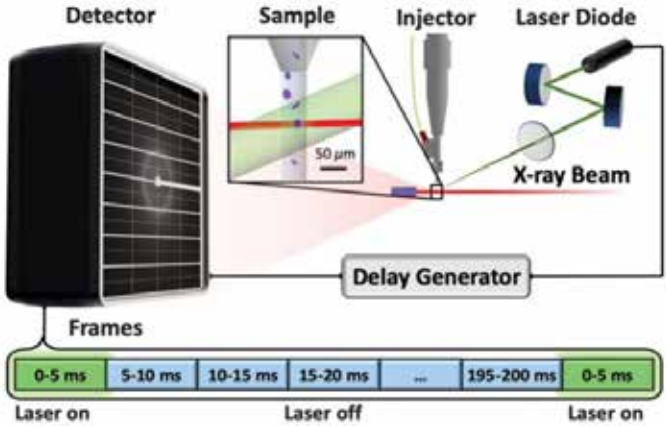

Figure 6.8: Schematic of experimental pump-probe setup for TR-SSX data collection. (Reproduced with permission from [128])

The laser used for this experiment was Thorlabs L375P70MLD (375 nm Laser Diode, 70 mW). The laser spot size was 100 µm with power of 55 mA, and it was aligned with Thorlabs moving stage to its final position (Figure 6.9 a). The SpRub crystals were first exposed to a laser for 20 ms, followed by a probe with X-ray of 13 keV energy and 80 % transmission. Diffraction data were collected with 4 ms exposure time per frame (Figure 6.9 b). Depending on the delay (distance) between the pump (laser excitation) and probe (X-ray radiation), different time points of the reaction were tracked, in this case, 100 and 1000 ms. The laser was controlled with a shutter so that it didn't shine continuously, as we saw that if the laser is turned on continuously it causes issues (will be discussed in 6.2.4). To achieve the collection scheme described above, two digital delay generators (DDGs) (DG645, Stanford Research Systems, USA) were used to synchronize the detector and laser. As shown in Figure 6.10, one DDG was used as a master to generate pulses with a repetition rate of 1.6 Hz, which defines a data collection cycle of 600 ms. The output pulse from master DDG triggered the second slave DDG, which then triggered the detector and laser shutter separately with 10 ms delay. The timings were confirmed by measuring the TTL signals from both DDGs with an oscilloscope.

Figure 6.9: TR-SSX setup at BioMAX. a) laser position at sample position, b) experiment viewed from control room, c) anti-settler setup, d) burning on the Serial-X glass capillary.

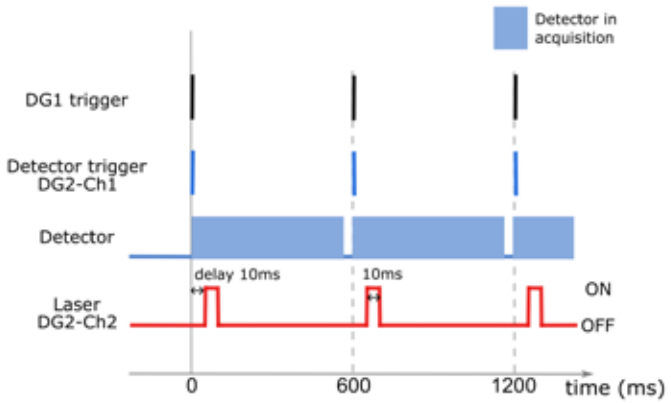

Figure 6.10: Triggering scheme for time-resolved pump-probe measurements

6.2.3 Sample preparation

Initially, RuBisCO microcrystals (crystalized as mentioned in 2.3) were combined with monoolein in a ratio of 30:70. However, the results from our initial beamtime indicated a need to modify the viscous medium, as the diffraction quality of the crystals had deteriorated. Consequently, following the protocol outlined in 5.2, we tested in HEC, Vazeline, vacuum grease, hyaluronic acid, pluronic F-127 and agarose. Best results were achieved with HEC and agarose, so we transitioned to using HEC and agarose as the medium for subsequent data collections, with a revised ratio of 60:40 for 20 % HEC and 20:30 for 5 % agarose. For the TR-SSX experiment, the sample preparation involved the initial mixing 50 µL 20 % HEC/30 µL 5 % agarose with 40 µL buffer (16 µL 50 mM mNAAP + 24 µL RuBisCO buffer), after that 20 µL RuBisCO microcrystals slurry was mixed in. Before data collection, 10 µL 50 mM RuBP was added to that LCP mixture.

6.2.4 Results

The initial beamtime served primarily as a trial run to assess the viability of our proposed setup at BioMAX. During this initial beamtime, we encountered the geometry limitation of goniometer, which prevented use of a shutter-controlled laser. Consequently, we had to rely on a continuous laser beam directed at the Serial-X flow cell. Despite facing technical challenges, we managed to collect data for two time points, specifically at 100 and 1000 milliseconds. The data processing yielded positive results, even though the resolution was relatively lower at 3.8 Å. As illustrated in Figure 6.11, the location of the green blob aligns with our expectations for the presence of RuBP. We used 1RCX [129] as a reference model.

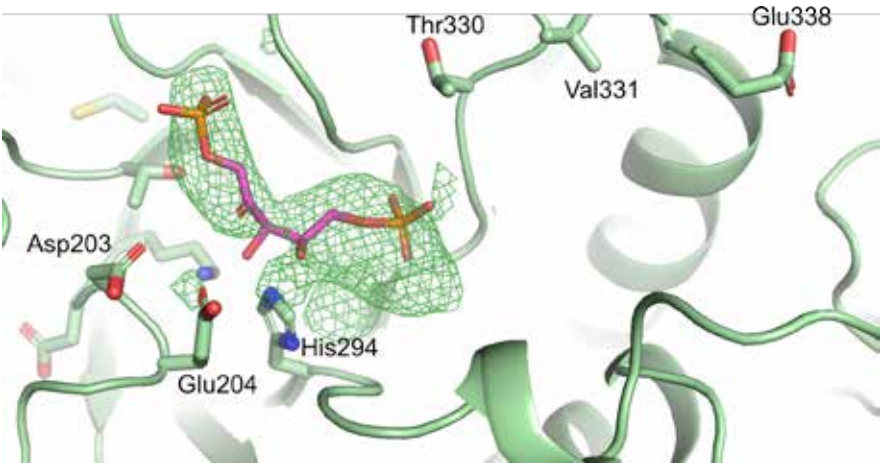

Figure 6.11: Green electron density in TR-SSX BioMAX experiment. Turquoise color is RuBP from PDB 1RCX [129].

The next step involved improving crystal diffraction, either by exploring new mediums or by collecting data in a solution. To achieve this, we prepared an anti-settler [130], depicted in Figure 6.9c. We subsequently tested crystals as outlined in 6.2.3. We first started with collection in solution. The anti-settler worked as intended; however, we encountered an unforeseen issue with the RuBisCO microcrystal solution. A part of the buffer solution contained PEG8000, which had previously caused problems (as discussed in section 6.2.1). This component led to sample burning (see Figure 6.9d) on the glass capillary, rendering data collection impossible. As a result, we had to transition to LCP collection. This time, we also incorporated a shutter (Figure 6.9a) on the laser, following our observation during the previous beamtime that continuous laser use for over two hours caused excessive capillary heating and crystal deposition. Our strategy remained consistent: collecting data at the same data points (100 and 1000ms) in the hope of achieving improved results to guide our next beamtime. Unfortunately, even though RuBisCO crystals diffracted better on their own compared to when they were in monoolein (reaching 2.7 Å for HEC and 2.8 Å in agarose), the data quality deteriorated to 4.2 Å when all the components were mixed for the time-resolved experiment. Moreover, we were unable to detect the expected sugar presence

in the form of the green blob. In conclusion, when all the components were combined the crystals started to degrade, rendering this method unfeasible for collection at BioMAX. Our last opportunity came during the beamtime at P14-TREXX, during which we collected seven chips with an HARE [120] pattern at a rate of 30 positions per second. We employed a pulsed nanosecond laser (355 nm) for sample excitation, with a measured energy of 1 µJ/pulse at the sample position (focus diameter of 30 µm FWHM). Regrettably, we still observed the absence of the green blob in the data during this beamtime. In response, we experimented with longer incubation times and higher sugar concentrations. However, increasing the sugar concentration led to crystal melting, and longer incubation times did not produce the desired results either.

6.2.5 Conclusion

Time-resolved serial X-ray crystallography is a rapidly growing field of research that encounters many challenges concerning sample preparation and reaction initiation [87]. RuBisCO is a potential target for such experiments since there is tremendous scientific interest in the chemical details of how CO_2 is removed from the atmosphere and incorporated into the biosphere on both agricultural and environmental grounds. Moreover, as a relatively slow reaction (turnover the order of 100 ms), the time-scale is well suited to validation using synchrotron radiation, even if TR-SFX studies using XFEL radiation may ultimately be necessary to optimize the resolution of collected data and to minimize the effects of X-ray induced photo-reduction of metal centres. Since microcrystals are grown using protein purified from a highly abundant native-source, sample quantities will not be a limiting factor. Moreover, since the laser induced release of CO_2 will lead to enzymatic turnover this seems to be a promising protocol. However, initial attempts to soak substrate into microcrystals either failed, or led to the crystals dissolving and the quality of X-ray diffraction data being severely compromised. As such, this strategy will need to be optimized, potentially by taking more care to minimize any potential sources of CO_2 or O_2 before crystals are mixed with the enzyme, and even exploring if viable strategies exist for co-crystallization of enzyme and

substrate. Alternatively, other reaction schemes may need to be considered, for example by exploring the diffusion of substrate into microcrystals following mixing as one possibility. Irrespectively, visualizing the enzyme-catalyzed fixation of CO_2 to a sugar precursor in three dimensions and in real time is an attractive scientific goal. It is therefore hoped that the progress reported here may inspire future work that overcomes several of these challenges and ultimately allows time-resolved serial crystallography studies to be pursued with maximum likelihood of success.

Chapter 7

Concluding remarks and future perspectives

This thesis represents a comprehensive exploration and practical implementation of various Serial Synchrotron Crystallography (SSX) methods at BioMAX, setting the stage for future applications at MicroMAX. The future of SSX experiments at MAX IV shines brightly as a result of these endeavors. In Chapter IV, we delve into several fixed-target techniques, showcasing their potential applications. In **Paper I**, we introduce an innovative MX-sample holder and protocol tailored for the collection of oxygen-sensitive samples using fixed-target methods. We have also developed custom 3D-printed tools to simplify the preparation of fixed-target Silson chips for oxygen-sensitive samples, as well as other sample types. In **Paper III**, we demonstrate the effective use of these fixed-target Silson chips and the newly designed Serial-X chips in obtaining room-temperature structures of human CYP3A4 at 2.95 Å resolution. This was compared to a high-resolution cryo-temperature structure, revealing valuable insights into temperature-induced structural changes within the active site. Furthermore, we have initiated preparations for *In-situ* data collection, a technique that has already been successfully employed for light-sensitive screening experiments and is now available to BioMAX users. Notably, our first experiment with Roadrunner II has laid a solid foundation for its future integration into MicroMAX Experiment hutch 2. In Chapter V, our focus shifts to the development of two distinct flow cells, catering to viscous and soluble samples. In **Paper II**, we introduce an innovative Serial-X flow cell, which has proven exceptionally effective in obtaining

high-quality SSX data from Cytochrome *c* oxidase. Notably, this innovative technology has been adopted on other beamlines globally. We also demonstrate the compatibility of this flow cell with various viscous matrices and provide a comprehensive protocol for preparing mock-up LCP samples. Equally significant, our efforts have resulted in the refinement of a microfluidic flow cell, AdaptoCell, designed for soluble samples, reaching its final form after numerous iterations. This achievement opens up exciting prospects for SSX research at MAX IV, including the ability to conduct mixing experiments and TR-SSX. Lastly, in Chapter VI, we presented the first room-temperature SSX structure of spinach RuBisCO (**Paper IV**) that was used for the first TR-SSX experiment at BioMAX albeit not fully successful. However, I believe that challenges with TR-SSX of RuBisCO can be overcome with further development. Possibly with the use of AdaptoCell microfluidic chip, finding new crystallizing conditions without PEG or preparing samples in the glovebox to eliminate competing oxygen.

Chapter 8

Svensk sammanfattning

Under det senaste decenniet har anmärkningsvärda framsteg inom femtosekunds-röntgenfrielektronlasrar (XFEL) åstadkommit en djupgående transformation inom strukturbiologin. Dessa XFELs har öppnat spännande möjligheter att utföra höghastighetsstudier i rumstemperatur av proteiners struktur och dynamik. Denna banbrytande metodik innefattar att tusentals kristaller i slumpmässiga orienteringar exponeras för röntgenstrålar vid rumstemperatur. Dessa innovationer har stimulerat framväxten av seriella kristallografitekniker, som har fått framgång på mer anpassningsbara och lättillgängliga mikrofokusstrålrör på synkrotronljusanläggningar. Det primära fokuset för avhandlingen kretsar kring utveckling och implementering av seriell synkrotronkristallografi för proteiner vid kristallografistrålrören BioMAX och MicroMAX, belägna vid MAX IV i Sverige. Avhandlingen omfattar utveckling av två innovativa provleveranssystem (Serial-X och AdaptoCell) och inkorporeringen av olika "fixed target"-metoder. I Artikel I introducerade vi ett nytt tillvägagångssätt för att samla in data från syrekänsliga prover med en "fixed target"-metoder, kompletterat med användning av 3D-utskrivna tillbehör. Artikel III visar en framgångsrik tillämpning av den metod som beskrivs i artikel I för att bestämma strukturen av CYP3A4. Artikel II fördjupar sig i skapandet av Serial-X-flödescellen, designad för effektiv leverans av viskösa prover, ett verktyg som har kommit till användning på många strållinjer över hela världen. Slutligen, i Artikel IV, presenterar vi den första seriella synkrotronkristallografistrukturen vid rumstemperatur av RuBisCo från spenat, tillsammans med förberedande steg för implementering av tidsupplöst seriell synkrotronkristallografi vid BioMAX.

Bibliography

[1] B. Rupp, *Biomolecular Crystallography*. Garland Science, Taylor & Francis Group, LLC, New York, 10 2009.

[2] C. B. Anfinsen, "Principles that govern the folding of protein chains," *Science*, vol. 181, pp. 223–230, 7 1973.

[3] J. Smith, "Chemical kinetics and reaction mechanisms," *The Chemical Engineering Journal*, vol. 25, no. 1, p. 122, 1982.

[4] H. Bartels and R. Baumann, "Respiratory function of hemoglobin.," *The New England Journal of Medicine*, vol. 338, pp. 239–247, 1 1998.

[5] M. Perutz, M. Rossmann, A. F. Cullis, H. Muirhead, G. Will, and A. C. T. North, "Structure of hemoglobin," *Nature*, vol. 185, pp. 416–422, 1960.

[6] F. Yang and G. N. Phillips, "Crystal structures of CO-, Deoxy- and Met-myoglobins at various pH values," *J. Mol. Biol.*, vol. 256, no. 4, pp. 762–774, 1996.

[7] H. Morrison, "Lysozyme," in *Enzyme Active Sites and their Reaction Mechanisms*, pp. 121–127, 2021.

[8] S. Venkataramani, J. Truntzer, and D. R. Coleman, "Thermal stability of high concentration lysozyme across varying pH: A Fourier Transform Infrared study," *J. Pharm. Bioallied Sci*, vol. 5, no. 2, pp. 148–153, 2013.

[9] D. C. Phillips, "The three-dimensional structure of an enzyme molecule.," *Scientific American*, vol. 215, no. 5, pp. 78–90, 1966.

[10] I. Andersson, "Large structures at high resolution: The 1.6 Å crystal structure of spinach ribulose-1,5-bisphosphate carboxylase/oxygenase complexed with 2-carboxyarabinitol bisphosphate," *J. Mol. Biol.*, vol. 259, no. 1, pp. 160–174, 1996.

[11] V. R. Kaila, M. I. Verkhovsky, and M. Wikström, "Proton-coupled electron transfer in cytochrome oxidase," *Chemical Reviews*, vol. 110, pp. 7062–7081, 12 2010.

[12] T. Soulimane, G. Buse, G. P. Bourenkov, H. D. Bartunik, R. Huber, and M. E. Than, "Structure and mechanism of the aberrant ba3-cytochrome c oxidase from Thermus thermophilus," *EMBO Journal*, vol. 19, pp. 1766–1776, 4 2000.

[13] A. Giuffrè, E. Forte, G. Antonini, E. D'Itri, M. Brunori, T. Soulimane, and G. Buse, "Kinetic properties of ba3 oxidase from Thermus thermophilus: Effect of temperature," *Biochemistry*, vol. 38, no. 3, pp. 1057–1065, 1999.

[14] S. Rendic and F. P. Guengerich, "Survey of human oxidoreductases and cytochrome P450 enzymes involved in the metabolism of xenobiotic and natural chemicals," *Chemical Research in Toxicology*, vol. 28, pp. 38–42, 1 2015.

[15] F. P. Guengerich, M. R. Waterman, and M. Egli, "Recent Structural Insights into Cytochrome P450 Function," *Trends in Pharmacological Sciences*, vol. 37, pp. 625–640, 8 2016.

[16] H. W. Wang, "A commentary of "Cryo-EM achieves atomic resolution" in 10 remarkable discoveries from 2020 in Nature," *Fundamental Research*, vol. 2, pp. 349–350, 3 2022.

[17] J. C. Kendrew, G. Bodo, H. M. Dintzis, R. G. Parrish, H. Wyckoff, and D. C. Phillips, "A Three-Dimensional Model of the Myoglobin Molecule Obtained by X-Ray Analysis," *Nature 1958 181:4610*, vol. 181, pp. 662–666, 3 1958.

[18] F. D. Fuller, S. Gul, R. Chatterjee, E. Sethe Burgie, I. D. Young, H. Lebrette, V. Srinivas, A. S. Brewster, T. Michels-Clark, J. A. Clinger, B. Andi, M. Ibrahim, E. Pastor, C. De Lichtenberg, R. Hussein, C. J. Pollock, M. Zhang, C. A. Stan, T. Kroll, T. Fransson, C. Weninger, M. Kubin, P. Aller, L. Lassalle, P. Bräuer, M. D. Miller, M. Amin, S. Koroidov, C. G. Roessler, M. Allaire, R. G. Sierra, P. T. Docker, J. M. Glownia, S. Nelson, J. E. Koglin, D. Zhu, M. Chollet, S. Song, H. Lemke, M. Liang, D. Sokaras, R. Alonso-Mori, A. Zouni, J. Messinger, U. Bergmann, A. K. Boal, J. Martin Bollinger, C. Krebs, M. Högbom, G. N. Phillips, R. D. Vierstra, N. K. Sauter, A. M. Orville, J. Kern, V. K. Yachandra, and J. Yano, "Drop-on-demand sample delivery for studying biocatalysts in action at X-ray free-electron lasers," *Nature Methods*, vol. 14, pp. 443–449, 2 2017.

[19] M. Eriksson, J. Friso Van Der Veen, and C. Quitmann, "Diffraction-limited storage rings-a window to the science of tomorrow," *J. Synchrotron Rad.*, vol. 21, pp. 837–842, 2014.

[20] J. M. Grimes, D. R. Hall, A. W. Ashton, G. Evans, R. L. Owen, A. Wagner, K. E. McAuley, F. Von Delft, A. M. Orville, T. Sorensen, M. A. Walsh, H. M. Ginn, and D. I. Stuart, "Where is crystallography going?," *Acta Cryst. D*, vol. 74, pp. 152–166, 2 2018.

[21] T. Ursby, K. Åhnberg, R. Appio, O. Aurelius, A. Barczyk, A. Bartalesi, M. Bjelčić, F. Bolmsten, Y. Cerenius, R. B. Doak, M. Eguiraun, T. Eriksson, R. J. Friel, I. Gorgisyan, A. Gross, V. Haghighat, F. Hennies, E. Jagudin, B. N. Jensen, T. Jeppsson, M. Kloos, J. Lidon-Simon, G. M. A. De Lima, R. Lizatovic, M. Lundin, A. Milan-Otero, M. Milas, J. Nan, A. Nardella, A. Rosborg, A. Shilova, R. L. Shoeman, F. Siewert, P. Sondhauss, V. O. Talibov, H. Tarawneh, J. Thånell, M. Thunnissen, J. Unge, C. Ward, A. Gonzalez, and U. Mueller, "BioMAX-the first macromolecular crystallography beamline at MAX IV Laboratory," *J. Synchrotron Rad.*, vol. 27, pp. 1415–1429, 2020.

[22] E. F. Garman, "Radiation damage in macromolecular crystallography: What is it and why should we care?," *Acta Cryst. D*, vol. 66, pp. 339–351, 3 2010.

[23] Springer Protocols Handbooks, *Advanced Methods in Structural Biology*. Springer Tokyo, 2016.

[24] R. C. Stevens, "Design of high-throughput methods of protein production for structural biology," *Structure*, vol. 8, pp. R177–R185, 9 2000.

[25] G. L. Rosano and E. A. Ceccarelli, "Recombinant protein expression in Escherichia coli: Advances and challenges," *Frontiers in Microbiology*, vol. 5, no. APR, 2014.

[26] M. Wishnick and M. Daniel Lane, "Ribulose Diphosphate Carboxylase from Spinach Leaves," *Methods in Enzymology*, vol. 23, no. C, pp. 570–577, 1971.

[27] S. D. Durbin and G. Feher, "Protein crystallization," *Annual Review of Physical Chemistry*, vol. 47, pp. 171–204, 11 1996.

[28] A. Bijelic and A. Rompel, "Polyoxometalates: more than a phasing tool in protein crystallography," *ChemTexts*, vol. 4, pp. 1–27, 8 2018.

[29] N. Asherie, "Protein crystallization and phase diagrams," *Methods*, vol. 34, pp. 266–272, 11 2004.

[30] A. Shilova, H. Lebrette, O. Aurelius, J. Nan, M. Welin, R. Kovacic, S. Ghosh, C. Safari, R. J. Friel, M. Milas, Z. Matej, M. Hogbom, G. Branden, M. Kloos, R. L. Shoeman, B. Doak, T. Ursby, M. Hakansson, D. T. Logan, and U. Mueller, "Current status and future opportunities for serial crystallography at MAX IV Laboratory," *J. Synchrotron Rad.*, vol. 27, pp. 1095–1102, 2020.

[31] A. A. Chernov, "Estimates of internal stress and related mosaicity in solution grown crystals: Proteins," *J. Cryst. Growth*, vol. 196, pp. 524–534, 1 1999.

[32] T. Weinert, N. Olieric, R. Cheng, S. Brünle, D. James, D. Ozerov, D. Gashi, L. Vera, M. Marsh, K. Jaeger, F. Dworkowski, E. Panepucci, S. Basu, P. Skopintsev, A. S. Doré, T. Geng, R. M. Cooke, M. Liang, A. E. Prota, V. Panneels, P. Nogly, U. Ermler, G. Schertler, M. Hennig, M. O. Steinmetz, M. Wang, and J. Standfuss, "Serial millisecond crystallography for routine room-temperature structure determination at synchrotrons," *Nature Communications*, vol. 8, no. 1, 2017.

[33] C. Kupitz, S. Basu, I. Grotjohann, R. Fromme, N. A. Zatsepin, K. N. Rendek, M. S. Hunter, R. L. Shoeman, T. A. White, D. Wang, D. James, J. H. Yang, D. E. Cobb, B. Reeder, R. G. Sierra, H. Liu, A. Barty, A. L. Aquila, D. Deponte, R. A. Kirian, S. Bari, J. J. Bergkamp, K. R. Beyerlein, M. J. Bogan, C. Caleman, T. C. Chao, C. E. Conrad, K. M. Davis, H. Fleckenstein, L. Galli, S. P. Hau-Riege, S. Kassemeyer, H. Laksmono, M. Liang, L. Lomb, S. Marchesini, A. V. Martin, M. Messerschmidt, D. Milathianaki, K. Nass, A. Ros, S. Roy-Chowdhury, K. Schmidt, M. Seibert, J. Steinbrener, F. Stellato, L. Yan, C. Yoon, T. A. Moore, A. L. Moore, Y. Pushkar, G. J. Williams, S. Boutet, R. B. Doak, U. Weierstall, M. Frank, H. N. Chapman, J. C. Spence, and P. Fromme, "Serial time-resolved crystallography of photosystem II using a femtosecond X-ray laser," *Nature*, vol. 513, no. 7517, pp. 261–265, 2014.

[34] M. Caffrey, "A comprehensive review of the lipid cubic phase or in meso method for crystallizing membrane and soluble proteins and complexes," *Acta Cryst. F*, vol. 71, pp. 3–18, 1 2015.

[35] R. Andersson, C. Safari, P. Bath, R. Bosman, A. Shilova, P. Dahl, S. Ghosh, A. Dunge, R. Kjeldsen-Jensen, J. Nan, R. L. Shoeman, M. Kloos, R. B. Doak, U. Mueller, R. Neutze, and G. Brändén, "Well-based crystallization of lipidic cubic phase microcrystals for serial X-ray crystallography experiments," *Acta Cryst. D*, vol. 75, pp. 937–946, 10 2019.

[36] I. Andersson, A. C. Tjäder, E. Cedergren-Zeppezauer, and C. I. Brändén, "Crystallization and preliminary x-ray studies of spinach ribulose 1,5-bisphosphate carboxylase/oxygenase complexed with activator and a transition state analogue.," *J. Biol. Chem.*, vol. 258, no. 23, pp. 14088–14090, 1983.

[37] T. Lundqvist and G. Schneider, "Crystal structure of activated ribulose-1,5-bisphosphate carboxylase complexed with its substrate, ribulose-1,5-bisphosphate," *Journal of Biological Chemistry*, vol. 266, no. 19, pp. 12604–12611, 1991.

[38] A. Sato-Tomita and N. Shibayama, "Size and Shape Controlled Crystallization of Hemoglobin for Advanced Crystallography," *Crystals*, vol. 7, p. 282, 9 2017.

[39] R. A. Novelline, *Squire's Fundamentals of Radiology*. Harvard University Press, 1997.

[40] "The Electromagnetic Spectrum - Mini Physics - Learn Physics, https://www.miniphysics.com/electromagnetic-spectrum_25.html. Accessed 21 September 2023.," 2016.

[41] A. Hofmann, "Synchrotron Radiation," in *Reviews of Accelerator Science and Technology*, pp. 121–141, WORLD SCIENTIFIC, 12 2008.

[42] "Birkbeck College, University of London, "How do Synchrotrons Work?", http://pd.chem.ucl.ac.uk/pdnn/inst2/work.htm. Accessed 21 September 2023."

[43] W. H. Bragg, "The reflection of X-rays by crystals," *Nature*, vol. 91, no. 2280, p. 477, 1913.

[44] P. P. Ewald, "Introduction to the dynamical theory of X-ray diffraction," *Acta Cryst. A*, vol. 25, no. 1, pp. 103–108, 1969.

[45] G. Rhodes, *Crystallography Made Crystal Clear: A Guide for Users of Macromolecular Models, Third Edition*. Elsevier, 1 2006.

[46] "Martín Martínez-Ripoll, "Experimental diffraction. Evaluating the diffraction pattern", https://www.xtal.iqfr.csic.es/Cristalografia/parte_06_2-en.html. Accessed 21 September 2023.."

[47] "Britannica, The Editors of Encyclopaedia. "Bragg law". Encyclopedia Britannica, 15 Mar. 2022, https://www.britannica.com/science/Bragg-law. Accessed 21 September 2023.."

[48] J. E. Penner-Hahn, "X-ray Absorption Spectroscopy," in *Comprehensive Coordination Chemistry II*, vol. 2, pp. 159–186, Pergamon, 1 2003.

[49] J. Yano and V. K. Yachandra, "X-ray absorption spectroscopy," *Photosynthesis Research*, vol. 102, pp. 241–254, 11 2009.

[50] K. Rajashankar and Z. Dauter, "Data collection for crystallographic structure determination," *Methods in Molecular Biology*, vol. 1140, pp. 211–237, 2014.

[51] P. Mehrabi, S. Sung, D. von Stetten, A. Prester, C. E. Hatton, S. Kleine-Döpke, A. Berkes, G. Gore, J. P. Leimkohl, H. Schikora, M. Kollewe, H. Rohde, M. Wilmanns, F. Tellkamp, and E. C. Schulz, "Millisecond cryo-trapping by the spitrobot crystal plunger simplifies time-resolved crystallography," *Nature Communications*, vol. 14, pp. 1–9, 4 2023.

[52] P. Emsley and K. Cowtan, "Coot: Model-building tools for molecular graphics," *Acta Cryst. D*, vol. 60, no. 12 I, pp. 2126–2132, 2004.

[53] J. W. Pflugrath, "Practical macromolecular cryocrystallography," *Acta Cryst. F*, vol. 71, pp. 622–642, 2015.

[54] J. M. Holton, "A beginner's guide to radiation damage," *J. Synchrotron Rad.*, vol. 16, pp. 133–142, 2 2009.

[55] K. Jang, H. G. Kim, S. H. S. Hlaing, M. Kang, H. W. Choe, and Y. J. Kim, "A Short Review on Cryoprotectants for 3D Protein Structure Analysis," *Crystals*, vol. 12, p. 138, 2 2022.

[56] A. Burkhardt, T. Pakendorf, B. Reime, J. Meyer, P. Fischer, N. Stübe, S. Panneerselvam, O. Lorbeer, K. Stachnik, M. Warmer, P. Rödig, D. Göries, and A. Meents, "Status of the crystallography beamlines at PETRA III," *European Physical Journal Plus*, vol. 131, pp. 1–9, 3 2016.

[57] J. A. Wojdyla, E. Panepucci, I. Martiel, S. Ebner, C. Y. Huang, M. Caffrey, O. Bunk, and M. Wang, "Fast two-dimensional grid and transmission X-ray microscopy scanning methods for visualizing and characterizing protein crystals," *Journal of Applied Crystallography*, vol. 49, pp. 944–952, 5 2016.

[58] A. A. McCarthy, R. Barrett, A. Beteva, H. Caserotto, F. Dobias, F. Felisaz, T. Giraud, M. Guijarro, R. Janocha, A. Khadrouche, M. Lentini, G. A. Leonard, M. Lopez Marrero, S. Malbet-Monaco, S. McSweeney, D. Nurizzo, G. Papp, C. Rossi, J. Sinoir, C. Sorez, J. Surr, O. Svensson, U. Zander, F. Cipriani, P. Theveneau, and C. Mueller-Dieckmann, "ID30B – a versatile beamline for macromolecular crystallography experiments at the ESRF," *Journal of Synchrotron Radiation*, vol. 25, pp. 1249–1260, 7 2018.

[59] H. N. Chapman, C. Caleman, and N. Timneanu, "Diffraction before destruction," *Philosophical Transactions of the Royal Society B: Biological Sciences*, vol. 369, 7 2014.

[60] K. Diederichs and M. Wang, *Serial synchrotron X-ray crystallography (SSX)*, vol. 1607. Humana Press Inc., 2017.

[61] H. N. Chapman, P. Fromme, A. Barty, T. A. White, R. A. Kirian, A. Aquila, M. S. Hunter, J. Schulz, D. P. Deponte, U. Weierstall, R. B. Doak, F. R. Maia, A. V. Martin, I. Schlichting, L. Lomb, N. Coppola, R. L. Shoeman, S. W. Epp, R. Hartmann, D. Rolles, A. Rudenko, L. Foucar, N. Kimmel, G. Weidenspointner, P. Holl, M. Liang, M. Barthelmess, C. Caleman, S. Boutet, M. J. Bogan, J. Krzywinski, C. Bostedt, S. Bajt, L. Gumprecht, B. Rudek, B. Erk, C. Schmidt, A. Hömke, C. Reich, D. Pietschner, L. Ströder, G. Hauser, H. Gorke, J. Ullrich, S. Herrmann, G. Schaller, F. Schopper, H. Soltau, K. U. Kühnel, M. Messerschmidt, J. D. Bozek, S. P. Hau-Riege, M. Frank, C. Y. Hampton, R. G. Sierra, D. Starodub, G. J. Williams, J. Hajdu, N. Timneanu, M. M. Seibert, J. Andreasson, A. Rocker, O. Jönsson, M. Svenda, S. Stern, K. Nass,

R. Andritschke, C. D. Schröter, F. Krasniqi, M. Bott, K. E. Schmidt, X. Wang, I. Grotjohann, J. M. Holton, T. R. Barends, R. Neutze, S. Marchesini, R. Fromme, S. Schorb, D. Rupp, M. Adolph, T. Gorkhover, I. Andersson, H. Hirsemann, G. Potdevin, H. Graafsma, B. Nilsson, and J. C. Spence, "Femtosecond X-ray protein nanocrystallography," *Nature*, vol. 470, no. 7332, pp. 73–78, 2011.

[62] M. O. Wiedorn, D. Oberthür, R. Bean, R. Schubert, N. Werner, B. Abbey, M. Aepfelbacher, L. Adriano, A. Allahgholi, N. Al-Qudami, J. Andreasson, S. Aplin, S. Awel, K. Ayyer, S. Bajt, I. Barák, S. Bari, J. Bielecki, S. Botha, D. Boukhelef, W. Brehm, S. Brockhauser, I. Cheviakov, M. A. Coleman, F. Cruz-Mazo, C. Danilevski, C. Darmanin, R. B. Doak, M. Domaracky, K. Dörner, Y. Du, H. Fangohr, H. Fleckenstein, M. Frank, P. Fromme, A. M. Gañán-Calvo, Y. Gevorkov, K. Giewekemeyer, H. M. Ginn, H. Graafsma, R. Graceffa, D. Greiffenberg, L. Gumprecht, P. Göttlicher, J. Hajdu, S. Hauf, M. Heymann, S. Holmes, D. A. Horke, M. S. Hunter, S. Imlau, A. Kaukher, Y. Kim, A. Klyuev, J. Knoška, B. Kobe, M. Kuhn, C. Kupitz, J. Küpper, J. M. Lahey-Rudolph, T. Laurus, K. Le Cong, R. Letrun, P. L. Xavier, L. Maia, F. R. Maia, V. Mariani, M. Messerschmidt, M. Metz, D. Mezza, T. Michelat, G. Mills, D. C. Monteiro, A. Morgan, K. Mühlig, A. Munke, A. Münnich, J. Nette, K. A. Nugent, T. Nuguid, A. M. Orville, S. Pandey, G. Pena, P. Villanueva-Perez, J. Poehlsen, G. Previtali, L. Redecke, W. M. Riekehr, H. Rohde, A. Round, T. Safenreiter, I. Sarrou, T. Sato, M. Schmidt, B. Schmitt, R. Schönherr, J. Schulz, J. A. Sellberg, M. M. Seibert, C. Seuring, M. L. Shelby, R. L. Shoeman, M. Sikorski, A. Silenzi, C. A. Stan, X. Shi, S. Stern, J. Sztuk-Dambietz, J. Szuba, A. Tolstikova, M. Trebbin, U. Trunk, P. Vagovic, T. Ve, B. Weinhausen, T. A. White, K. Wrona, C. Xu, O. Yefanov, N. Zatsepin, J. Zhang, M. Perbandt, A. P. Mancuso, C. Betzel, H. Chapman, and A. Barty, "Megahertz serial crystallography," *Nature Communications*, vol. 9, pp. 1–11, 10 2018.

[63] F. Stellato, D. Oberthür, M. Liang, R. Bean, C. Gati, O. Yefanov, A. Barty, A. Burkhardt, P. Fischer, L. Galli, R. A. Kirian, J. Meyer, S. Panneerselvam, C. H. Yoon, F. Chervinskii, E. Speller, T. A. White, C. Betzel, A. Meents, and H. N. Chapman, "Room-temperature macromolecular serial crystallography using synchrotron radiation," *IUCrJ*, vol. 1, pp. 204–212, 6 2014.

[64] D. P. DePonte, U. Weierstall, K. Schmidt, J. Warner, D. Starodub, J. C. Spence, and R. B. Doak, "Gas dynamic virtual nozzle for generation of microscopic droplet streams," *Journal of Physics D: Applied Physics*, vol. 41, p. 195505, 9 2008.

[65] U. Weierstall, D. James, C. Wang, T. A. White, D. Wang, W. Liu, J. C. Spence, R. Bruce Doak, G. Nelson, P. Fromme, R. Fromme, I. Grotjohann, C. Kupitz, N. A. Zatsepin, H. Liu, S. Basu, D. Wacker, G. Won Han, V. Katritch, S. Boutet, M. Messerschmidt, G. J. Williams, J. E. Koglin, M. Marvin Seibert, M. Klinker, C. Gati, R. L. Shoeman, A. Barty, H. N. Chapman, R. A. Kirian, K. R. Beyerlein, R. C. Stevens, D. Li, S. T. Shah, N. Howe, M. Caffrey, and V. Cherezov, "Lipidic cubic phase injector facilitates membrane protein serial femtosecond crystallography," *Nature Communications*, vol. 5, 2014.

[66] S. Botha, K. Nass, T. R. Barends, W. Kabsch, B. Latz, F. Dworkowski, L. Foucar, E. Panepucci, M. Wang, R. L. Shoeman, I. Schlichting, and R. B. Doak, "Room-temperature serial crystallography at synchrotron X-ray sources using slowly flowing free-standing high-viscosity microstreams," *Acta Cryst. D*, vol. 71, pp. 387–397, 2015.

[67] K. H. Nam, "Sample delivery media for serial crystallography," *International Journal of Molecular Sciences*, vol. 20, no. 5, 2019.

[68] S. Ghosh, D. Zoric, P. Dahl, M. Bjelčić, J. Johannesson, E. Sandelin, P. Borjesson, A. Björling, A. Banacore, P. Edlund, O. Aurelius, M. Milas, J. Nan, A. Shilova, A. Gonzalez, U. Mueller, G. Brändén, and R. Neutze, "A simple goniometer-compatible flow cell for serial synchrotron X-ray crystallography," *J. Appl. Cryst.*, vol. 56, pp. 449–460, 2023.

[69] C. G. Roessler, A. Kuczewski, R. Stearns, R. Ellson, J. Olechno, A. M. Orville, M. Allaire, A. S. Soares, and A. Héroux, "Acoustic methods for high-throughput protein crystal mounting at next-generation macromolecular crystallographic beamlines," *J. Synchrotron Rad.*, vol. 20, pp. 805–808, 9 2013.

[70] D. C. F. Monteiro, D. von Stetten, C. Stohrer, M. Sans, A. R. Pearson, G. Santoni, P. van der Linden, and M. Trebbin, "3D-MiXD: 3D-printed X-ray-compatible microfluidic devices for rapid, low-consumption serial synchrotron crystallography data collection in flow," *IUCrJ*, vol. 7, pp. 207–219, 3 2020.

[71] G. Illava, R. Jayne, A. D. Finke, D. Closs, W. Zeng, S. K. Milano, Q. Huang, I. Kriksunov, P. Sidorenko, F. W. Wise, W. R. Zipfel, B. A. Apker, and R. E. Thorne, "Integrated sample-handling and mounting system for fixed-Target serial synchrotron crystallography," *Acta Cryst. D*, vol. 77, pp. 628–644, 2021.

[72] A. Karpik, I. Martiel, P. M. Kristiansen, and C. Padeste, "Fabrication of ultrathin suspended polymer membranes as supports for serial protein crystallography," *Micro and Nano Engineering*, vol. 7, p. 100053, 6 2020.

[73] J. Lieske, M. Cerv, S. Kreida, D. Komadina, J. Fischer, M. Barthelmess, P. Fischer, T. Pakendorf, O. Yefanov, V. Mariani, T. Seine, B. H. Ross, E. Crosas, O. Lorbeer, A. Burkhardt, T. J. Lane, S. Guenther, J. Bergtholdt, S. Schoen, S. Törnroth-Horsefield, H. N. Chapman, and A. Meents, "On-chip crystallization for serial crystallography experiments and on-chip ligand-binding studies," *IUCrJ*, vol. 6, pp. 714–728, 2019.

[74] C. G. Feiler, D. Wallacher, and M. S. Weiss, "An all-in-one sample holder for macromolecular x-ray crystallography with minimal background scattering," *Journal of Visualized Experiments*, p. e59722, 7 2019.

[75] N. Coquelle, A. S. Brewster, U. Kapp, A. Shilova, B. Weinhausen, M. Burghammer, and J.-P. P. Colletier, "Raster-scanning serial protein crystallography using micro- and nano-focused synchrotron beams," *Acta Cryst. D*, vol. 71, no. 5, pp. 1184–1196, 2015.

[76] P. Mehrabi, H. M. Müller-Werkmeister, J.-P. Leimkohl, H. Schikora, J. Ninkovic, S. Krivokuca, L. Andriček, S. W. Epp, D. Sherrell, R. L. Owen, A. R. Pearson, F. Tellkamp, E. C. Schulz, and R. J. D. Miller, "The HARE chip for efficient time-resolved serial synchrotron crystallography," *Journal of Synchrotron Radiation*, vol. 27, no. 2, pp. 1–11, 2020.

[77] S. Horrell, D. Axford, N. E. Devenish, A. Ebrahim, M. A. Hough, D. A. Sherrell, S. L. Storm, I. Tews, J. A. Worrall, and R. L. Owen, "Fixed target serial data collection at diamond light source," *Journal of Visualized Experiments*, vol. 2021, p. e62200, 2 2021.

[78] A. Tolstikova, M. Levantino, O. Yefanov, V. Hennicke, P. Fischer, J. Meyer, A. Mozzanica, S. Redford, E. Crosas, N. L. Opara, M. Barthelmess, J. Lieske, D. Oberthuer, E. Wator, I. Mohacsi, M. Wulff, B. Schmitt, H. N. Chapmana, and A. Meents, "1 kHz fixed-target serial crystallography using a multilayer monochromator and an integrating pixel detector," *IUCrJ*, vol. 6, pp. 927–937, 2019.

[79] F. Cipriani, M. Röwer, C. Landret, U. Zander, F. Felisaz, and J. A. Márquez, "CrystalDirect: A new method for automated crystal harvesting based on laser-induced photoablation of thin films," *Acta Cryst. D*, vol. 68, pp. 1393–1399, 10 2012.

[80] H. Okumura, N. Sakai, H. Murakami, N. Mizuno, Y. Nakamura, G. Ueno, T. Masunaga, T. Kawamura, S. Baba, K. Hasegawa, M. Yamamoto, and T. Kumasaka, "In situ crystal data-collection and ligand-screening system at SPring-8," *Acta Cryst. F*, vol. 78, pp. 241–251, 6 2022.

[81] P. Aller, J. Sanchez-Weatherby, J. Foadi, G. Winter, C. M. Lobley, D. Axford, A. W. Ashton, D. Bellini, J. Brandao-Neto, S. Culurgioni, A. Douangamath, R. Duman, G. Evans, S. Fisher, R. Flaig, D. R. Hall, P. Lukacik, M. Mazzorana, K. E. McAuley, V. Mykhaylyk, R. L. Owen, N. G. Paterson, P. Romano, J. Sandy, T. Sorensen, F. Von Delft, A. Wagner, A. Warren, M. Williams, D. I. Stuart, and M. A. Walsh, "Application of in situ diffraction in high-throughput structure determination platforms," in *Methods in Molecular Biology*, pp. 233–253, Humana Press Inc., 2015.

[82] K. R. Beyerlein, D. Dierksmeyer, V. Mariani, M. Kuhn, I. Sarrou, A. Ottaviano, S. Awel, J. Knoska, S. Fuglerud, O. Jönsson, S. Stern, M. O. Wiedorn, O. Yefanov, L. Adriano, R. Bean, A. Burkhardt, P. Fischer, M. Heymann, D. A. Horke, K. E. Jungnickel, E. Kovaleva, O. Lorbeer, M. Metz, J. Meyer, A. Morgan, K. Pande, S. Panneerselvam, C. Seuring, A. Tolstikova, J. Lieske, S. Aplin, M. Roessle, T. A. White, H. N. Chapman, A. Meents, and D. Oberthuer, "Mix-and-diffuse serial synchrotron crystallography," *IUCrJ*, vol. 4, pp. 769–777, 10 2017.

[83] K. A. Zielinski, A. Prester, H. Andaleeb, S. Bui, O. Yefanov, L. Catapano, A. Henkel, M. O. Wiedorn, O. Lorbeer, E. Crosas, J. Meyer, V. Mariani, M. Domaracky, T. A. White, H. Fleckenstein, I. Sarrou, N. Werner, C. Betzel, H. Rohde, M. Aepfelbacher, H. N. Chapman, M. Perbandt, R. A. Steiner, and D. Oberthuer, "Rapid and efficient room-temperature serial synchrotron crystallography using the CFEL TapeDrive," *IUCrJ*, vol. 9, no. 6, pp. 778–791, 2022.

[84] M. Lahey-Rudolph, L. Holthusen, and M. Rößle, "Blotting Tapedrive - an efficient sample delivery for SX with low background noise," in *2nd Time-Resolved Structural Biology workshop, Poster*, 2022.

[85] P. Nogly, D. James, D. Wang, T. A. White, N. Zatsepin, A. Shilova, G. Nelson, H. Liu, L. Johansson, M. Heymann, K. Jaeger, M. Metz, C. Wickstrand, W. Wu, P. Båth, P. Berntsen, D. Oberthuer, V. Panneels, V. Cherezov, H. Chapman, G. Schertler, R. Neutze, J. Spence, I. Moraes, M. Burghammer, J. Standfuss, and U. Weierstall, "Lipidic cubic phase serial millisecond crystallography using synchrotron radiation," *IUCrJ*, vol. 2, pp. 168–176, 2015.

[86] E. C. Schulz, B. A. Yorke, A. R. Pearson, and P. Mehrabi, "Best practices for time-resolved serial synchrotron crystallography," *Acta Cryst. D*, vol. 78, pp. 14–29, 2022.

[87] G. Brändén and R. Neutze, "Advances and challenges in time-resolved macromolecular crystallography," *Science*, vol. 373, p. eaba0954, 8 2021.

[88] T. A. White, "Processing serial crystallography data with crystFEL: A step-by-step guide," *Acta Cryt. D*, vol. 75, pp. 219–233, 2019.

[89] H. R. Powell, "A beginner's guide to X-ray data processing," *The Biochemist*, vol. 43, pp. 46–50, 6 2021.

[90] V. R. Dubach and A. Guskov, "The resolution in x-ray crystallography and single-particle cryogenic electron microscopy," *Crystals*, vol. 10, pp. 1–13, 7 2020.

[91] G. Taylor, "The phase problem," in *Acta Cryst. D*, vol. 59, pp. 1881–1890, International Union of Crystallography, 10 2003.

[92] A. Wlodawer, W. Minor, Z. Dauter, M. Jaskolski, and B. Physics, "Protein crystallography for non-crystallographers, or how to get the best (but not more) from published macromolecular structures," *FEBS J*, vol. 275, no. 1, pp. 1–21, 2015.

[93] G. N. Murshudov, P. Skubák, A. A. Lebedev, N. S. Pannu, R. A. Steiner, R. A. Nicholls, M. D. Winn, F. Long, and A. A. Vagin, "REFMAC5 for the refinement of macromolecular crystal structures," *Acta Cryst. D*, vol. 67, no. 4, pp. 355–367, 2011.

[94] T. A. White, R. A. Kirian, A. V. Martin, A. Aquila, K. Nass, A. Barty, and H. N. Chapman, "CrystFEL: A software suite for snapshot serial crystallography," *J. Appl. Cryst.*, vol. 45, no. 2, pp. 335–341, 2012.

[95] A. Barty, R. A. Kirian, F. R. Maia, M. Hantke, C. H. Yoon, T. A. White, and H. Chapman, "Cheetah: Software for high-throughput reduction and analysis of serial femtosecond X-ray diffraction data," *Journal of Applied Crystallography*, vol. 47, no. 3, pp. 1118–1131, 2014.

[96] H. R. Powell, "The Rossmann Fourier autoindexing algorithm in MOSFLM," *Acta Cryst. D*, vol. 55, pp. 1690–1695, 10 1999.

[97] W. Kabsch, "XDS," *Acta Cryst. D*, vol. 66, no. 2, pp. 125–132, 2010.

[98] Y. Gevorkov, O. Yefanov, A. Barty, T. A. White, V. Mariani, W. Brehm, A. Tolstikova, R. R. Grigat, and H. N. Chapman, "XGANDALF - Extended gradient descent algorithm for lattice finding," *Acta Cryst. A*, vol. 75, pp. 694–704, 8 2019.

[99] A. J. McCoy, R. W. Grosse-Kunstleve, P. D. Adams, M. D. Winn, L. C. Storoni, and R. J. Read, "Phaser crystallographic software," *J. Appl. Cryst.*, vol. 40, no. 4, pp. 658–674, 2007.

[100] J. Agirre, M. Atanasova, H. Bagdonas, C. B. Ballard, A. Baslé, J. Beilsten-Edmands, R. J. Borges, D. G. Brown, J. J. Burgos-Mármol, J. M. Berrisford, P. S. Bond, I. Caballero, L. Catapano, G. Chojnowski, A. G. Cook, K. D. Cowtan, T. I. Croll, J. Debreczeni, N. E. Devenish, E. J. Dodson, T. R. Drevon, P. Emsley, G. Evans, P. R. Evans, M. Fando, J. Foadi, L. Fuentes-Montero, E. F. Garman, M. Gerstel, R. J. Gildea, K. Hatti, M. L. Hekkelman, P. Heuser, S. W. Hoh, M. A. Hough, H. T. Jenkins, E. Jiménez, R. P. Joosten, R. M. Keegan, N. Keep, E. B. Krissinel, P. Kolenko,

O. Kovalevskiy, V. S. Lamzin, D. M. Lawson, A. A. Lebedev, A. G. Leslie, B. Lohkamp, F. Long, M. Malý, A. J. McCoy, S. J. McNicholas, A. Medina, C. Millán, J. W. Murray, G. N. Murshudov, R. A. Nicholls, M. E. Noble, R. Oeffner, N. S. Pannu, J. M. Parkhurst, N. Pearce, J. Pereira, A. Perrakis, H. R. Powell, R. J. Read, D. J. Rigden, W. Rochira, M. Sammito, F. Sánchez Rodríguez, G. M. Sheldrick, K. L. Shelley, F. Simkovic, A. J. Simpkin, P. Skubak, E. Sobolev, R. A. Steiner, K. Stevenson, I. Tews, J. M. Thomas, A. Thorn, J. T. Valls, V. Uski, I. Usón, A. Vagin, S. Velankar, M. Vollmar, H. Walden, D. Waterman, K. S. Wilson, M. D. Winn, G. Winter, M. Wojdyr, and K. Yamashita, "The CCP4 suite: integrative software for macromolecular crystallography," *Acta Cryst. D*, vol. 79, pp. 449–461, 2023.

[101] E. Krissinel, A. A. Lebedev, V. Uski, C. B. Ballard, R. M. Keegan, O. Kovalevskiy, R. A. Nicholls, N. S. Pannu, P. Skubák, J. Berrisford, M. Fando, B. Lohkamp, M. Wojdyr, A. J. Simpkin, J. M. H. Thomas, C. Oliver, C. Vonrhein, G. Chojnowski, A. Basle, A. Purkiss, M. N. Isupov, S. Mcnicholas, E. Lowe, J. Triviño, K. Cowtan, J. Agirre, D. J. Rigden, I. Uson, V. Lamzin, I. Tews, G. Bricogne, A. G. W. Leslie, D. G. Brown, J. Trivinõ, K. Cowtan, J. Agirre, D. J. Rigden, I. Uson, V. Lamzin, I. Tews, G. Bricogne, A. G. W. Leslie, D. G. Brown, and S. Antonyuk, "CCP4 Cloud for structure determination and project management in macromolecular crystallography," *Acta Cryst. D*, vol. 78, no. Pt 9, pp. 1079–1089, 2022.

[102] G. N. Murshudov, A. A. Vagin, and E. J. Dodson, "Refinement of macromolecular structures by the maximum-likelihood method," *Acta Cryst. D*, vol. 53, no. 3, pp. 240–255, 1997.

[103] E. Krissinel and K. Henrick, "Secondary-structure matching (SSM), a new tool for fast protein structure alignment in three dimensions," *Acta Cryst. D*, vol. 60, no. 12 I, pp. 2256–2268, 2004.

[104] Schrödinger, "The PyMOL Molecular Graphics."

[105] F. Cipriani, F. Felisaz, L. Launer, J. S. Aksoy, H. Caserotto, S. Cusack, M. Dallery, F. Di-Chiaro, M. Guijarro, J. Huet, S. Larsen, M. Lentini, J. McCarthy, S. McSweeney, R. Ravelli, M. Renier, C. Taffut, A. Thompson, G. A. Leonard, and M. A. Walsh, "Automation of sample mounting for macromolecular crystallography," *Acta Cryst. D*, vol. 62, no. 10, pp. 1251–1259, 2006.

[106] J. Vojtěchovský, K. Chu, J. Berendzen, R. M. Sweet, and I. Schlichting, "Crystal structures of myoglobin-ligand complexes at near-atomic resolution," *Biophysical Journal*, vol. 77, no. 4, pp. 2153–2174, 1999.

[107] K. Klementiev, K. Norén, S. Carlson, K. G. Sigfridsson Clauss, and I. Persson, "The BALDER Beamline at the MAX IV Laboratory," in *Journal of Physics: Conference Series*, vol. 712, p. 012023, IOP Publishing, 5 2016.

[108] J. Baldwin and C. Chothia, "Haemoglobin: The structural changes related to ligand binding and its allosteric mechanism," *J. Mol. Biol.*, vol. 129, pp. 175–220, 4 1979.

[109] R. Liddington, Z. Derewenda, E. Dodson, R. Hubbard, and G. Dodson, "High resolution crystal structures and comparisons of T-state deoxyhaemoglobin and two liganded T-State haemoglobins: T(α-oxy)haemoglobin and T(met)haemoglobin," *Journal of Molecular Biology*, vol. 228, pp. 551–579, 11 1992.

[110] J. Wilson, K. Phillips, and B. Luisi, "The crystal structure of horse deoxyhaemoglobin trapped in the high-affinity (R) state," *Journal of Molecular Biology*, vol. 264, no. 4, pp. 743–756, 1996.

[111] P. Roedig, I. Vartiainen, R. Duman, S. Panneerselvam, N. Stübe, O. Lorbeer, M. Warmer, G. Sutton, D. I. Stuart, E. Weckert, C. David, A. Wagner, A. Meents, and . A. Meents, "A micro-patterned silicon chip as sample holder for macromolecular crystallography experiments with minimal background scattering," *Scientific Reports*, vol. 5, no. April, pp. 1–11, 2015.

[112] P. Roedig, R. Duman, J. Sanchez-Weatherby, I. Vartiainen, A. Burkhardt, M. Warmer, C. David, A. Wagner, and A. Meents, "Room-temperature macromolecular crystallography using a micro-patterned silicon chip with minimal background scattering," *Journal of Applied Crystallography*, vol. 49, pp. 968–975, 2016.

[113] P. Roedig, H. M. Ginn, T. Pakendorf, G. Sutton, K. Harlos, T. S. Walter, J. Meyer, P. Fischer, R. Duman, I. Vartiainen, B. Reime, M. Warmer, A. S. Brewster, I. D. Young, T. Michels-Clark, N. K. Sauter, A. Kotecha, J. Kelly, D. J. Rowlands, M. Sikorsky, S. Nelson, D. S. Damiani, R. Alonso-Mori, J. Ren, E. E. Fry, C. David, D. I. Stuart, A. Wagner, and A. Meents, "High-speed fixed-target serial virus crystallography," *Nature Methods*, vol. 14, no. 8, pp. 805–810, 2017.

[114] P. Fischer, A. Meents, T. Ursby, J. Meyer, A. Finke, I. Gorgisyan, J. Lidon-Simon, M. Eguiraun, M. Bjelcic, A. Gonzalez, E. Jagudin, J. Nan, M. Milas, O. Aurelius, A. Siwen, T. Kamnert, and G. Branden, "Roadrunner at BioMAX, unpublished work," 2023.

[115] Q. Chen and D. Wei, "Human cytochrome P450 and personalized medicine," in *Advances in Experimental Medicine and Biology*, vol. 827, pp. 341–351, Springer New York LLC, 2015.

[116] R. Andersson, C. Safari, R. Dods, E. Nango, R. Tanaka, A. Yamashita, T. Nakane, K. Tono, Y. Joti, P. Båth, E. Dunevall, R. Bosman, O. Nureki, S. Iwata, R. Neutze, and G. Brändén, "Serial femtosecond crystallography structure of cytochrome c oxidase at room temperature," *Scientific Reports*, vol. 7, no. 1, pp. 1–9, 2017.

[117] M. Caffrey and C. Porter, "Crystallizing membrane proteins for structure determination using lipidic mesophases," *Journal of Visualized Experiments*, no. 45, p. 1712, 2010.

[118] U. Mueller, M. Thunnissen, J. Nan, M. Eguiraun, F. Bolmsten, A. Milàn-Otero, M. Guijarro, M. Oscarsson, D. de Sanctis, and G. Leonard, "MXCuBE3: A New Era of MX-Beamline Control Begins," *Synchrotron Radiation News*, vol. 30, pp. 22–27, 1 2017.

[119] K. S. Clauss, A. Terry, R. Friel, S. Nehzati, L. Barbe, M. Bjelčić, A. Fornell, Y. Chen, and P. Micheal, "AdaptoCell," 2021.

[120] E. C. Schulz, P. Mehrabi, H. M. Müller-Werkmeister, F. Tellkamp, A. Jha, W. Stuart, E. Persch, R. De Gasparo, F. Diederich, E. F. Pai, and R. J. Miller, "The hit-and-return system enables efficient time-resolved serial synchrotron crystallography," *Nature Methods*, vol. 15, no. 11, pp. 901–904, 2018.

[121] T. C. Taylor and I. Andersson, "The structure of the complex between rubisco and its natural substrate ribulose 1,5-bisphosphate," *Journal of Molecular Biology*, vol. 265, no. 4, pp. 432–444, 1997.

[122] R. A. Nicholls, M. Tykac, O. Kovalevskiy, and G. N. Murshudov, "Current approaches for the fitting and refinement of atomic models into cryo-em maps using CCP-EM," *Acta Cryst. D*, vol. 74, no. 6, pp. 492–505, 2018.

[123] G. Schneider, Y. Lindqvist, and T. Lundqvist, "Crystallographic refinement and structure of ribulose-1,5-bisphosphate carboxylase from Rhodospirillum rubrum at 1.7 Å resolution," *Journal of Molecular Biology*, vol. 211, no. 4, pp. 989–1008, 1990.

[124] C. Wickstrand, R. Dods, A. Royant, and R. Neutze, "Bacteriorhodopsin: Would the real structural intermediates please stand up?," *Biochem Biophys Acta*, vol. 1850, pp. 536–553, 3 2015.

[125] K. Lommel, G. Schäfer, K. Grenader, C. Ruland, A. Terfort, W. Mäntele, and G. Wille, "Caged CO2 for the Direct Observation of CO2-Consuming Reactions," *ChemBioChem*, vol. 14, no. 3, pp. 372–380, 2013.

[126] C. R. Sales, G. E. Degen, A. B. da Silva, and E. Carmo-Silva, "Spectrophotometric determination of RuBisCO activity and activation state in leaf extracts," in *Methods in Molecular Biology*, vol. 1770, pp. 239–250, Humana Press Inc., 2018.

[127] Anwaruzzaman and A. Yokota, "Activation of ribulose 1,5-bisphosphate carboxylase/oxygenase by inorganic phosphate under nocturnal conditions," *Plant and Cell Physiology*, vol. 40, no. 7, pp. 695–701, 1999.

[128] T. Weinert, P. Skopintsev, D. James, F. Dworkowski, E. Panepucci, D. Kekilli, A. Furrer, S. Brünle, S. Mous, D. Ozerov, P. Nogly, M. Wang, and J. Standfuss, "Proton uptake mechanism in bacteriorhodopsin captured by serial synchrotron crystallography," *Science*, vol. 364, no. 6448, pp. 61–65, 2019.

[129] T. C. Taylor and I. Andersson, "Structure of a product complex of spinach ribulose-1,5-bisphosphate carboxylase/oxygenase," *Biochemistry*, vol. 36, no. 13, pp. 4041–4046, 1997.

[130] S. Ghosh, P. Borjesson, P. Dahl, R. Neutze, and M. Bjelčić, "Anti-settler."